Research on Coupling Mechanism of Primary Acoustic Instability in Downward-Propagating Flames

(下方伝播火炎における燃焼と音響学的不安定性の相互作用に関する研究)

SungHwan YOON

Research on Coupling Mechanism of Primary Acoustic Instability in Downward-Propagating Flames

By

SungHwan YOON

Submitted to the Department of Mechanical and Space Engineering, Hokkaido University, Japan, in Partial Fulfillment of the Requirement for the Degree of Doctor of Philosophy in Mechanical and Space Engineering

September 2016

Abstract

The understanding of thermo acoustic instabilities caused by an effective interaction between the heat release by combustion and acoustic fluctuations are of fundamental importance because industrial applications such as gas turbines and rocket engines often suffer when strong pressure disturbances develop. It is therefore significant to suppress the instabilities by acoustically decoupled flame as much as possible for engine designs considering the safety of accidental explosions.

Recent experimental studies of such thermo acoustic instability have frequently been conducted in downward-propagating flames in a tube open at one end, and described the different types of the development of acoustic instability which are a primary acoustic instability evolving from a smooth curved shape to a flat flame and a violent secondary acoustic instability evolving from the flat flame to a corrugated structure. The secondary acoustic instability is caused by pre-existing finite-amplitude of the primary acoustic oscillations. Therefore, the primary acoustic instability is key feature of the whole process. However, an important unsolved problem is the generation mechanism of the primary acoustic instability because this instability is a major cause of flame instability initiation.

This paper is concerned with the coupling mechanism of primary acoustic instability of downward-propagating flames in a combustion tube. As tested gases, ethylene/methane/ propane premixed flames diluted with carbon dioxide or nitrogen were selected. The flame front propagates from the open to the closed end of the tube, and, for a particular position, starts vibration under the presence of acoustic sound resonating at quarter wavelength. This phenomenon is called as the primary acoustic instability and focused on the growth mechanism responsible for acoustic sound amplification.

In Chapter 1, premixed flame overview and intrinsic flame instabilities are elucidated.

Then, the potential coupling mechanisms of acoustic instability suggested by previous researchers are introduced. Finally, an objective and a scope of this study are presented.

In Chapter 2, the experimental setup and procedure are described. The propagation tube (transparent acrylic tube, 50-mm inner diameter and 511-mm length for Chapter 3 and 4; 50-mm inner diameter and 711-mm length for Chapter 5) is fixed vertically and charged with the tested gas at atmospheric pressure. The time-dependent behaviors of the downward-propagating flame are recorded by two high-speed cameras. The temporal variation of the primary acoustic pressure is measured at the bottom end of the tube.

In Chapter 3, the main focus is to establish the dominant onset mechanism of primary acoustic instability between pressure coupling and acceleration coupling. To change the coupling constant, various gas compositions for lean ethylene flames diluted with carbon dioxide or nitrogen are used. Also, the CO_2 laser irradiation method is utilized to alter the shape of the flame front. Finally, the effects of acoustic losses on acoustic instability are also estimated.

In Chapter 4, the effects of the Lewis number on primary acoustic instability in non-equidiffusive flames, based on pressure coupling which is more dominant mechanism confirmed in Chapter 3, are described. In general, the chemical reaction rate becomes more sensitive to variations in gas temperature with decreasing Lewis number. This effect is significant on the enhancement of heat release in phase with acoustic pressure, because gas temperature fluctuation is generated from acoustic pressure fluctuation under constant enthalpy.

In Chapter 5, the effects of the various fuels for CH_4, C_2H_4 and C_3H_8 diluted with N_2 or CO_2 on acoustic instability are additionally introduced. Different fuels cause to change gas properties and *Le*. Therefore, the dependence of effects of fuel on generation mechanisms of primary as well as secondary acoustic instabilities followed by previous Chapter 3 and 4 is estimated.

In Chapter 6, conclusions are briefly summarized based on experimental evidences.

In Appendix A, calculation of acoustic losses with various gas properties is presented. How to calculate acoustic intensity as the flame movements and measured acoustic pressure is described in Appendix B. In Appendix C and D, achievements which are awarded from photo contest of beautiful flame in combustion society of Japan and award of visualization of combustion in Korea society of combustion are introduced.

Keywords: Acoustic instability, Acoustic intensity, Activation energy, Coupling mechanism, Growth rate, Laser irradiation, Lewis number, Primary acoustic instability, Rayleigh criterion, Secondary acoustic instability.

Thesis Supervisor: Osamu Fujita

Title: Professor

Acknowledgements

First of all, I would like to express my sincere gratitude to my supervisor, Professor Osamu Fujita, for giving a chance to study under his supervision and unstinting support, invaluable instructions, great encouragement and good guidance as well as offering the excellent research environment during my PhD course. He has taught me, not only how to complete research work based on experimental idea, but also patience for scientific achievement. Furthermore, I could learn how could interact to people who think differently to me and the process how persuade others about my opinion from him.

I would like to thank Prof. Harunori Nagata, Prof. Nobuyuki Oshima, Prof. Nozomu Hashimoto and Prof. Osamu Fujita on evaluation committee and also for their help on my study and research in the past years. I appreciate Prof. Takashi Nakamura, Prof. Kazuaki Sasaki, Prof. Masao Watanabe, Prof. Hiroshi Terashima, Prof. Itsuro Kajiwara, Prof. Takemi Chikahisa, Prof. Hideyuki Ogawa and Prof. Koichi Sasaki on judgment committee.

I wish to thank Professor Nozomu Hashimoto and Professor Yuji Nakamura for their generous help and encouragement on my research. I very much appreciate Prof. Hashimoto for his kind comment on my research and valuable advice as the elder in life. I thank Ms. Miho Taga for her kind help dealing a lot of paper works related to my research and business trips.

I especially want to acknowledge my master-course supervisor, Professor Jeong Park (Pukyung National University, Korea), for his continuous encouragement and extremely valuable instruction. He is the first teacher who led me into the combustion society and scientific research. I very much appreciate him for the efforts to introduce me to the PhD course at Hokkaido University under Prof. Fujita's supervision.

I would like to thank Professor OhBoong Kwon (Pukyung National University, Korea), who is my undergraduate-course supervisor, for his kind instruction and continuous encouragement which have enabled me to be a researcher.

I wish to thank Professor Longhua Hu (USTC) for co-work and publishing a journal paper together. It was very great experience for me and I am looking forward to study with him in the future.

I am very much grateful to my research group member (OFG), Kira Aguilar, TaeJoon Noh, YongHo Chung, Yuiko Sato, Johan Sick and Yoichiro Koyama, for lots of help and academic discussion. I hope that we shall have an opportunity to study combustion research together in the future. Especially, I very much appreciate TaeJoon Noh for not only co-work but also personal discussion.

I have met many good friends at HU. I would like to thank them, Dr. Jian Gao, Dr. Akter Hossain, Prof. Longhua Hu, TaeJoon Noh, YongHo Chung, Kenichi Sato, Masashi Nagachi and Yusuke Konno. I am grateful to them for their friendship and the parties enjoyed with them in the past years gave me warmness and happiness.

I would like to express my gratitude to the Ministry of Education of Japanese Government (MEXT) for providing me with financial support for 3 years as a Monbukagakusho scholarship. I also would like to express my especial thank again to my supervisor Professor Osamu Fujita for arranging the scholarship.

My warmest thanks are due to my friends, Dr. YangKyun Kim and Yan Hui for their sincere friendship and help on various ways regarding life in Japan.

My sincere thanks go to my family for their endless support, inspiration and love which encourage me to keep going on study in Japan. *Thanks to my father and mother.*

Thanks to my wife JeeHyun Noh and to my son JaeMin Youn

Table of Contents

List of figures

List of tables

Nomenclature

a	amplitude of curved flame
a_f	maximum amplitude of curved flame
A_f	flame surface area
A_{final}	final amplitude of perturbation
$A_{initial}$	initial amplitude of perturbation
A_p	Arrhenius rate prefactor
c	speed of sound
C_p	specific heat under constant pressure
C_v	specific heat under constant volume
d	tube diameter
D	mass diffusivity of deficient species
E	activation energy
$E_{ex.}$	gas expansion ratio
g	acceleration of gravity
I	sound intensity or acoustic intensity
$\langle I \rangle$	average sound intensity
k	wave number
K	flame stretch rate
l_{tip}	flame tip position
L	tube length
L_b	Markstein length
m	mass fraction of the limiting reactant
p'	acoustic pressure fluctuation

P	acoustic pressure
p^n	pre-exponential factor
P_o	acoustic pressure at bottom of tube
P_u	acoustic pressure in unburned mixture
q	heat flux
q'	heat flux fluctuation
r	tube radius
r^*_{cur}	radius of curvature at the flame tip
R	gas constant
S_b	unstretched burning velocity in downstream
S_d	displacement flame velocity
$S_{d,lim.}$	displacement velocity enhance by the buoyancy
S_L	laminar burning velocity
S_n	local flame velocity
$S_{n,T}$	tangentially local flame velocity
S_u	unstretched burning velocity in upstream
t	time
T_b	adiabatic flame temperature
T_u	temperature in unburned mixture
u_a	acoustic velocity
u_b	flow velocity in burned mixture
u_n	flow velocity of normal direction in unburned mixture
u_T	flow velocity of tangential direction in unburned mixture
u_u	flow velocity in unburned mixture
u^*	flow velocity at the flame tip

U	flame velocity
w_f	maximum width of curved flame
x	distance from bottom of tube

Greek Symbols

α	thermal diffusivity
γ	specific heat ratio
Γ	total growth rate
δ_f	flame thickness
δ_r	reaction zone
δ_p	preheat zone
ε	total energy per unit cross-sectional area
θ	angle
λ	wavelength of sound
ν	kinematic viscosity
ξ_u	displacement of unburned mixture
ρ	density
ρ_b	density in burned mixture
ρ_u	density in unburned mixture
σ_{cur}	growth rate of flame curvature effect
σ_{DL}	growth rate of D–L instability
$\sigma_{lin.}$	growth rate of linear instability
σ_{non}	growth rate of nonlinear instability
σ_{RT}	growth rate of R–T instability
τ_a	acoustic time

$1/\tau_{exp}$	experimental growth rate of acoustic instability
$1/\tau_{ins}$	calculated growth rate of acoustic instability
$1/\tau_{loss}$	total acoustic loss
$1/\tau_{obs}$	observed growth rate of acoustic instability
$1/\tau_{rad}$	radiative losses
t_{res}	residential time
τ_t	transit time
$1/\tau_{wall}$	wall losses
Φ	equivalence ratio
ω	angular frequency

Dimensionless Numbers

β	dimensionless activation energy or Zel'dovich number
Le	Lewis number ($=\alpha/D$)
Le_c	critical Lewis number ($=1-2/\beta$)
$Le_{re.}$	reduced Lewis number ($=\beta(Le-1)$)
M	Mach number ($=S_L/c$)
Ma	Markstein number ($=L_b/\delta_f$)
Pr	Prandtl number ($=\nu/\alpha$)
S	normalized flame surface area
Tr	transfer function defined by Ref. [11]
x	dimensionless space coordinates

Subscript

b	burned mixture

f	flame
u	unburned mixture
o	bottom of tube

Chapter 1: Introduction

1.1 Premixed flame overview

The general definition of premixed flame is that a wave of chemical reaction propagates to the unburned mixture in a nonequilibrium environment, once ignition is achieved in a flammable mixture. The wave phenomenon of premixed flame is different with nonpremixed flame located at the stoichiometric line between the fuel and oxidizer sources. The essential characteristic of the premixed combustion process is that the reactants are sufficiently hot. Two possible mechanisms of wave propagation exist, namely subsonic deflagration wave and supersonic detonation wave. For deflagration, the chemical reaction gives a heat source to the unburned mixture by thermal diffusion which is quasi-isobaric process. However, for detonation, a shock wave caused by the gas expansion supplies the heat to the fresh gases which is associated with a large pressure jump. The present paper is only focused on deflagration wave.

In Chapter 1.1.1, the structure of premixed flames with chemical reaction time and thicknesses of preheat and reaction zones shall be identified based on Arrhenius form. Then, in Chapter 1.1.2, the relationship between the flame thickness and the Zel'dovich number is described. Finally, the laminar flame velocity, which is a phenomenological description of the premixed flames, is discussed. It is a representative property of the combustible gas indicating exothermic reaction rate, and contains significant information which is flammable limit, flash back, and turbulent behavior.

1.1.1 Premixed flame structure

The steady propagating planar flame with adiabatic condition is considered. For a simple

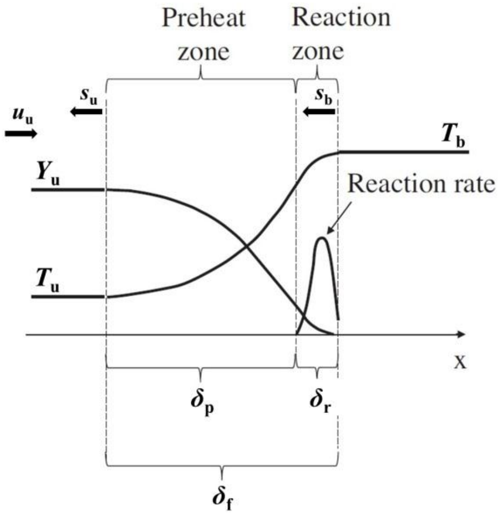

Fig. 1.1 Schematic of the premixed flame structure.

framework of premixed flame structure, one-step high-activation energy kinetics is assumed. Figure 1.1 shows the typical one dimensional premixed flame structure. The flame consists of two regions which are a nonreacting convective-diffusive (preheat) zone, δ_p, and a reactive-diffusive (reaction) zone, δ_r. In the preheat zone, the incoming reactants are preheated by thermal diffusion from the reaction zone and the reaction rate is negligible at $T < T_b$. Most chemical reaction occurs in the reaction zone with the heat generation and all the chemical energy released supplies heat source to the preheat zone by diffusion process in adiabatic condition, particularly. The reactant consumption rate is generally presented by the Arrhenius form:

$$\dot{\omega} \propto p^n exp^{-E/RT} \quad (1\text{-}1)$$

where p^n, E, and R are pre-exponential factor, activation energy, and gas constant, respectively. Considering methane flames, typical order of magnitude for E is generally 160 kJ/mole. To initiate combustion process, the large value of the activation is required than the thermal energy: $E/RT \gg 1$. The reaction takes place at δ_r which is $E/RT \approx 9.5$ ($T_b \approx 2000$ K), considering the reaction (or transit) time scale ($\tau_t \approx 10^{-4}$ s). On the other hand, in the preheat zone which is normally $E/RT \approx 65$ ($T_u \approx 300$ K), the reaction is very hard to occur because of too slow reaction time scale ($\tau_t \approx 10^{11}$ year). Therefore, the propagation mechanism of premixed flame is that the reaction zone is fed by the diffusive flow of flammable mixture.

1.1.2 Laminar burning velocity

In the Fig. 1.1, two different velocities are identified by different characterized regions of flame spread which are δ_r and δ_p. In the region of δ_r, a unstretched burning velocity in downstream, S_b, can be defined with respect to the burned side [1]:

$$S_b = L_b K + S_n \tag{1-2}$$

where L_b, K, and S_n are Markstein length in the burned side, a flame stretch rate, and a local flame velocity, respectively. The flame stretch rate is defined as [2]

$$K = \nabla_t \cdot S_{n,T} + (S_n \cdot n)(\nabla_T \cdot n) \tag{1-3}$$

where $S_{n,T}$ and n are a tangentially local flame velocity and a unit normal vector of the surface as shown in Fig. 1.2, respectively. Here, the first term is the stretch due to the nonuniform tangential velocity field, while the second term represents the flame displacement and the third term implies the effect of curvature. For the stationary (no propagation) and/or the planar flames, the second and third terms vanish. Also, when the flame has single cell similar to hydrodynamic instability (long wavelength disturbance), Eq. (1-3) can be alternatively expressed as [3]

$$K = -\frac{\partial S_{n,T}}{\partial T} + \frac{(|u^*| + S_n)}{r^*_{cur}} \tag{1-4}$$

at the central flame tip. Here, u^* and r^*_{cur} are a flow velocity and a flame radius of curvature at the flame tip as shown in Fig. 1.2, respectively. From Eq. (1-2), it is recognize that the local flame velocity and the flame stretch have a linear relationship by previous study [1]. Then, a unstretched burning velocity in upstream, S_u, can be described, considering the gas expansion in behind of the flame front as

$$S_u = S_b \left(\frac{\rho_b}{\rho_u}\right) \tag{1-5}$$

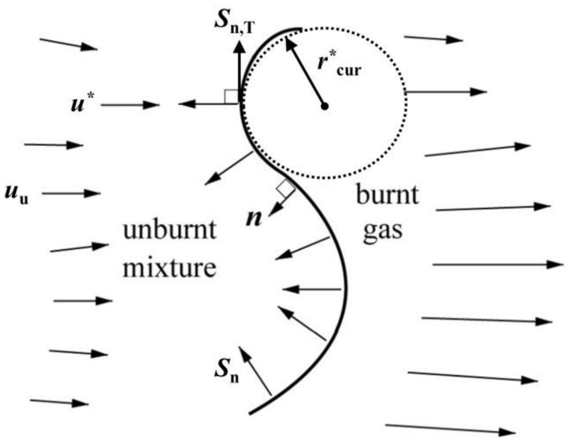

Fig. 1.2 Schematic diagram of the flame surface and its coordinate system.

, where ρ is the density of mixture. Generally, the unstretched burning velocity in upstream corresponds with the laminar burning velocity: $S_u = S_L$. As mentioned above, the flame spread is controlled by the thermal diffusion and the chemical reaction which is the same order of the chemical time. Thus, the laminar flame velocity can be expressed by

$$S_{\mathrm{L}} \approx \sqrt{\alpha/\tau_t} \tag{1-6}$$

where α is the thermal diffusivity of unburned mixture. Also, the flame thickness can be estimated as

$$\delta_{\mathrm{f}} = \alpha/S_{\mathrm{L}} \equiv \sqrt{\alpha\tau_t}. \tag{1-7}$$

Another important consideration is the relative thickness of the reaction and preheat zone described by

$$\frac{\delta_{\mathrm{r}}}{\delta_{\mathrm{p}}} \sim \frac{T_{\mathrm{b}}^2}{(T_{\mathrm{b}} - T_{\mathrm{u}})\frac{E}{R}} \equiv \frac{1}{\beta}. \tag{1-8}$$

Here, β is introduced as dimensionless activation energy, the Zel'dovich number, which can be calculated [4] as follows.

$$\beta = E(T_{\mathrm{b}} - T_{\mathrm{u}})/(RT_{\mathrm{b}}^2). \tag{1-9}$$

The Zel'dovich number is a nondimensional measure of the sensitivity of the reaction rate to temperature variations. From Eq. (1-8), if the high activation energy and sufficiently low temperature of unburned mixture are assumed, the reaction zone should be much thinner than the preheat zone, $\delta_r/\delta_p \ll 1$; the flame thickness is essentially the same as the preheat zone, $\delta_f \sim \delta_p$. Indeed, the inverse Zel'dovich number physically implies the flame thickness. In quasi-isobaric process, the order of magnitude in introduced each values can be estimated as follows:

$$\frac{S_b}{S_u} = \frac{\rho_u}{\rho_b} = \frac{T_b}{T_u} \equiv E_{ex.} \approx 7 \tag{1-10}$$

where $E_{ex.}$ represents gas expansion ratio.

In this chapter 1.1, significant parameters and properties of the premixed flame in the deflagration wave are discussed, and the combustion instability which is main topic of the present paper will be evaluated based on the estimation in here.

1.2 Intrinsic flame instabilities in premixed combustion

This Section mainly describes intrinsic flame instabilities in premixed system. Here, forced instabilities are not considered such as effects of flow field, acoustic sound by external input, and pressure wave by forced vibration. Nevertheless, the premixed flame essentially undergoes unstable processes. It can be classified as three categories are body force (Rayleigh–Taylor), hydrodynamic (Darrieus–Landau), and diffusive-thermal instabilities. The R–T instability is caused by gravitational force largely determined as propagation direction and combustor shape. This is external influences, not combustion properties. In contrast, the D–L and the diffusive-thermal instabilities are included in internal influences mainly caused by heat release based on the chemical reaction. Technically, the three different types of flame instabilities in premixed system closely interact with each other. Therefore, the mechanisms of the each instability are discussed based on theoretical analysis. Then, the most complete description of flame stability (e.g. dispersion relation) is introduced in detail.

1.2.1 Body force instability

In the acceleration field, the fluid surface is unstable when the gravity works from the heavy to the light densities. This phenomenon is called as "R–T instability". For combustion process, if a flame propagates upwards in the gravitational field, there is an appropriate condition for development of the R–T instability as shown in Fig. 1.3. Also, the flame's shape in upward propagating is more convex than downward, and the displacement velocity enhance by the buoyancy effect. The rise velocity of the flame, $S_{\mathrm{d,lim.}}$, is determined as [6]:

$$S_{\mathrm{d,lim.}} = 0.33\sqrt{gd}. \tag{1-11}$$

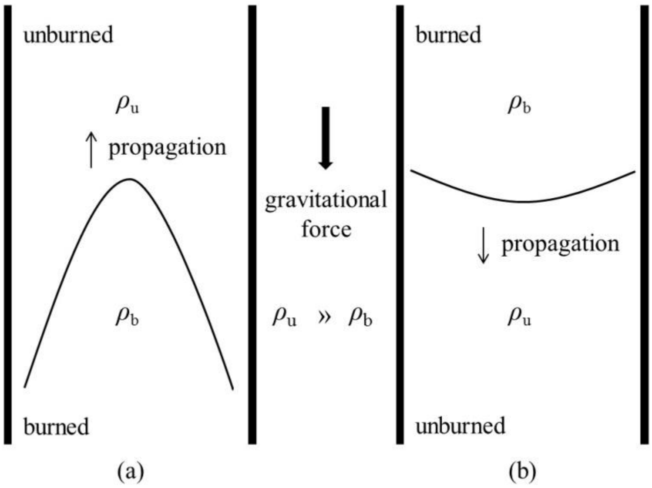

Fig. 1.3 Schematic of buoyancy-induced flame in tube; (a) upward propagation and (b) downward propagation.

Here, g and d represent acceleration of gravity and tube diameter, respectively. This value is only determined by hydrodynamics, and lower velocity than $S_{\mathrm{d,lim.}}$, indicates that the extinction mechanism is additionally considered with hydrodynamics, rather than the chemical reaction alone.

However, for downward propagating flames, there are not so serious effects of the R–T instability because the buoyancy flow is structurally stable as shown in Fig. 1.3, and the displacement velocity is almost the same with the laminar burning velocity, $S_{\mathrm{d}} \approx S_{\mathrm{L}}$, when $u_{\mathrm{u}} = 0$ (freely propagating flames). Also, the flame is relatively small amplitude of curved shape. Nevertheless, the buoyancy flow marginally affect to the flame front and the critical value of the rise velocity, $S_{\mathrm{d,lim.}}$, is calculated by [7]:

$$S_{\mathrm{d,lim.}} \approx (g\alpha)^{1/3}. \quad (1\text{-}12)$$

Let us consider the growth rate of the R–T instability in an infinitely thin flame. The expression of the growth rate is derived by

$$\sigma_{\mathrm{RT}} = \sqrt{\frac{E_{\mathrm{ex.}}-1}{E_{\mathrm{ex.}}+1} gk} \quad (1\text{-}13)$$

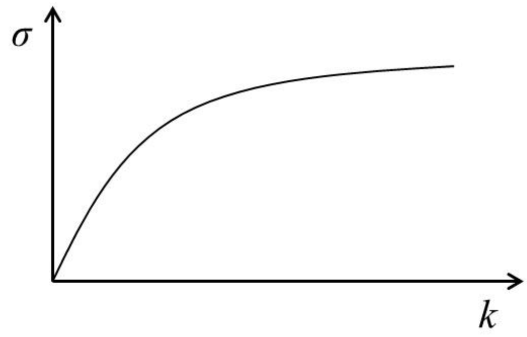

Fig. 1.4 Schematic diagram of the growth rate of the R-T instability in upward propagating flames.

where, k is a wave number. The dimensionless perturbation of the flame front, F(x, t) is derived as $F = \exp(\sigma t + ik\mathrm{x})$, where x is dimensionless space coordinates. For, upward propagating flames (positive gravitational force), the formula in the radical sign has positive value and the growth rate has real number, $\sigma_{\mathrm{RT}} \sim \sqrt{gk}$. Then, gk is always positive and the R–T instability will be growing up. For, downward propagating flames (negative gravitational force), however, the formula in the radical sign has negative value and the growth rate has complex number, $\sigma_{\mathrm{RT}} \sim i\sqrt{gk}$. This result leads to the stable flame from the R–T instability. To understand the growth rate of the R–T instability more clearly, Figure 1.4 shows the relation between σ_{RT} and k. The R–T instability suppresses at small wave number (large wavelengths) and the growth rate increases until an intermediate wave number. Finally, the growth rate has nearly a constant value after the intermediate wave number.

1.2.2 Hydrodynamic instability

In general, the premixed flame front is unstable to the hydrodynamic instability and will spontaneously take form curved shape. This phenomenon dealt with George Darrieus and Lev Landau at first [8, 9]. The thermal expansion plays a role of the discontinuity for the flow direction. Because the Mach number, $M \equiv S_{\mathrm{L}}/c$ (where c is speed of sound), of deflagration flames is very small; the flow can be assumed as quasi-incompressible.

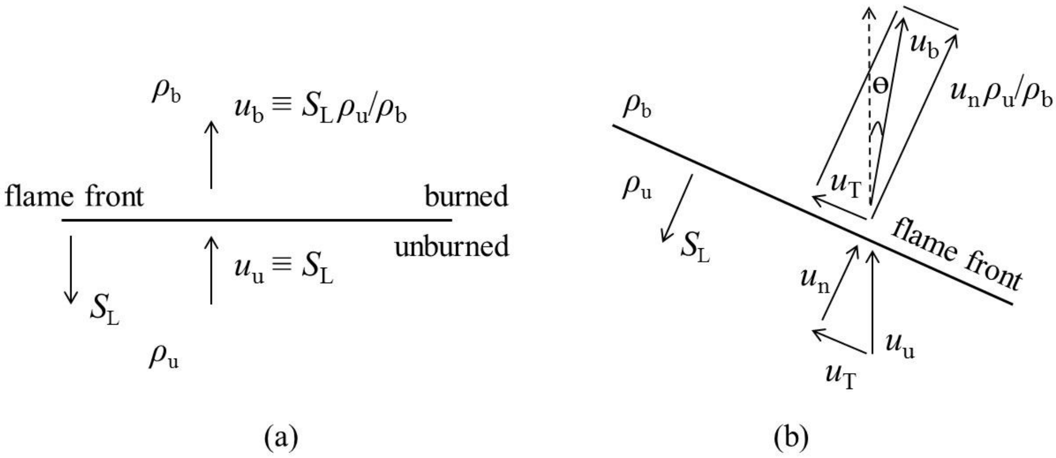

Fig. 1.5 Gas expansion through (a) planar flame and (b) Bunsen flame.

Considering the planar flame front as shown in Fig. 1.5(a), the large activation energy is firstly assumed with an infinitely thin flame thickness. Then the cold (unburned) mixtures with temperature, T_u, and density, ρ_u, come into the hot (burned) mixtures with temperature, T_b, and density, ρ_b. This propagate velocity, u_u, is the same with S_L considering no forced flow velocity (freely propagating flames) and $u_b = S_L(\rho_u/\rho_b)$ because of the gas expansion. From Eq. (1-10), the small pressure jump generates by the velocity jump at the discontinuity interface considering momentum conservation as below:

$$\delta p = \frac{1}{2}(\rho_b u_b^2 - \rho_u u_u^2) \equiv \frac{1}{2}(\rho_u S_L^2)(\frac{\rho_u}{\rho_b} - 1). \tag{1-14}$$

The pressure difference, δp, is generally of the order of 1 Pa.

Considering the inclined flame front as shown in Fig. 1.5(b), the vector of the incoming flow consists of two components which are a normal velocity to the front, u_n, and a tangential velocity to the front, u_T. If the stationary flame ($S_d = 0$) is assumed, the normal component is obviously the same with the laminar burning velocity, $u_n = S_L$. Then, the normal component of the flow velocity at downstream (burned side) is equal to $u_n(\rho_u/\rho_b)$ because of the gas expansion. However, the component of the tangential velocity, u_T, is not changed through

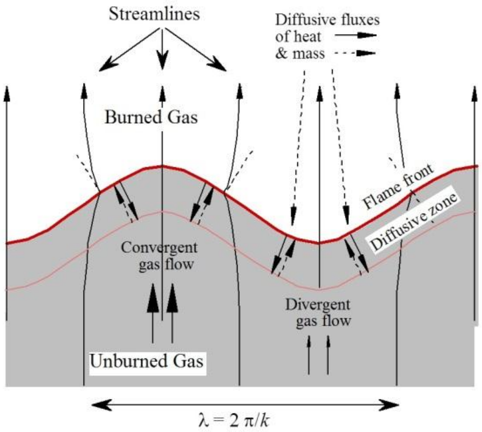

Fig. 1.6 Structure of a wrinkled flame front showing the hydrodynamic streamlines and the diffusive fluxes of heat and mass in Ref. [10].

discontinuity. Therefore, the incoming flow deviates toward the outgoing wave as θ in Fig. 1.5.

Summarizing the above theoretical explanations, it can be understood that the gas expansion is unavoidable process in combustion regardless of flame's shape. However, the deviation of streamlines occurs except of the planar flame. Thus, the deviation will be intensified when the flame has curvature caused by the body force and the diffusive-thermal instabilities.

Figure 1.6 shows the hydrodynamic streamlines and the diffusive fluxes of heat and mass in a wrinkled flame front. The diffusive-thermal effects will be discussed in Chapter 1.2.3. In Fig. 1.6, the incoming flows undergo divergence and convergence at convex and concave towards the fresh mixture by the thermal expansion, respectively. The growth rate of the D–L instability is presented through the function of wave number, laminar burning velocity, and gas expansion ratio as [9]:

$$\sigma_{\mathrm{DL}} = kS_L\left(\frac{E_{\mathrm{ex.}}}{E_{\mathrm{ex.}}+1}\sqrt{\frac{{E_{\mathrm{ex.}}}^2+E_{\mathrm{ex.}}-1}{E_{\mathrm{ex.}}}}-1\right). \tag{1-15}$$

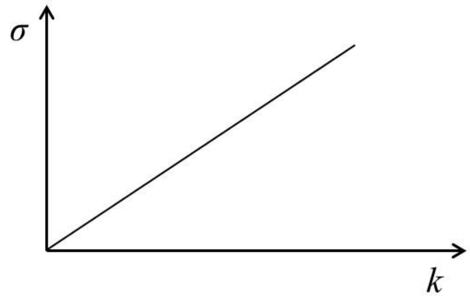

Fig. 1.7. Schematic diagram of the growth rate of the D–L instability.

This analysis is only valid for the wrinkled flame front with which the wavelength is much larger than flame thickness. To understand the growth rate of the D–L instability more clearly, the growth rate as the wave number is assigned in Fig. 1.7. The growth rate has linear relationship with *k*. Meanwhile, for which the wavelength is comparable with flame thickness, the flame front is affected by diffusive-thermal effects. This is room for doubt, which the restabilization of the D–L instability at large *k* generates or not. This issue will be discussed in more detail in the next chapter.

1.2.3 Diffusive-thermal instability

In the assumption of the premixed flame with high activation energy, the flame thickness is very thin and the heat and mass diffusion can control propagation process within the thin layer. Therefore, the gradient of temperature and mass concentration are parallel to the normal direction of propagation in the planar flame. However, for the wrinkled flame, they are no longer parallel.

Now, the structure of a wrinkled flame front is reconsidered as shown in Fig. 1.6. For the concave structure, the incoming gas temperature locally increases by effect of convergent heat flux (indicated as the solid arrows in Fig. 1.6), and local propagation velocity should be increase. The convex structure is the complete opposite. Thereby, the wrinkled flame should be stabilized only concerning thermal diffusion effects.

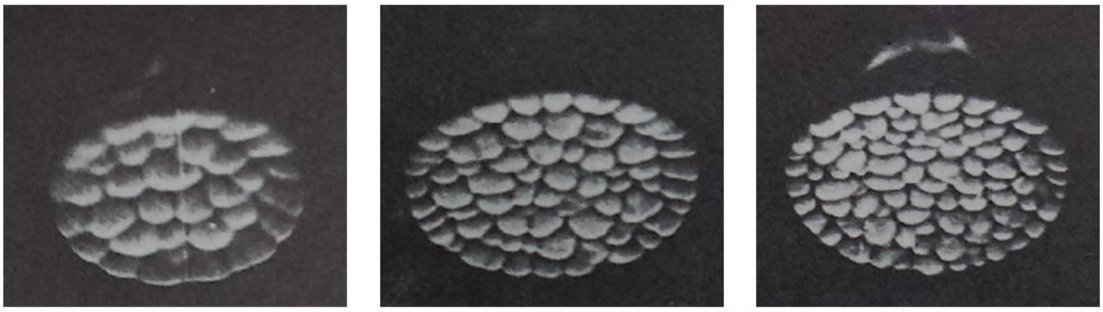

C_2H_4 C_3H_8 C_4H_{10}

Fig. 1.8. Images of cellular flames in fuel-rich hydrocarbon-air-nitrogen mixtures at d = 10 cm and atmospheric pressure in Ref. [12].

In consideration of mass concentration, the incoming mass flux is locally divergent at the concave structure (indicated as the dotted arrows in Fig. 1.6), and local propagation velocity should be decrease with reaction rate. Thereby, the wrinkled flame should be destabilized by mass diffusion effects, which is opposite to the thermal diffusion. This imbalance of the diffusion effects [5, 11] represents as Lewis number, $Le = \alpha/D$. Here, D is mass diffusivity of deficient species. When Lewis number is larger (less) than unity, the thermal (mass) diffusion is dominant parameter in the propagation mechanism and the flame will be thermo-diffusively stable (mass-diffusively unstable). In particular, at low Le ($Le < 1$), the diffusive-thermal instability often takes place itself in the form of cellular structure as shown in Fig. 1.8 and extensively suited by Markstein [12]. More recently, Joulin and Clavin [13] theoretically treated this phenomenon and reported that the region of existence of cellular instability broadens as the volumetric heat loss increases, therefore, the instabilities more easily occur when heat loss is significant. More detail discussion of this issue will be expressed, with pulsating instability at $Le > 1$, in this Section 1.2.5.

Barenblatt et al. [14] theoretically showed the growth rate in linear analysis of the stability of a plane flame front to long wave disturbances yields as follows:

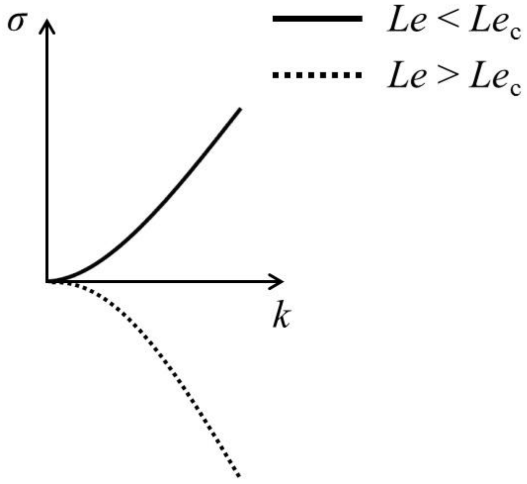

Fig. 1.9. Schematic diagram of the growth rate of the diffusive-thermal instability.

$$\sigma_{\mathrm{Le}} = \alpha[\frac{1}{2}\beta(1 - Le) - 1]k^2. \tag{1-16}$$

According to Eq. (1-16), the growth rate, σ_{Le}, is always positive at $Le < Le_c$ for any value of k as shown in Fig. 1.9. Here, the critical Le is defined as Le_c = 1-2/β. On the other hand, the flame is always stable at $Le > Le_c$ as shown in Fig. 1.9. Typical value is $\beta \approx 15$, and therefore, $Le_c \approx 0.87$. This value is good agreement with experimental study [12]. However, this theoretical study is limited only for long wavelength and required the relaxation effect for short wavelength disturbance. Otherwise, for $Le < Le_c$, the flames consistently undergo unstable perturbation in combination with D–L instability even though really do not.

Another the relaxation parameter on the flame stabilization is pure curvature effects (flame stretch rate). Again, let us reconsider figure 1.6. For the concave structure, the thermal diffusion is relatively strong by converging effect and local propagation velocity should be increases when wavelengths comparable with the flame thickness. The convex structure is opposite. This phenomenon is independent of Le effects, and the stabilizing force is enhanced by gas expansion because of increasing stretch rate. This thermo-diffusive stabilization is first treated by Markstein [15] who demonstrated that the flame is stable, if Markstein number, $Ma = L_b/\delta_f$, is positive. This expression is written as

$$\frac{S_n - S_L}{S_L} = Ma\frac{\delta_f}{r_{cur}}. \tag{1-17}$$

Now, let's discuss the physical meaning of Eq. (1-17). For the concave structure, the flame curvature is positive and the term of the r.h.s. of Eq. (1-17) is also positive at $Ma > 0$. Local flame velocity, S_n, is faster than laminar burning velocity, S_L, according to Eq. (1-17). Here, if a stationary flame ($S_n = S_L$) is assumed, displacement velocity, S_d, has positive value because of flow velocity smaller than S_d. After then, the flame will be stable (planar shape) as shown in Fig. 1.9. For $Ma < 0$, the term of the r.h.s. of Eq. (1-17) is negative. Local flame velocity, S_n, is slower than laminar burning velocity, S_L. Then, S_d has negative value because of flow velocity faster than S_d. After then, the flame will be more unstable (more concave shape) as shown in Fig. 1.9. The convex structure (negative curvature) is the complete opposite. Therefore, Markstein number is dominant parameter for short wavelength disturbance on the effect of curvature on localized burning velocity concerning flame stabilization.

The growth rate of flame curvature, which is relaxation parameter of flame stabilization, is described as follows [16]:

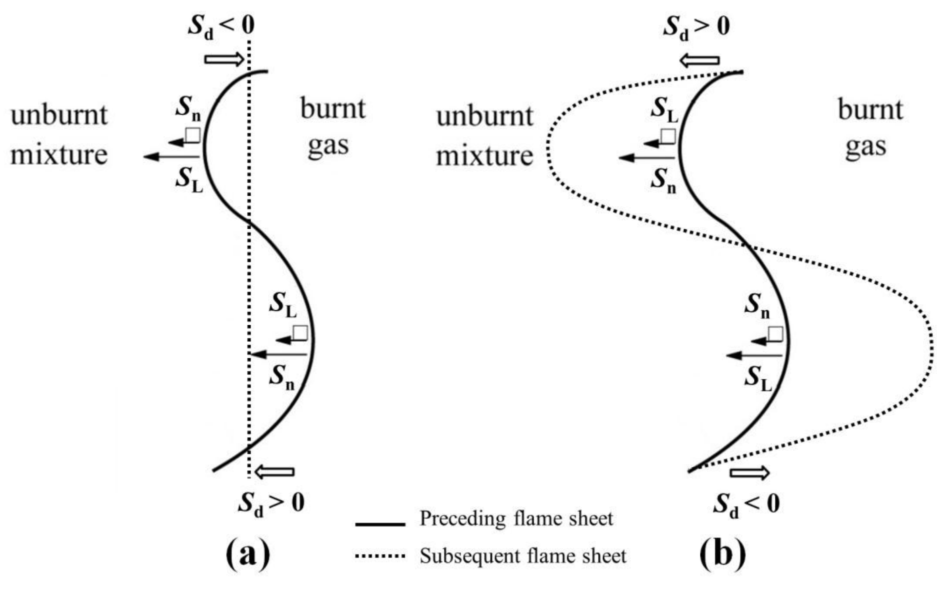

Fig. 1.10. Variation of wrinkled flame shape depending on *Ma*; (a) $Ma > 0$ (stable) and (b) $Ma < 0$ (unstable).

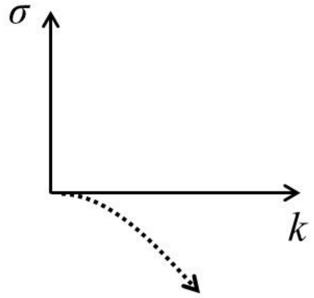

Fig. 1.11. Schematic diagram of the growth rate of curvature effect.

$$\sigma_{\mathrm{cur}} = -4\alpha\delta_{\mathrm{f}}^{2}k^{4}. \tag{1-18}$$

This equation, as was first pointed out by Sivashinsky [16], is different expression in effect of curvature with Eq. (1-17) suggested by Markstein [15], however, the both physical understanding are almost the same. In fact, Markstein theory is better description only for kinematic analysis even though it cannot arbitrarily be formulated as growth parameter, σ.

The growth rate of curvature effect is assigned as the wave number in Fig. 1.11. The growth rate, σ_{cur}, is always negative and supports the flame stabilization for any value of k as shown in Fig. 1.9. Therefore, for $Le < 1$, it is expected that long wavelength disturbance causes unstable flame because of destabilizing contribution by mass diffusion effects, however, that short wavelength disturbance causes stable flame because stabilizing contribution by curvature effects becomes predominant in global flame stability.

Meanwhile, for $Le > 1$, the flame is always stable when hydrodynamic instability is absent. However, Joulin and Clavin [13] theoretically predicted flame front with traveling wave or pulsating instability at sufficiently high Le and β. This phenomenon, which occurs periodically with radial wave movement, is different type of instability with previous instabilities. More precise explanation will be described in Section 1.2.5.

In this Section, diffusive-thermal instability included two types of contribution for flame stability is discussed. One is destabilizing effect at $Le < 1$ and the other one is stabilizing effect at $Le > 1$. Also, another stabilizing contribution is described as thermo- diffusively stable effect by flame curvature. The global stability simultaneously included various instabilities as mentioned above will be taken into account in next Section.

1.2.4 Dispersion relation

Reconsidering the linear stability of a planar flame composed of D–L instability, diffusive-thermal instability and curvature effect (relaxation effect), Sivashinsky [16, 17] firstly found and derived the dispersion relation for the growth rate, $\sigma_{\text{lin.}}$, of small amplitude wrinkling with wavenumber, k, which is given by:

$$\sigma_{\text{lin.}} = \left(\frac{E_{\text{ex.}}}{E_{\text{ex.}}+1} \sqrt{\frac{{E_{\text{ex.}}}^2 + E_{\text{ex.}} - 1}{E_{\text{ex.}}}} - 1 \right) S_L k + \alpha [\tfrac{1}{2}\beta(1 - Le) - 1] k^2 - 4\alpha \delta_{\text{f}}^2 k^4. \qquad (1\text{-}19)$$

Here, the term of the r.h.s. of Eq. (1-19) has three parts: D–L, diffusive-thermal, curvature in order each term, respectively. R–T instability is excluded in Eq. (1-19) in order to avoid complexity of calculation. The role of curvature effect suppresses instability at large k (small wavelengths) because of negative fourth-order term, while D–L instability enhances unstable phenomena of combustion at small k (large wavelengths) due to positive linear correlation with the growth rate. For Le effects, it depends on whether Le is larger than Le_{c} or not.

To estimate Le effects on the global flame stability more clearly, Figure 1.12 shows the linear dispersion relation according to Eq. (1-19) with different Le. For the initial stage corresponding to long wavelength disturbances, the growth rate increase from zero regardless of Lewis numbers. This result is good agreement with Sivashinsky analysis [16, 17] in which D–L instability plays an important role at small wave numbers. For $Le < Le_{\text{c}}$, the growth rate reaches a maximum value at the critical wave number. When the wave number further increases, the growth rate steadily decreases. After then, the growth rate becomes negative when the wave number is larger than a marginal wave number. For $Le > Le_{\text{c}}$, the trend of global flame stability is the same with the small Le, however, both the marginal and critical

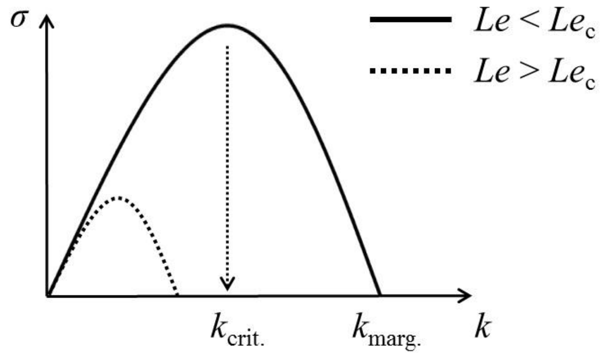

Fig. 1.12 Schematic diagram of the growth rate in global flame stability.

wave numbers are smaller than the case of $Le < Le_c$. Because the second term of the r.h.s. of Eq. (1-19) related with *Le* effects has negative value at $Le > Le_c$. In summary, unstable region of flame stability expands with large *Le*, while large *Le* contributes flame stabilization.

Equation (1-19) is assumed that the flame is perturbed with the small amplitude linear growth rate of the instability. It is well described by linearized asymptotic laminar flame theory [16, 17]. However, in reality, the flame is stabilized by geometrically finite flame shape before the wrinkled flame reaches the critical wave number. This phenomenon is concerned with the weakly nonlinear effects leading to the saturation of the amplitude of the structure. Figure 1.13 is conceptional diagram of weakly nonlinear saturation of the instability. Considering the wrinkled flame on the left picture in Fig. 1.13, the unburned fresh mixture converges to the concave flame surface by redirection of the streamline due to gas expansion (D–L instability). However, the growth of the flame amplitude by the gas expansion has limitation for intensified trough because the converged fresh mixture (finite volume) is entirely consumed by the local flame propagation at face to face slopes of the trough as shown in Fig. 1.13. After all, the intensified trough is disappeared by merging of the face to face slopes and the flame will be stable. This nonlinear effect is closed to purely kinematic in nature, rather than the reaction phenomenon [16].

However, this weakly nonlinear effect is not included in Eq. (1-19) assumed linearized

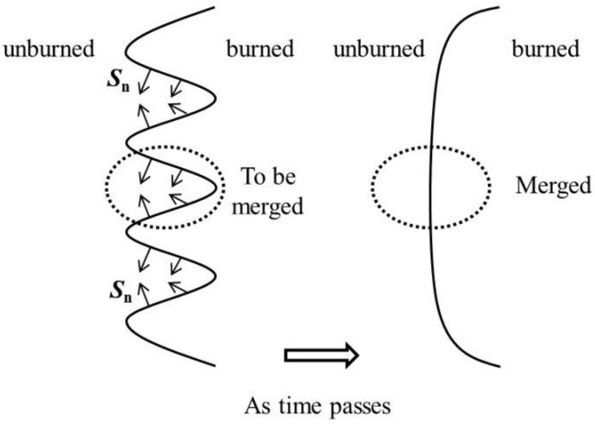

Fig. 1.13 Conceptional diagram of weakly nonlinear saturation of the instability.

instability. To describe the nonlinear evolution, nonlinear term is required by using the asymptotic expansion. Here, Sivashinsky analysis [16] is reviewed. First, the constant density model is assumed. The relative propagation speed of the flame to the gas mixture may be equal to u_b if the radius of the flame curvature is greater than the flame thickness. The movement of the curved flame, $z = F(x, y, t)$ is described by the Eikonal equation:

$$F_{DL} = u_b(1 - \sqrt{1 + (\nabla F)^2}). \tag{1-20}$$

Near the stability threshold $Le \approx Le_c$, $(\nabla F)^2 \ll 1$ is expected. Therefore,

$$F_{DL} + \frac{1}{2} u_b (\nabla F)^2 = 0. \tag{1-21}$$

Here, F_{DL} is the movement of the curved flame by D–L instability. In Eq. (1-19), there is no description of $\frac{1}{2} u_b (\nabla F)^2$ as nonlinear term. Therefore, the solution of the flame movement with instabilities is missing when Eq. (1-19) is solved at relative large amplitude.

In this Section, the global flame stability based on linear dispersion relation have been discussed and clearly confirmed difference with nonlinear theory briefly. For nonlinear theory, it does not treat any more in depth in here because of unrelated subject matter with the present paper.

1.2.5 Pulsating instability

The full dispersion relation (weakly nonlinear theory) studied by Sivashinsky [16] showed that pulsating instability, which is different type of instabilities (occurrence of periodically radial propagating wave), can be observed at:

$$\beta(Le\text{-}1) > 4(1+\sqrt{3}) \approx 11. \quad (1\text{-}22)$$

In this case of onset criterion of pulsating instability by Eq. (1-22) called as reduced Lewis number, the real and imaginary part of the growth rate, σ_{non}, are positive leading to oscillating phenomenon. Figure 1.14 shows the bottom view of the flame behavior with the different modes of pulsating instability, in downwardly propagating flame in a vertically-oriented tube opened at the top and closed at the bottom filled with a lean n-butane-oxygen mixture diluted with helium, studied by Pearlman and Ronney [18, 19]. One is target patterns (Fig. 1.14(a)) and the other one is spiral waves (Fig. 1.14(b)). These observations may be a manifestation of the pulsating instability predicted to occur in high Lewis number. Until now, there is no research for observation of certain pulsating instability (oscillating motion).

In Eq. (1-19), the second and third terms are both negative values at $Le > 1$. To exist the

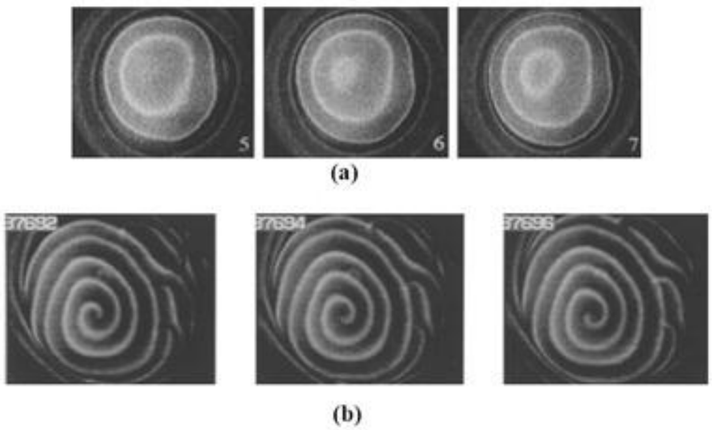

Fig. 1.14 Time sequence of target patterns and spiral waves in propagating flame front. (a) Target pattern (b) Spiral wave rotating counter-clockwise on flame front. Tube diameter is 28.5 cm i.d. and 1.5 m long in Ref. [18, 19].

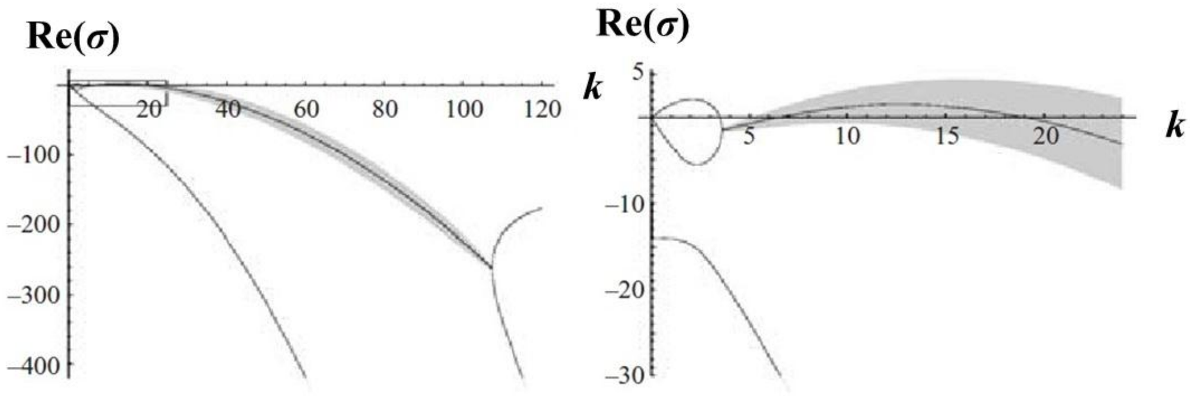

Fig. 1.15 Predicted stability and instability region at large *Le* in Ref. [20]. The figure on the right is a scale up of the boxed region in the figure on the left.

positive real value of the growth rate, σ_{non}, the gas expansion ratio, $E_{ex.}$, must be large value only at long wavelength disturbance. At short wavelength disturbance, the flame is always stable for $Le > 1$. Also, it is required to has high value of reduced Lewis number, $Le_{re.}$, for appearance of imaginary part of the growth rate in full dispersion relation [20]. Figure 1.15 shows that predicted stability and instability region at sufficiently large *Le* [20]. The instabilities occur at small wave number as shown in a picture on the l.h.s of Fig. 1.15. To make more clearly, it is showed that a figure on the right is the scale up image of the boxed region in the figure on the left. The shaded region is the complex number of the solution. Therefore, it can be expected that pulsating instability occurs from 5 to 20 of the wave number, satisfied that both of real and imaginary parts are positive.

The physical mechanism of the pulsating instability can be explained from Fig. 1.16. For $Le > 1$, the mass diffusion zone thickness is smaller than the thermal thickness. Once the flame propagates to the unburned mixture caused by pulsating mode (positive motion), the concentration gradient increases more than the temperature gradient. Thereby, the reaction zone is enriched and the flame propagation velocity increases. On the other hand, once the

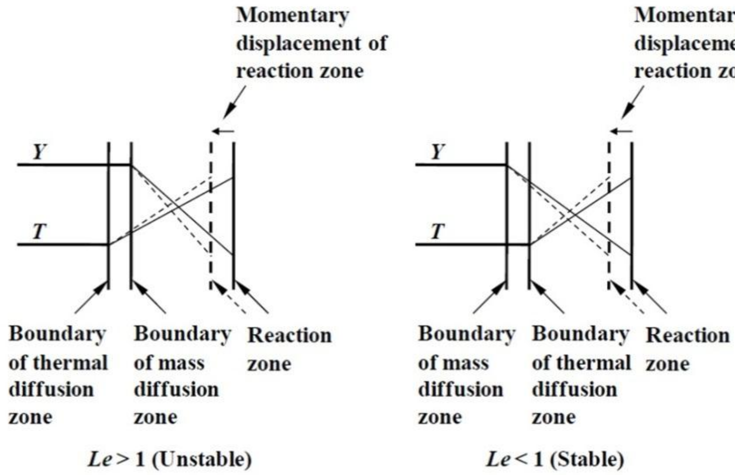

Fig. 1.16 A phenomenological mechanism of diffusive-thermal pulsating instability for the large *Le* in Ref. [21, 22].

flame propagates to the burned mixture caused by pulsating mode (negative motion), the flame propagation velocity decreases by deficient reactant. Therefore, the flame easily occurs pulsating instability for *Le* > 1 when the flame is exposed to external disturbance. However the flame with *Le* < 1 is stable for pulsating mode.

Now, the both of cellular and pulsating instabilities caused by diffusive-thermal effects are considered. According to Eq. (1-19), the flame can be stable for -2 < $Le_{re.}$ <11 determined

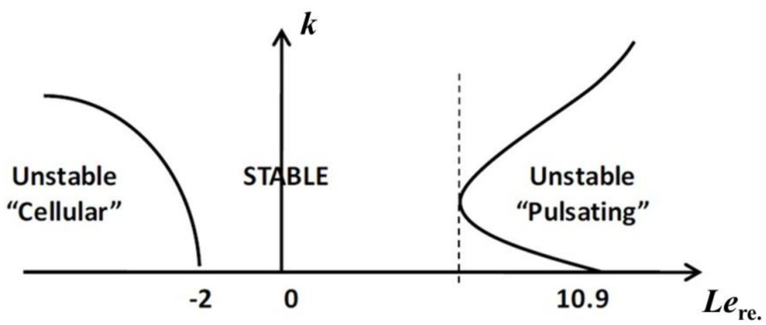

Fig. 1.17 Predicted stability and instability region for *Le* effects without heat loss in Ref. [16, 22].

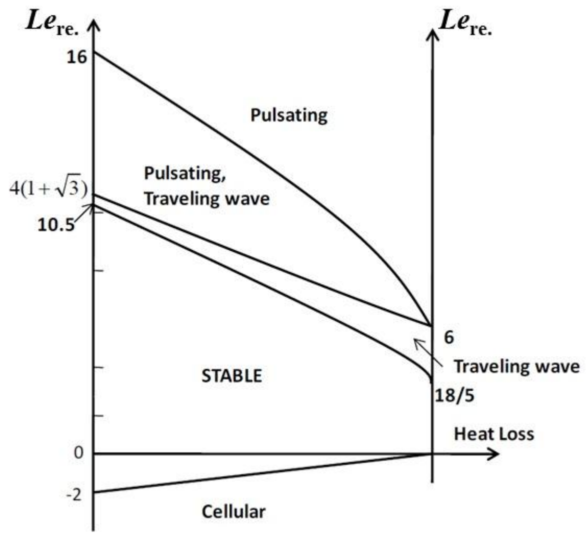

Fig. 1.18 The effect of heat loss on the diffusive-thermal instability in Ref. [13].

by evaluating solutions for Re (σ) < 0 as shown in Fig. 1.17. For -2 < $Le_{re.}$, there is only positive value of real part of solution, however, for $Le_{re.}$ <11, imaginary part of solution comes out.

Figure 1.18 shows the effect of heat loss on the diffusive-thermal instability studied by Joulin and Clavin [13]. They suggested that the critical reduced *Le* is decrease from 11 to 6 with excessive heat loss for pulsating instability as shown in Fig. 1.18. Furthermore, the critical reduced *Le* of cellular instability increases from -2 to 0. Therefore, the stabilizing region of the flame will be narrow when the heat loss is sufficiently large. The analytical results [13] give us significant information that the heat loss is one of controlling parameters for the flame stability.

1.3 Acoustic instability in combustion tube

Thermoacoustic instabilities caused by an effective interaction between heat released by a flame and acoustic fluctuations are often observed in industrial applications such as gas turbines and rocket engines [23] as shown in Fig. 1.19 (Damage of industrial burner system; (a) burner nozzle assembly and (b) Turbine blade/Bucket). It is therefore significant to suppress the instabilities, as much as possible, by an acoustically decoupled flame, in order to protect the combustors. An approach toward resolving this issue has generally been to consider the Rayleigh criterion [24]: an acoustic wave will be amplified if a time integral of the product of pressure and heat release fluctuations is positive over a pressure cycle as shown in Fig. 1.20. Particularly, the possibility of explosion at rocket engines is very high for acoustical amplification. The criterion can be mathematically expressed as follows:

$$\int p'q'dv > 0. \tag{1-23}$$

Here, p' and q' are pressure and heat release rate fluctuations, respectively. However, the Rayleigh criterion does not give us information of how to couple with pressure and heat release fluctuations. In this Section, the experimental observations conducted by Searby [25]

(a) (b)

Fig. 1.19 Damage of industrial burner system; (a) burner nozzle assembly and (b) Turbine blade/Bucket.

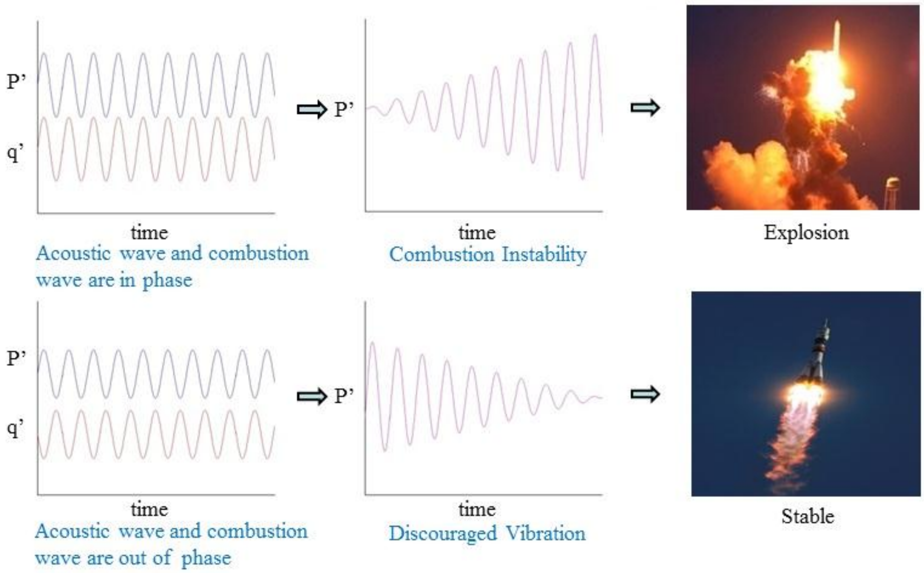

Fig. 1.20 A phenomenological mechanism of acoustical amplification and damping process.

who described the different types of acoustic instability development will be discussed. Here, a point of phenomenalistic view is only explained and a theoretical approach of coupling mechanism will be introduced in Section 1.4.1 based on Searby's experimental observation [25].

1.3.1 Primary acoustic instability

Research on such thermoacoustic instability has been conducted for a long time in various ways; experiments on a flame propagating in a tube have been the most elementarily adopted. The experimental observations by Searby [25] constitute a typical example of research in a combustion tube, which is a premixed flame propagating in an open-ended tube as shown in Fig. 1.21. Experimental method is as follows: Firstly, the flammable gas is charged in a tube and ignited at upper side of the tube. After then, the time-dependent flame behavior and the pressure temporal variation are recoded by high speed camera and pressure sensor, respectively when the flame propagates to the bottom side.

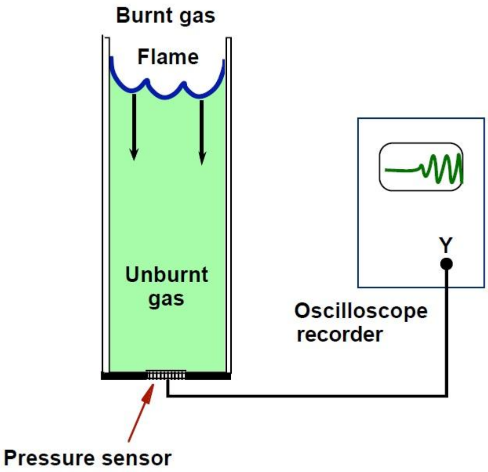

Fig. 1.21 Schematic representation of the experimental apparatus in Ref. [25].

He reported four distinct regimes of downward-propagating flames in a tube: (I) a curved flame with no acoustic sound just after ignition (see, Fig. 1.22(I)); (II) a primary acoustic instability with a flat flame surface when the flame has reached the lower half of the tube (Fig. 1.22(II)); (III) a violent secondary acoustic instability with a corrugated flame (Fig. 1.22(III)); and (IV) turbulent flame (Fig. 1.22(IV)). In connection with this explanation about the four regimes of flame behavior, Figure 1.23 describes the change of acoustic pressure in each regime. For curved flame in Regime I, no growth of pressure amplitude is observed until the flat flame appears. Once the flat flame via the curved shape appears as shown in Fig. 1.23 when the flame reaches the lower half of the tube, the acoustic pressure suddenly increases.

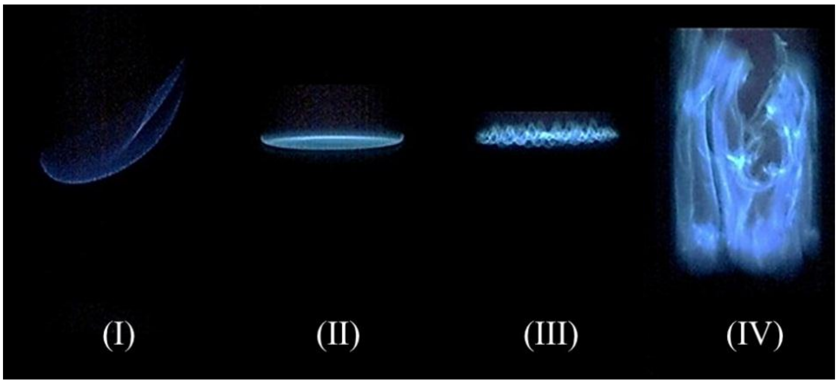

Fig. 1.22 Representative flame shapes under acoustic influences; (I) curved flame, (II) flat flame, (III) corrugated flame and (IV) turbulent flame.

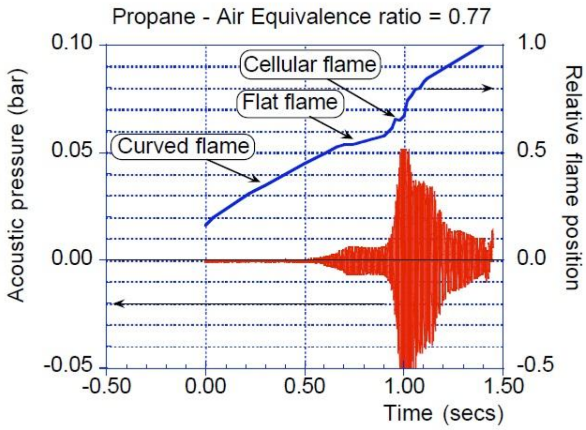

Fig. 1.23 Pressure record of acoustic instability of a premixed propane-air flame propagating in a tube in Ref. [25].

After then, the acoustic pressure is saturated and the vibrating flat flame maintains its shape. This is a typical feature of the primary acoustic instability. Once the corrugated structure via ice-cream flame appears as shown in Fig. 1.22(III), the acoustic pressure exponentially increases (as called the secondary acoustic instability). Finally, the turbulent motion appears with a breakdown of the coherent corrugated structures, and the acoustic pressure simultaneously decreases. Here, the primary acoustic instability is most important feature of the whole process because the secondary acoustic instability is caused by pre-existing finite-amplitude of the primary vibration.

To explain the mechanism of the primary acoustic instability, various mechanisms are proposed. Firstly, Kaskan [26] has suggested that the coupling is required to variations of the flame surface area within the acoustic boundary layer close to the walls of the tube. Although it is expected that the primary acoustic sound is generated when the acoustic boundary layer thickness is smaller than the quenching distance, the experimental verification is failed. Therefore, this mechanism is not valid any more. Until now, two mechanisms have been considered to provide a reasonable explanation for the generation of primary acoustic instability by propagating flames in tubes: the direct sensitivity of the reaction rate to acoustic pressure [27, 28] (called as pressure coupling in the present work) and the variation in the flame surface area induced by acoustic acceleration [29, 30] (called as acceleration coupling in the present work). In the present paper, the main focus is to provide experimental evidence regarding which is the dominant mechanism between pressure coupling and acceleration coupling for the onset of primary acoustic instability of downward-propagating flames in a tube. The more detail explanation of the both coupling mechanisms (pressure and acceleration couplings) will be discussed in Section 1.4.

1.3.2 Secondary acoustic instability

The physical initiation mechanism of the secondary acoustic instability is periodic acceleration of the flame separating dense and tenuous regions, which is similar to Faraday instability [31]. The vibrating corrugated structure oscillates with a period that is twice the acoustic period as shown in Fig. 1.24. The half frequency of vibrating motion was first noticed by Markstein [32]. He suggested that this parametric instability is driven by a time dependent modulation of the restoring force by diffusive-thermal stabilizing effect for strong acoustic acceleration.

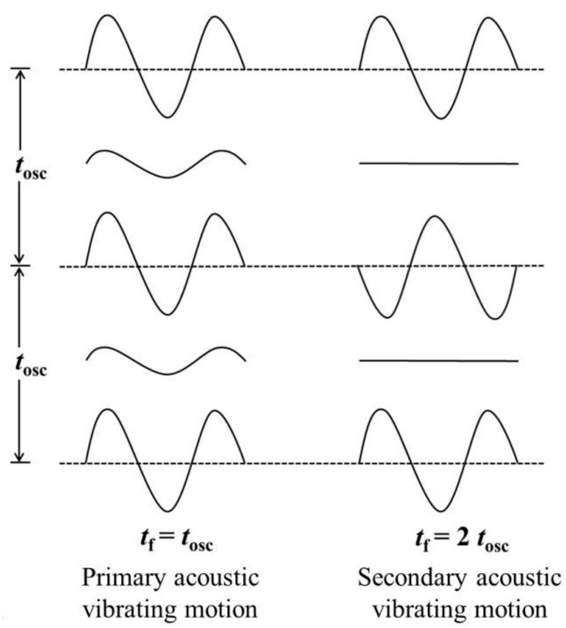

Fig. 1.24 Flame behaviors induced by primary and secondary acoustic instabilities in Ref. [32].

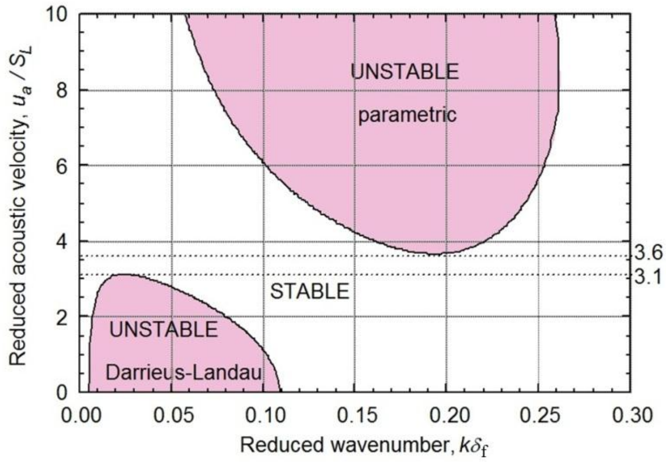

Fig. 1.25 Regions of stability and instability of a periodic acoustic acceleration in Ref. [33].

To consider it more clearly, Figure 1.25 reviews the stability diagram of acoustic instability in Ref. [33]. Here, u_a is acoustic velocity and δ_f is flame thickness. The lower pocket of instability at small wave number and low acoustic amplitudes corresponds to the D–L instability and the blank space corresponds to the primary acoustic instability. At larger acoustic levels, the upper pocket is subjected to a secondary acoustic instability. The rest area is applicable to the primary acoustic instability. The small wave number is required of higher reduced acoustic velocity to generate the primary acoustic instability, although the large wave number easily causes. As mentioned above, the strong pre-existing finite-amplitude of the primary vibration is needed to observe the secondary acoustic instability as shown in Fig. 1.25. However, a theoretical study describing the growth rate is still unknown and much work remains to be fully done on this instability.

1.4 Summary of previous works

Many previous researchers [26-30] suggested different coupling mechanisms based on the Rayleigh criterion [24] for the primary acoustic instability. In this Section, two potential candidates of coupling mechanism characterizing the feedback of the primary acoustic instability on flame fronts, pressure coupling [27, 28] and acceleration coupling [29, 30] will be discussed. Firstly, the physical meaning of its mechanisms and the theoretical analysis are showed based on the estimation of the order of magnitude of the acoustic energy. Also, the strengths and weaknesses of the both mechanisms are explained. Finally, the novel solutions of the both weaknesses are suggested.

1.4.1 Pressure coupling

Initially, Dunlap [27] theoretically showed that the effect of the pressure and adiabatic temperature of an incoming acoustic wave modulates local heat release rates of a flame with the correct phase relationship. More recently, Clavin et al. [28] treated Dunlap's mechanism and reported that a total growth rate, Γ, is proportional to coupling constant, βM at small Mach number, $M \leq 10^{-3}$, when the residential time, t_{res}, is sufficiently long. The flames may overcome the damping mechanism due to heat transfer and viscous friction at the tube wall and to acoustic radiation losses at the open end of the tube when the coupling constant is adequately large ($\beta M \approx 10^{-2}$). Here, Γ is defined as $\Gamma = A_{final}/A_{initial}$ where A_{final} and $A_{initial}$ are the final and initial amplitude of the perturbation. These explanations can be understood by the fact that the reaction rate will increase with pressure since the chemical reaction rate is proportional to the density according to Arrhenius law:

$$\Omega = A_p \rho m exp(-\frac{E}{RT}). \tag{1-24}$$

Here, A_p is the Arrhenius rate prefactor, ρ is the density, m is the mass fraction of the limiting reactant, E is the activation energy, R is the gas constant and T is temperature. Also, the gas temperature fluctuates with the pressure oscillation because acoustic waves are adiabatic:

$$\frac{\delta T}{T} = \frac{C_p - C_v}{C_p}\frac{\delta p}{p}, \tag{1-25}$$

where C_p and C_v are specific heat under constant pressure and volume, respectively. Since the Zel'dovich number is a nondimensional measure of the sensitivity of the reaction rate to temperature variations, acoustic pressure will be amplified for large β. However, for sufficiently large Mach numbers, $M \geq 5 \times 10^{-3}$, a strong acoustic instability cannot appear [28] because the transit time is much shorter than the acoustic time, $\tau_t \ll \tau_a$. Thus, the violent acoustic instability is predicted to appear at sufficiently small Mach numbers, $M \approx 10^{-3}$ ($\tau_t/\tau_a \approx O(1)$), when β is sufficiently large. Unfortunately, the mechanism of pressure coupling has limitations, which can be applied only for planar, rather than curved, flames, and the initial growth rate of the acoustic instability measured by experiments for nonplanar flames [34] is two to three orders of magnitude higher than that expected by the theoretical prediction of Clavin et al. [28]. Thus, this analysis is very hard to apply to real combustion experiments since propagating premixed flames in an actual combustor do not take on a planar structure owing to exposure to hydrodynamic instabilities (e.g., D–L instability and gravity effects). Nevertheless, there is ample room to appraise the coupling constant, βM, for fully developed flat flames (the saturated region of acoustic pressure) in the primary acoustic instability. Also, when a tube with short length is used, the coupling constant can be bigger than long tube to observe the primary acoustic instability because of excessive acoustic losses.

Now, the estimation of the order of magnitude of pressure coupling [28] is reviewed for the generation of primary acoustic instability at propagating flames in tubes.

The time derivative of the total energy per unit cross-sectional area, $d\varepsilon/dt$, is given as follows:

$$\frac{\mathrm{d}\varepsilon}{\mathrm{d}t} = \delta P(\delta u_{\mathrm{b}} - \delta u_{\mathrm{u}}). \qquad (1\text{-}26)$$

Here δP is the pressure fluctuation, δu is the velocity fluctuation and the subscripts u and b identify unburned and burned mixtures, respectively. For the pressure jump across the flame, it is of order ρU^2, where ρ is the density and U is the flame velocity, and it is much smaller than the variations in the acoustic wave, ρc^2, where c is the speed of sound. Thus, it can be supposed that pressures are equal on both sides of the flame. Considering Rayleigh criteria, the main problem in Eq. (1-26) is how to link $(\delta u_{\mathrm{b}} - \delta u_{\mathrm{u}})$ to δP in phase. Because, the gas expansion, $(\delta u_{\mathrm{b}} - \delta u_{\mathrm{u}})$, is proportional to the fluctuation of the rate of heat release per unit cross-sectional area, δq.

For simplicity of calculation, a one-step reaction with large activation energy is assumed and the chemical reaction occurs in a thin region since the inverse of β implies an effective dimensionless width of the reaction zone [35]. In the present work, Zel'dovich number can be calculated [5] as follows:

$$\beta = E(T_{\mathrm{b}} - T_{\mathrm{u}})/(RT_{\mathrm{b}}^2). \qquad (1\text{-}27)$$

Peters and Williams [36] define the activation energy, E, as follows:

$$\frac{E}{R} = -\frac{\mathrm{d}2[\ln(\rho_{\mathrm{u}} S_{\mathrm{L}})]}{\mathrm{d}(1/T_{\mathrm{b}})}. \qquad (1\text{-}28)$$

A small relative variation in the flame temperature induces a modification to the laminar flame velocity, S_{L}, and the heat flux, q, of order unity:

$$\frac{\delta T_{\mathrm{b}}}{T_{\mathrm{b}}} = O(\frac{1}{\beta}) \Longrightarrow \frac{\delta S_{\mathrm{L}}}{S_{\mathrm{L}}} = O(1) \text{ and } \frac{\delta q}{q} = O(1). \qquad (1\text{-}29)$$

In the conservation equation of enthalpy, the relative variation in temperature and pressure in an acoustic wave are of the same order of magnitude:

$$\frac{\delta T}{T} \approx \frac{\delta P}{P} \approx \frac{\rho c \delta u}{P} = M\left(\frac{\delta u}{S_\mathrm{L}}\right). \quad (1\text{-}30)$$

According to (1-29), this temperature fluctuation induces a modification of the flame structure and of the heat release of the order $\beta M(\delta u/S_\mathrm{L})$. For a relative gas expansion across a discontinuity surface, one may expect the same order of magnitude for the relative velocity jump across the flame to be as follows:

$$\frac{\delta u_\mathrm{b} - \delta u_\mathrm{u}}{S_\mathrm{L}} \approx \beta M\left(\frac{\delta u}{S_\mathrm{L}}\right). \quad (1\text{-}31)$$

The energy per unit cross-sectional area, ε, which is stored in the acoustic mode of the tube, is of order ($\tau_\mathrm{a}\delta u \delta P$). Therefore, the characteristic order of magnitude of the growth rate of such an acoustic instability, $1/\tau_\mathrm{ins} \equiv \varepsilon^{-1}\,\partial\varepsilon/\,\partial t$, according to (1-26) and (1-31) would be the following:

$$\frac{1}{\tau_\mathrm{ins}} \approx \frac{\beta M}{\tau_\mathrm{a}}. \quad (1\text{-}32)$$

Thus, the growth rate of the acoustic instability of planar flames is proportional to the coupling constant, βM.

1.4.2 Acceleration coupling

Another mechanism was proposed by Markstein [29], who suggested that the acoustic pressure modulates a flame shape and can lead to a parametric acoustic instability. An analytical analysis of this mechanism was further performed by Pelcé and Rochwerger [30] in connection with the experiments conducted by Searby [25]. They studied acceleration coupling produced by Darrieus–Landau (D–L) instability and demonstrated that the growth rate of the primary acoustic instability is proportional to $(ak)^2$, where a is an amplitude and k is a wave number of the curved flame. Also, they used a more complete model for flame dynamics that adopted stability limits of the D–L instability [4] and gravity effects into the problem in order to estimate a situation close to that of real propagating flames. The fundamental principle of this mechanism can be understood as follows: the sufficiently large amplitude of the wrinkled flame caused by D–L instability causes deviation of the flow lines in front of the flame, and velocity gradients across the flame increase. After then, the increasing velocity gradients induce change in the flame surface area in phase with pressure fluctuation, and then the primary acoustic sound is generated. Finally, the variation in the flame surface area caused by the acoustic velocity field forces the amplification of the primary acoustic sound and the flame becomes flat by the parametric force [25, 30, 33]. Their calculation indicates that the maximum growth rate of the acoustic pressure takes place when the flame has reached the lower half of the tube, which is in good agreement with Searby's experimental observations [25]. It should be noted that the flame amplitude by D–L instability changes in a weakly nonlinear trend rather than a neutrally stable mode. However, Pelcé and Rochwerger [30] described a constant amplitude in their calculation. Thus, it is required to consider the weakly nonlinear trend of D–L instability to confirm effect of acceleration coupling. However, a and k are very hard to control experimentally; because the initial curved flame is intrinsically unstable, even the effect of a and k is significant in the instability mechanism. To solve this problem, the novel CO_2 laser-irradiation method is utilized to control the shape of the freely propagating flames, which is supported to estimate acceleration coupling. More detail explanation of CO_2 laser-irradiation will be discussed in Section 1.5.

Now, the estimation of the order of magnitude of acceleration coupling [30] is reviewed for the generation of primary acoustic instability at propagating flames in tubes. Pelcé and Rochwerger [30] introduced a new transfer function defined as follows:

$$Tr = \frac{(\delta u_{\mathrm{b}} - \delta u_{\mathrm{u}})}{\delta u_{\mathrm{u}}}. \tag{1-33}$$

When the mass conservation equation crossing the flame is considered, the amplitude of the outgoing wave in the burned mixture is determined by the following relation:

$$\delta u_{\mathrm{b}} - \delta u_{\mathrm{u}} = \left(\frac{\rho_{\mathrm{u}}}{\rho_{\mathrm{b}}} - 1\right) S_{\mathrm{L}} \delta S, \tag{1-34}$$

where δS is the perturbation of the normalized flame area. Thus, the growth rate of the acoustic instability of curved flames is proportional to $(ak)^2$ because of the relation $S = 1 + \frac{1}{4}(ak)^2$ [30].

1.5 Objective of present research

In this Section, the novel method shall be introduced, CO_2 laser-irradiation method, to change the flame surface area of the freely propagating flames. This method gives us very creative way to judge by Pelcé and Rochwerger's suggestion, acceleration coupling [30]. On the other hand, the utilization method of various gas compositions for lean ethylene flames diluted with carbon dioxide or nitrogen is also described to confirm validity of pressure coupling [27, 28]. Finally, the importance of evaluation of *Le* effect on the primary acoustic instability and its estimation method will be explained.

1.5.1 Motivation

To understand whole process of the acoustic instability in propagating flame in combustion tube, it is preferentially required to deduce coupling mechanism of the primary acoustic instability. In last Section, previously proposed mechanisms were introduced, pressure coupling [27, 28] and acceleration coupling [29, 30] on primary acoustic instability.

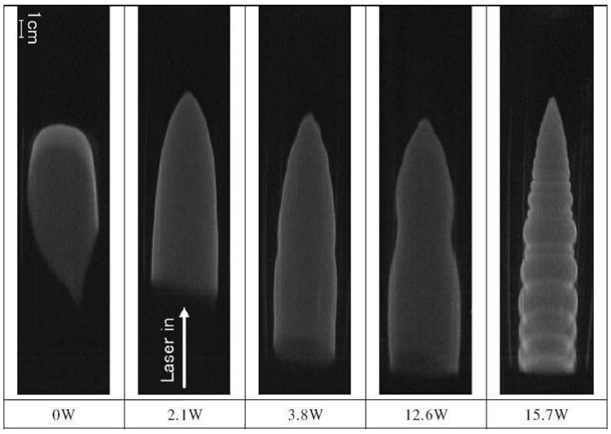

Fig. 1.26 Still images of propagating ethylene-air premixed flames with various applied laser powers in Ref. [37].

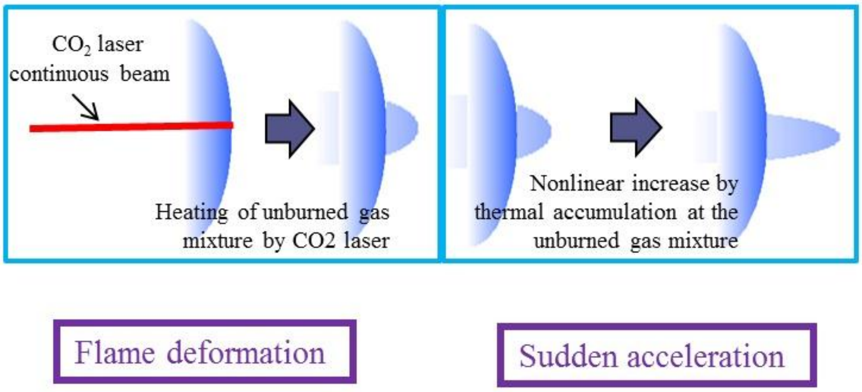

Fig. 1.27 Acceleration mechanism induced by CO_2 laser-irradiation method in ethylene premixed flames.

Unfortunately, which mechanism is more dominant remains an open question even though both mechanisms have satisfied Rayleigh criteria according to theoretical studies. To find the answer, both mechanisms must be experimentally estimated in the same gas compositions. However, to control the flame surface area systematically is very difficult without any change of the gas compositions.

To solve this problem, the novel CO_2 laser-irradiation method is utilized to control the shape of the freely propagating flames. Tsuchimoto et al. [37] investigated the oscillating motion of an upward-propagating flame in a tube induced by the CO_2 laser irradiation method, which forms a convex flame surface with the desired dimension toward the unburned mixture as shown in Fig. 1.26. Figure 1.27 shows more detail acceleration mechanism induced by CO_2 laser-irradiation method in ethylene premixed flames. The external laser irradiation preheats an unburned mixture locally in front of a reaction zone, and the flame propagation velocity increases locally. Because ethylene gas plays an important role as the main absorption medium of CO_2 laser light. Therefore, the flame front acquires a strongly curved shape. This method is also allowed to evaluate nonlinear growth of D–L instability. Park et al.

[38] have conducted experiments on downward-propagating flames with CO_2 laser light and have observed a unique deformation of the flame surface (called an "ice-cream flame" in present work) from a flat flame surface caused by the primary acoustic instability when the flame front is exposed to CO_2 laser light. Since then, Taniyama and Fujita [39] have examined the criteria of a transition from the primary to the secondary acoustic instability induced by a short-term CO_2 laser-irradiation method. In their research [38, 39], however, the growth rate of primary acoustic instability depending on variations of flame surface areas was not discussed.

The main purpose of this paper is to provide experimental evidence regarding which is the dominant mechanism between pressure coupling and acceleration coupling for the onset of primary acoustic instability the dependence of change in the coupling constant, βM, and the effects of variation in the flame area on the primary acoustic instability of downward-propagating flames in a tube by using CO_2 laser-irradiation method.

1.5.2 Scope of present research

In the present thesis, more dominant mechanism between pressure coupling and acceleration coupling on the generation of the primary acoustic instability is established by experimental research. To do that, it is necessary to take into account simultaneously both mechanisms in the same gas composition. After then, the effect of the Lewis number on the primary acoustic instability in non-equidiffusive flames will be investigated based on the correct mechanism. In general, the chemical reaction rate becomes more sensitive to variations in gas temperature with decreasing Lewis number [40, 41]. This has a significant effect on the enhancement of acoustic sound, because gas temperature fluctuation is generated from acoustic pressure fluctuation under constant enthalpy, whereas the effect of *Le* was not investigated in previous studies [25, 34]. In contrast, Clavin et al. [28] theoretically predicted strong acoustic instability when *Le* > 1, which is caused by pulsating instability, first pointed out by Sivashinsky [17]. Unfortunately, this instability has never been observed experimentally because the critical *Le* required theoretically is beyond the range of real flames. Another important consideration is how the cellular instability associated with diffusive thermal effect affects the generation of acoustic sound. Generally, the cellular instability appears at *Le* < 1 as mention Section 1.2.3. The wavelength is relatively shorter than the D–L instability caused by the thermal expansion of an unburned mixture through the flame front. However, the previous experiment [25] only considered D–L instability for lean propane flames without cellular structures. Therefore, an experimental study of the *Le* effects is required to estimate the primary acoustic instability with effect on the flame's shape.

The rest of the paper is to investigate the effects of acoustic losses on the primary acoustic instability. Generally, the acoustic losses depend on the geometries of combustion chambers and on the nature of the gaseous medium. Experimental observations of damping effects in different gaseous media with different thermal diffusivities and kinematic viscosities in an identical tube will be presented.

Chapter 2: Experimental setup

The experimental apparatus is schematically outlined in Fig. 2.1a. The propagation tube (transparent acrylic tube, 50-mm inner diameter and 511-mm length for Chapter 3 and 4; 50-mm inner diameter and 711-mm length for Chapter 5) is fixed vertically and charged with the tested gas at atmospheric pressure. To artificially change the flame area, the CO_2 laser-irradiation method is utilized. Ethylene gas plays an important role as the main absorption medium of CO_2 laser light according to the NIST chemical database [42]. The CO_2 laser beam (beam diameter: 3.3 mm, SYNRAD Firestar v20, wave length: 10.6 μm) vertically passes along the center of the tube. The specification of CO_2 laser is shown in Table 2.1. A point ignition system using a spark plug is located near the upper end of the tube. When the spark igniter is activated, the top lid (see, Fig. 2.2) is simultaneously opened by an automatic opening system of the top lid of the tube powered by an electromagnet and a mechanical spring.

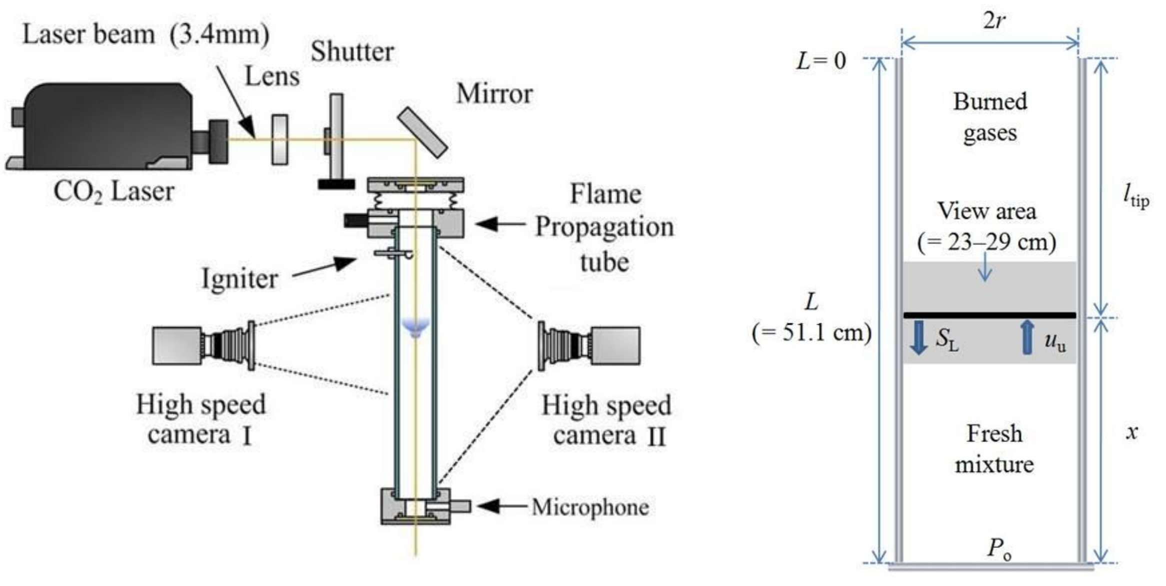

(a) (b)

Fig. 2.1 (a) Schematic drawing of the experimental setup and (b) general configuration.

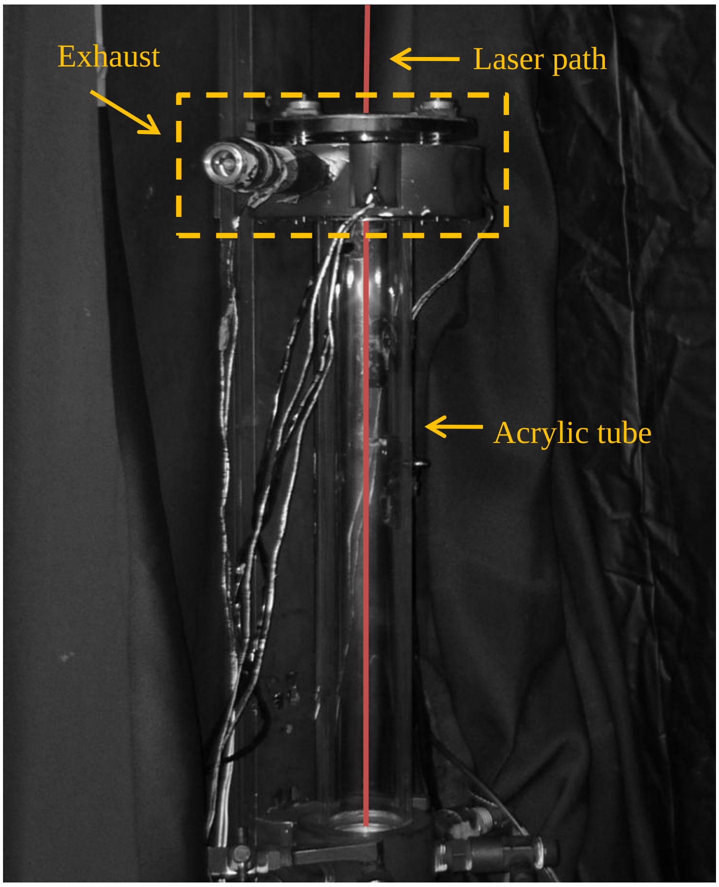

Fig. 2.2 Direct photo of propagation tube.

Table 2. 1 Specification of CO_2 laser.

Model	SYNRAD firestar v20
Wavelength	10.57 ~ 10.63μm
Output Power	20W
Power Stability	±5% (cold start) ±3% (After 2 minutes)
Beam Diameter	2.0mm±0.5mm
Beam Divergence	<7.0mRad
Rise Time	< 100μsec
Ellipticity	<1.2

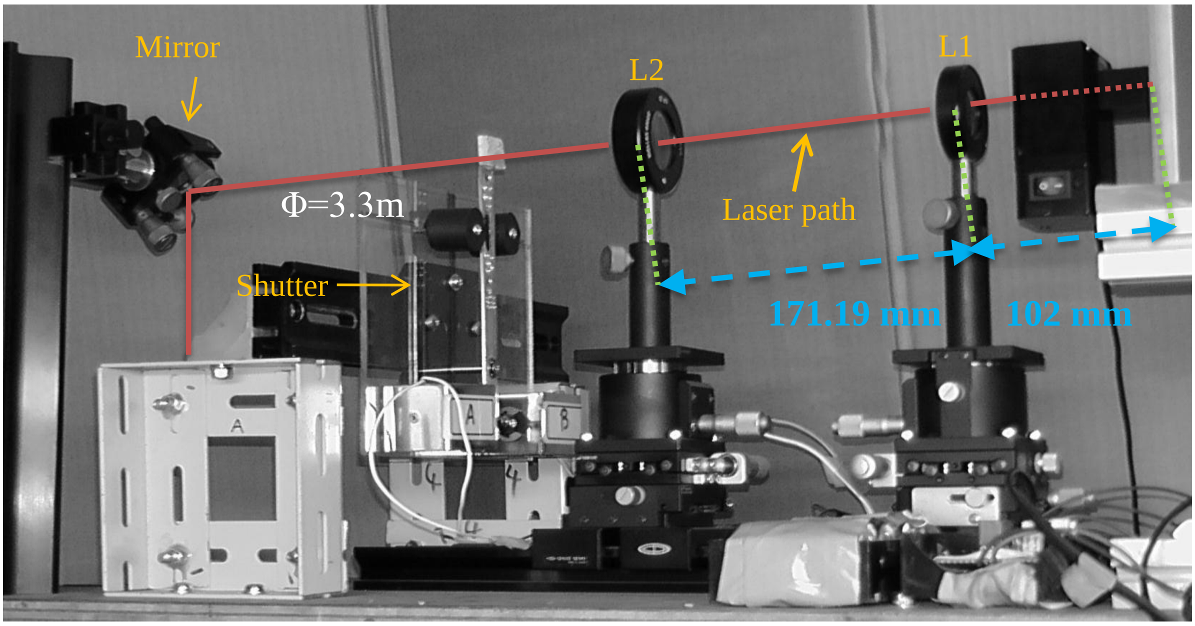

Fig. 2. 1 Direct photo of optical setup.

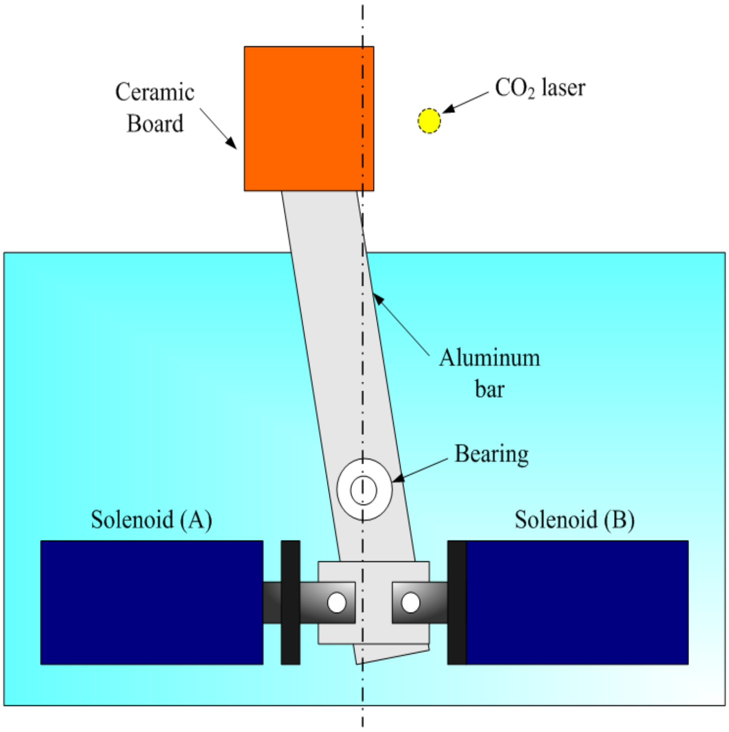

Fig. 2. 2 Schematic diagram of mechanical shutter.

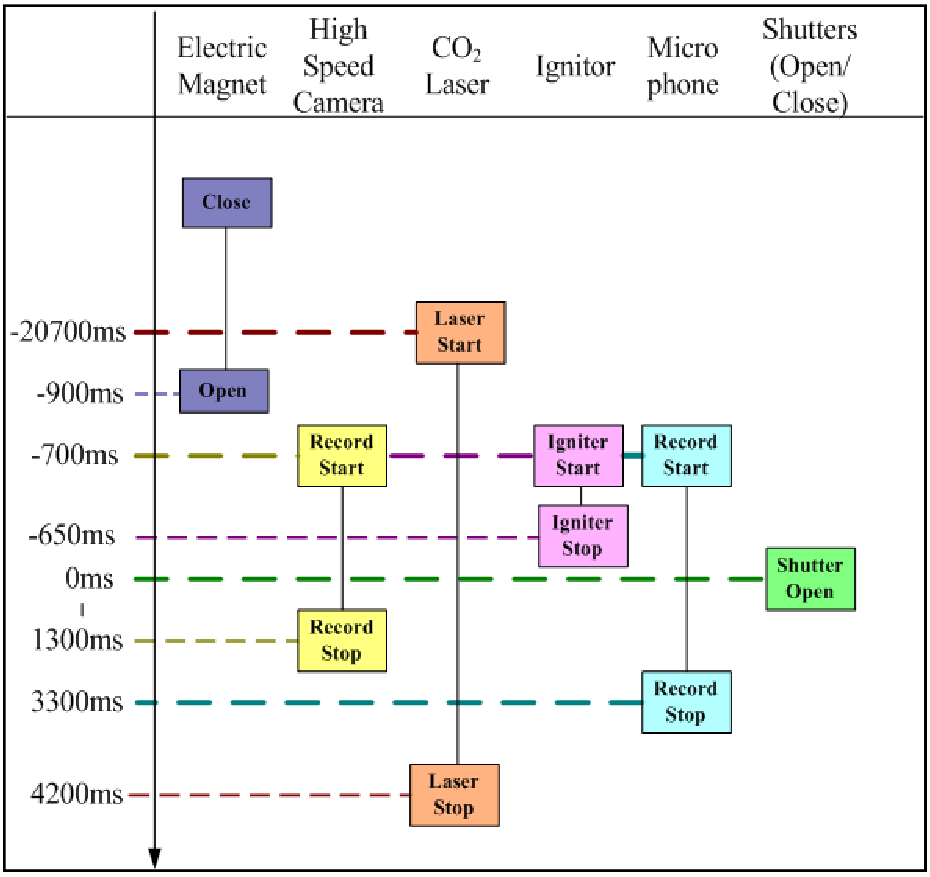

Fig. 2. 5 Time schedule of system sequence.

The direct photo of optical setup is illustrated in Fig.2.3. The focusing lenses (OPHIR DURA-LENS**)** are made of Zinc Selenide (ZnSe) with an anti-reflective coating. In order to ensure parallel laser beam, it is crucial to set exact optical arrangement. The focusing lenses are Meniscus (L1, focusing length: 63.5 mm) and Plano-Convex (L2, focusing length: 95.25 mm) as shown in Fig.2.3. Mechanical shutter is set in the laser path to control the exposure time and onset time of laser beam. Fig.2.4. depicts the schematic outline of mechanical shutter. To control the exposure time of CO_2 laser, the ceramic board as a shutter (powered by two solenoids) closes and opens according to expected time sequence.

The time-dependent behaviors of the downward-propagating flame are recorded by two high-speed cameras. One of the high-speed cameras (IDT MotionPro X-4 recording at 2000 fps) captures images from 230 to 290 mm from the upper side of the tube, as illustrated as the shaded region in Fig. 2.1b. In Searby's work [25], he observed that the primary acoustic sound occurs when the flame has reached the lower half of the tube. Therefore, half of the tube is an appropriate field to observe the generation process of the primary acoustic instability, and this captured region is called as "view area" in the present work. Another high-speed camera (nac HSV-500C[3] recording at 500 fps) captures whole images of the propagating flames in the tube. In cases of laser -irradiation, a flame front is exposed to laser light when the flames reach 230 mm from the upper end of the tube, and this moment is defined as t = 0.0 ms in the present study. Pressure temporal variation is measured with a PCB Piezotronics 106B52 dynamic pressure sensor located at the bottom end of the tube at a sampling rate of 10 kHz. System sequence is controlled by the programmable controller (MITSUBISHI, FX_0-20MR). The time schedule of the system sequence for continuous laser beam is shown in Fig. 2.5. The onset of the laser exposure is defined as t = 0.0 s in the present study.

Chapter 3: Establishment of coupling mechanism of primary acoustic instability

In Chapter 3 to establish coupling mechanism of the primary acoustic instability, the premix gas composed of ethylene, oxygen, carbon dioxide, and nitrogen are set at atmospheric pressure in the tube. Various gas compositions are tested in association with different acoustic losses, laminar burning velocities, adiabatic flame temperatures, coupling constant, βM, laser powers, and irradiation times as shown in Table 3.1. The flame properties (e.g., laminar burning velocities and adiabatic flame temperatures) are calculated using CHEMKIN (Premix code/ USC II) [43].

To estimate the coupling mechanisms related to the coupling constant, βM leading to the generation of acoustic sound, experiments are conducted with various coupling constants, βM, which can be varied by changing the laminar burning velocity and adiabatic flame temperature. It should also be considered with the effect of acoustic losses because the actual acoustic intensity produced by the flame can be presented as the sum of the observed acoustic intensity and the acoustic losses. Here, details concerning the calculation of acoustic losses are described in Appendix A.

Mixtures 1 and 2 are chosen to study the effect of βM with the different T_b and $1/\tau_{loss}$ under the same S_L. Comparison of Mix. 1 and 3 provide information on the effect of βM with the different S_L and T_b under nearly the same $1/\tau_{loss}$. Also, Mix. 2 and 4 give us the same information. The acoustic losses have relevance to kinematic viscosity, thermal diffusivity, and acoustic frequency, as discussed in Section 2.2. Mixtures 1, 5, and 6 allow estimation of the effect of βM with the different T_b under the same S_L and nearly the same $1/\tau_{loss}$. Mixtures

Table. 3.1 Summary of results for the tested gas in Chapter 3.

Mixture	C_2H_4	O_2	CO_2	N_2	ϕ	S_L (cm/s)	T_b (K)	α (cm^2/s)	ν (cm^2/s)	$1/\tau_{loss}$ (s^{-1})	βM	w/ or w/o laser	vibration or not
1	0.071	0.24	0.69		0.90	22	2049	0.13	0.10	8.5	0.011	with laser (0, 2, 6, 12, 18 (W))	O
2	0.040	0.14		0.82	0.84	22	1832	0.21	0.15	12.7	0.007		x
3	0.059	0.20	0.74		0.90	11	1814	0.13	0.09	8.4	0.005		x
4	0.049	0.18		0.77	0.84	40	2092	0.21	0.15	12.6	0.013		O
5	0.067	0.25	0.68		0.80	22	1988	0.13	0.10	8.5	0.010	without laser	O
6	0.063	0.27	0.67		0.70	22	1927	0.13	0.10	8.6	0.009		O
7	0.070	0.26	0.67		0.80	25	2049	0.13	0.10	8.6	0.012		O
8	0.069	0.29	0.64		0.70	29	2049	0.14	0.10	8.7	0.013		O
9	0.061	0.20	0.74		0.90	12	1851	0.13	0.09	8.4	0.005		x
10	0.063	0.21	0.73		0.90	14	1900	0.13	0.09	8.4	0.006		x
11	0.066	0.22	0.71		0.90	16	1951	0.13	0.09	8.4	0.008		O
12	0.068	0.23	0.70		0.90	19	2000	0.13	0.09	8.5	0.009		O
13	0.041	0.15		0.81	0.84	22	1850	0.21	0.15	12.7	0.007		x
14	0.043	0.15		0.81	0.84	26	1900	0.21	0.15	12.7	0.008		x
15	0.044	0.16		0.80	0.84	29	1950	0.21	0.15	12.6	0.009		x
16	0.046	0.16		0.79	0.84	32	2000	0.21	0.15	12.6	0.010		O
17	0.090	0.20	0.71		1.35	12	1817	0.13	0.09	8.4	0.004	with laser during 60 ms (0, 14 (W))	O

1, 7, and 8 enable us to elucidate the effect of βM with the different S_L under the same T_b and nearly the same $1/\tau_{loss}$. In addition, in the comparisons between Mix. 1, 9, 10, 11, and 12 as well as between Mix. 4, 13, 14, 15, and 16, the influence of variations of the coupling constant, βM on the onset of primary acoustic instability can be evaluated under the same Φ and nearly the same $1/\tau_{loss}$, respectively.

To take the coupling mechanisms featuring variations of flame areas for curved flames into account, experiments induced by CO_2 laser irradiation are conducted. In this study, the deformed single cell structure is only considered to evaluate variations of flame surface areas qualitatively for a curved structure. Mixtures 2 and 4 are nonvibrating flames at initial conditions and allow study of the potential for spontaneous generation of acoustic sound by increasing flame surface areas. Mixtures 1 and 4 provide experimental observations of the potential for change of the primary acoustic pressure from initial vibrating flames (flat flames) to convex flames (ice-cream structure) under various laser powers. Finally, the effects of growth or decline of the flame surface area induced by a short-term CO_2 laser-irradiation method on the growth rate of acoustic instability will be discussed in Mix. 17.

3.1 Pressure coupling

The Figure 3.1 shows typical downward-propagating flat flame behavior after the initial curved flame in the primary acoustic instability in Mix. 1. The numerical values at the bottom of each picture are the passage of time in the view area. A transition process from the initial curved flame to a flat flame is as follows. After ignition, a curved flame front propagates downward because of hydrodynamic instability. Then, the flame becomes flat under the presence of acoustic sound resonating at a quarter wave length. The transition from a curved flame to a flat flame occurs within 0.4 s after ignition. Figure 3.2 depicts temporal variation in the flame tip position, l_{tip}, and flame behavior (inserted pictures) with different gas

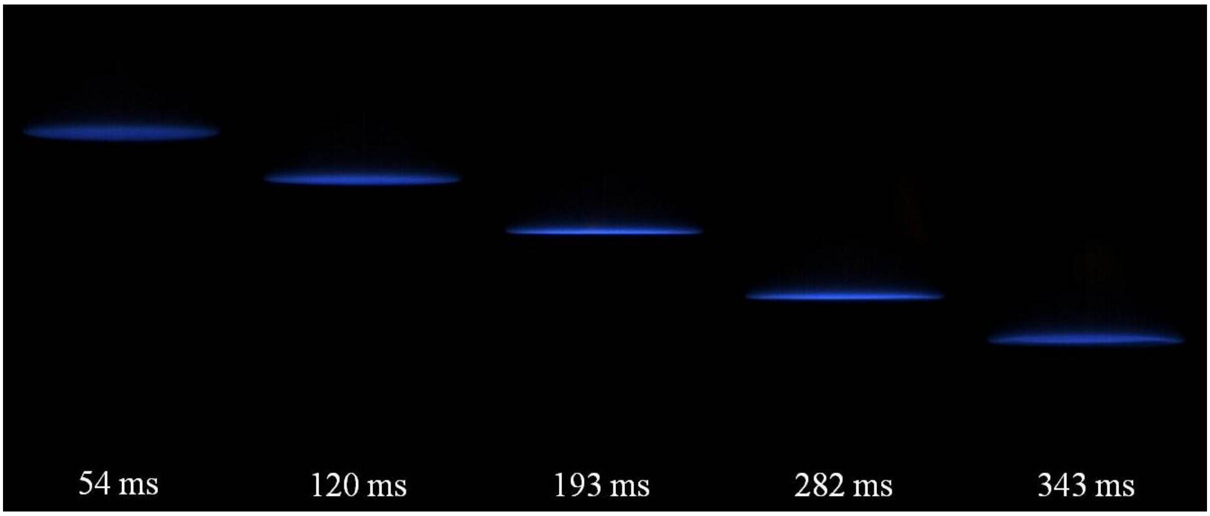

Fig. 3.1 Sequential images for a propagating flame without laser power in Mix. 1.

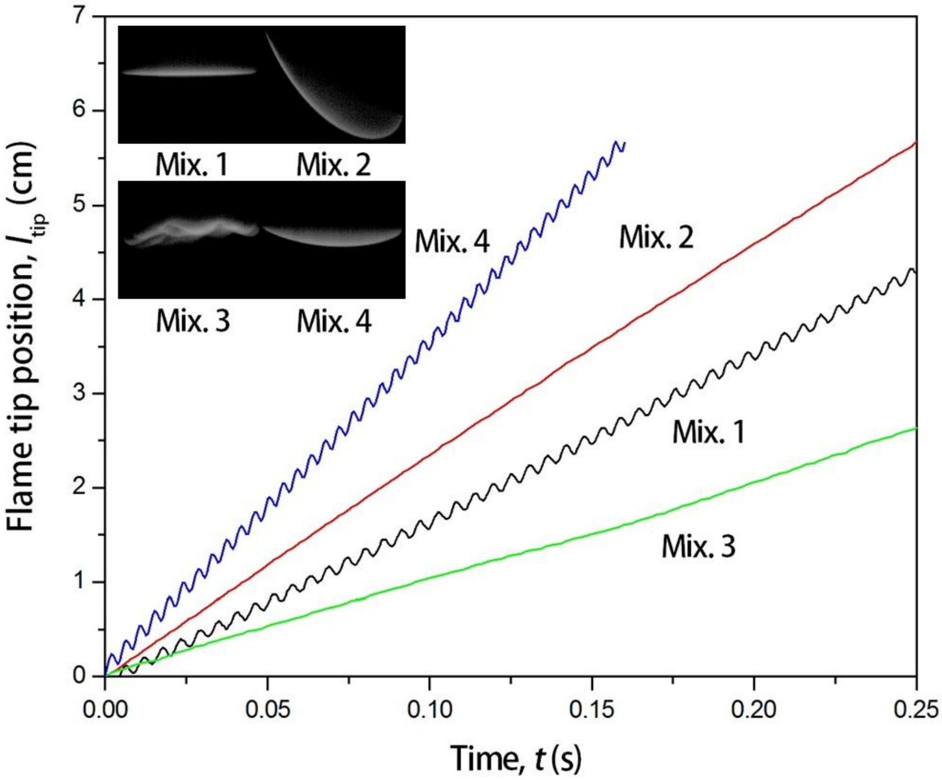

Fig. 3.2 Temporal flame tip position without laser irradiation in Mix. 1, 2, 3, and 4.

compositions at the view area. Two distinct types of behavior are identified. First, a regime of acoustic instability in which the flames are flat and vibrating, as shown in Mix. 1 and 4, is identified. Second, in a regime of nonacoustic instability, flames are curved and propagate without fluctuation, as shown in Mix. 2 and 3. The cell size in Mix. 3 is relatively smaller than that in Mix. 2, and it is not homogeneous. Thus, it is apparent that measurement of the initial flame curvature is extremely difficult in experiments. In the present study, the vibrating flame is defined as the flame with a peak-to-peak amplitude periodic oscillation over 0.03 cm. On comparing Mix. 1 and 2, the flame with relatively lower kinematic viscosity and thermal diffusivity (Mix. 1) displays periodic vibration, even with the same laminar burning velocity. Moreover, in Mix. 1, the mean flame velocity is lower than that in Mix. 2 because of the relatively small flame surface area. The mean flame velocities are 17.4 and 22.9 cm/s in Mix.

1 and 2, respectively. On comparing Mix. 1 and 3, the flame with both higher burning velocity and adiabatic flame temperature (Mix. 1) can only be observed as a vibration behavior even though both Mixtures are at nearly the same kinematic viscosity and the same thermal diffusivity. In the same way, the comparison of Mix. 2 and 4 shows that both higher burning velocity and adiabatic flame temperature tend to result in vibration behavior. As a summary of the above experimental observations, two facts can be pointed out: (1) larger kinematic viscosity and thermal diffusivity result in the suppression of acoustic vibration and (2) larger burning velocity and adiabatic flame temperature tend to cause acoustic vibration.

The acoustic losses consist of the sum of the radiative losses and wall losses (see Appendix A). In general, natural damping processes are unavoidable dissipations in flame propagation in one-end-open combustion tubes. For $1/\tau_{\mathrm{rad}}$, a faster speed of sound causes stronger acoustic radiation losses, which are considered in an identical combustion tube according to Appendix A. For $1/\tau_{\mathrm{wall}}$, high thermal diffusivity leads to a gentle radial temperature gradient and an enhancement of the thermal-penetration depth at the flame edge, and the acoustic instability can be suppressed by acoustic energy dissipation with excessive heat loss to the acoustic boundary layer. Moreover, acoustic energy losses due to viscous friction should increase with kinematic viscosity. Therefore, it is probable that the flame cannot overcome natural damping with a high speed of sound, thermal diffusivity, and kinematic viscosity in Mix. 2. In another respect, the comparison of Mix. 1 and 3 (Mix. 2 and 4) shows the effect of the coupling constant, βM [28], which can be varied by changing the laminar burning velocity and adiabatic flame temperature according to Section 1.4.1. Therefore, the temperature fluctuations associated with an incoming acoustic wave may be small enough in comparison with the natural damping effect because the coupling constants are relatively small in Mix. 3 (Mix. 2) under the same acoustic loss.

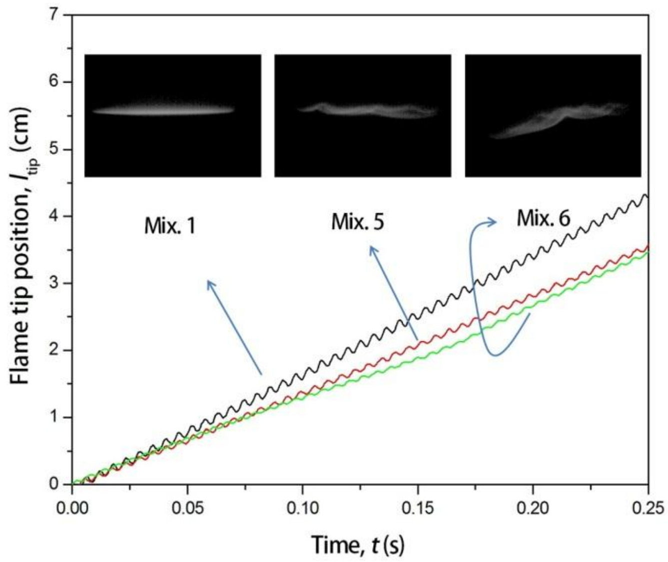

(a)

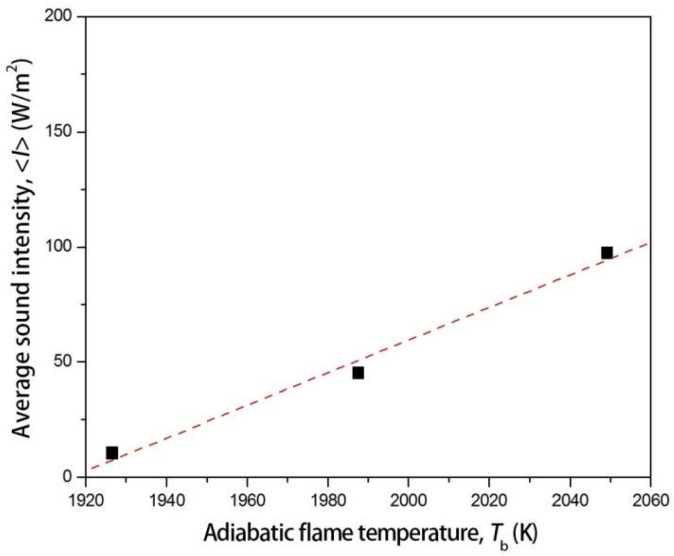

(b)

Fig. 3.3 Effect of adiabatic flame temperature on primary acoustic instability; (a) temporal flame tip position without laser irradiation and (b) average sound intensity with various adiabatic flame temperatures in Mix. 1, 5, and 6.

To show the effect of a coupling constant on the growth rate of the primary acoustic instability more clearly, additional experiments considered the effect of individual parameters

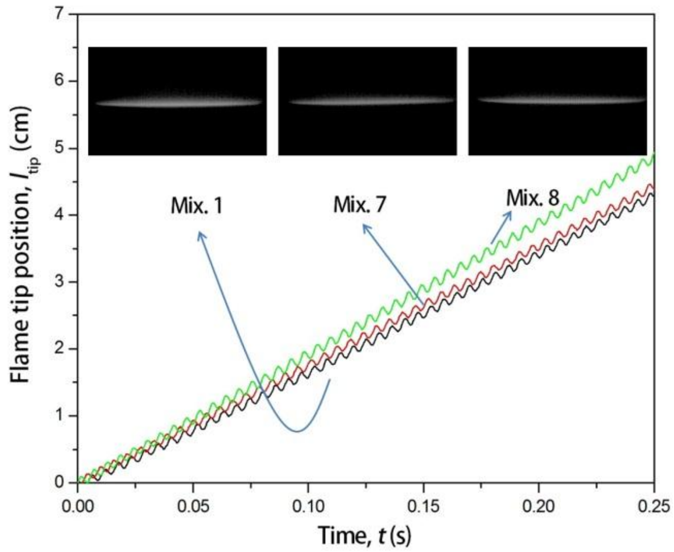

(a)

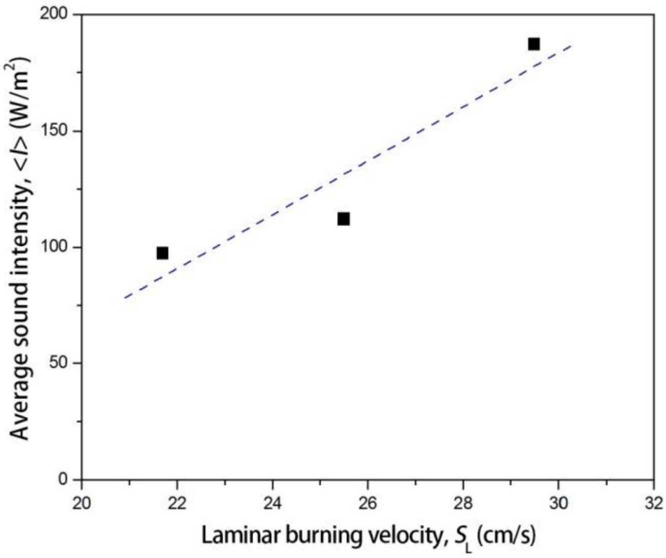

(b)

Fig. 3.4 Effect of laminar burning velocity on primary acoustic instability; (a) temporal flame tip position without laser irradiation and (b) average sound intensity with various laminar burning velocities in Mix. 1, 7, and 8.

included in the coupling constant, βM, are conducted such as the adiabatic flame temperature and the laminar burning velocity. Figure 3.3 illustrates the effects of the adiabatic flame temperature on (a) the flame tip position with time and (b) the average sound intensity with various adiabatic flame temperatures in Mix. 1, 5, and 6. The inserted pictures show flame behaviors in different Mixtures. The flames are relatively faster and have broad amplitude with a higher adiabatic flame temperature in spite of the same laminar burning velocity as 22 cm/s in Fig.3.3a. Moreover, the flame shape is closer to the flat surface as the adiabatic flame temperatures increase because of the relatively strong acoustic sound. For a quantitative estimation, the coupling constant and the average sound intensity, $\langle I \rangle$ (see, Appendix B) are compared. In Fig. 3.3b, the average sound intensity, $\langle I \rangle$, given by Eq. (B1) correlates well with the variations in the adiabatic flame temperatures.

Figure 3.4a illustrates the variation in the flame tip position with time in Mix. 1, 7, and 8. The flames have large amplitudes with higher laminar burning velocities, despite the same adiabatic flame temperature of 2,049 K. The average sound intensity increases with the laminar burning velocity in Fig. 3.4b.

When experimental results in Figs. 3.3b and 3.4b are taken into consideration, the average acoustic intensity seems to be proportional to the adiabatic flame temperature and the laminar burning velocity. Moreover, the flame shapes are flat when the average sound intensities are larger than around 100 $W\cdot m^{-2}$. It is experimentally suggested that the coupling constant, βM, dominates the average sound intensity and a critical value of the coupling constant exists to attain a flat flame by acoustic vibration.

Additional experiments are conducted to clearly investigate the effect of the coupling constant. Figure 3.5 illustrates the temporal variation in the flame tip position for different coupling constants (a) diluted with CO_2 and (b) diluted with N_2 with the same equivalence ratios and nearly the same $1/\tau_{loss}$, respectively. In the case of CO_2 dilution, the vibration motions are observed in three cases. Mix. 11 is the limit of acoustic sound detection, and then,

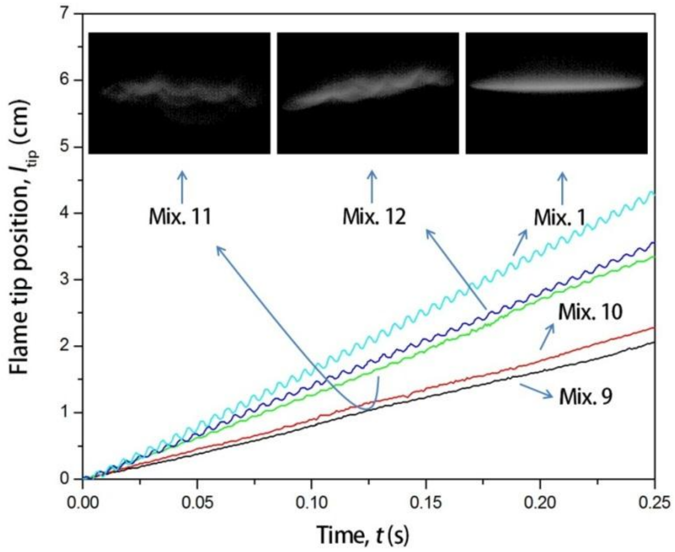

(a)

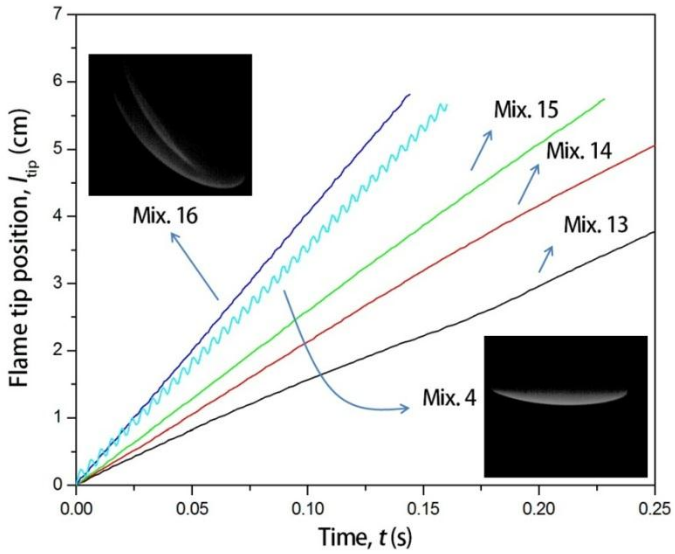

(b)

Fig. 3.5 Temporal flame tip positions without laser; (a) diluted with CO_2 at ϕ =0.90 and (b) diluted with N_2 at ϕ =0.84.

flame vibrations are more clearly observed in Mix. 12 and 1 as increasing coupling constant. In the case of N_2 dilution, the vibration motion is observed in Mix. 16 and 4, and Mix. 16 is the detection limit of acoustic vibration similar to Mix. 11. Both Figs. 3.5a and 3.5b show that

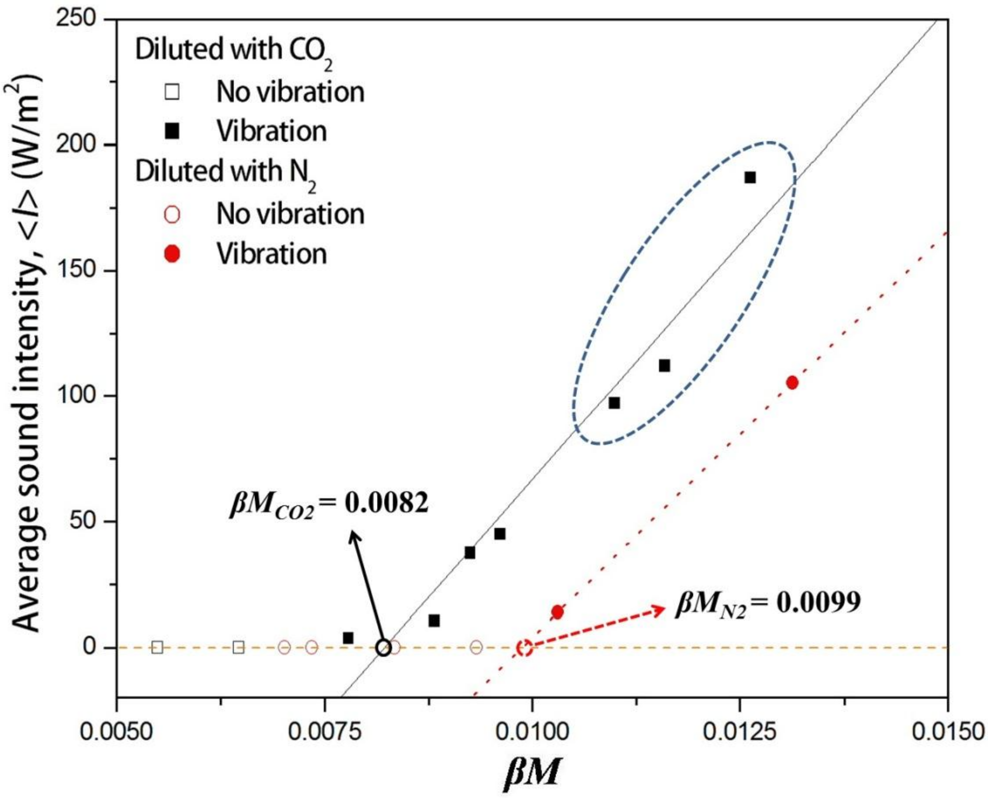

Fig. 3.6 Characteristics of the onset of the primary acoustic instability;

Dependence of the average sound intensity for primary acoustic instability on the coupling constant at various gas compositions.

increasing coupling constants tend to give increased amplitudes of vibrations.

The effect of the coupling constant on the primary acoustic instability is characterized according to the experimental observations shown so far. Figure 3.6 shows the relationship between βM and average acoustic intensity, $\langle I \rangle$. The open symbols are the no-vibration cases and the solid symbols are the vibration cases. To determine the critical coupling constant for generating the primary acoustic instability, a linear approximation between $\langle I \rangle$ and βM is established. The average acoustic intensity correlates well with the coupling constant. The best fit expressed by a solid line for lean ethylene diluted with CO_2 is $\langle I \rangle = 3.7 \times 10^4 \beta M - 309$ and the critical coupling constant, βM_{CO2}, is 0.0082. For lean ethylene diluted with N_2, the best fit expressed by the dotted line is $\langle I \rangle = 3.2 \times 10^4 \beta M - 320$ and the critical coupling constant, βM_{N2}, is 0.0099.

A difference between βM_{CO2} and βM_{N2} may result from different total acoustic loss. In previous research [28], a more precise transfer function involves the damping rate. However, for simplicity of interpretation, the coupling constant is only adopted in this study, which may cause a difference in the critical coupling constants. It is noted that curved flames are included in the plots for acoustic vibration, while the analysis by Clavin et al. [28] was exclusively based on planar flames. Nevertheless, the amplitudes of pressure vibrations are fully developed even for vibrating curved flames in the measured area (view area), and the slopes of linear approximation are coherent even if comparison is made between curved and flat flames, as shown in Fig. 3.6. Furthermore, the comparison between correlations for both CO_2 dilution and N_2 dilution suggests that larger total acoustic losses (N_2 dilution) tend to suppress acoustic intensity, even at the same coupling constant.

Meanwhile, the effects of hydrodynamic instability on the generation of the primary acoustic instability also need to be considered. Because the gas expansion ratios, ρ_u/ρ_b, also change with βM. The 3 solid symbols in the dotted circle in Fig. 3.6 indicate different coupling constants βM, with the same burnt gas temperature (2049 K). The relationship between βM and average acoustic intensity is still under the linear correlation even the expansion ratios are almost the same ($\rho_u/\rho_b \approx 0.145$) in the cases. In summary, the average acoustic intensity of the primary acoustic instability patently shows good correlation with the coupling constant, βM regardless of the gas expansion ratios.

3.2 Acceleration coupling

To artificially change the flame surface area, a CO_2 laser light is irradiated into the tube. The ethylene among the mixture components absorbs laser energy just in front of the flames. The local flame velocity should obviously increase due to the preheated unburned mixture by CO_2 laser irradiation. Thus, the flame front is locally accelerated toward the unburned mixture (e.g., convex structure). The acceleration of the local flame velocity naturally increases as the applied laser power increases.

Figure 3.7 shows the temporal of the flame tip position for different gas compositions with various laser powers. Vertical dashed-dotted lines indicate beginning of laser irradiation. The sudden increase in the propagation speed starts around 50 ms after the beginning of laser irradiation. As discussed in Section 3.1, Mix. 1 and 4 were in the regime of acoustic instability, and Mix. 2 and 3 were in the regime of nonacoustic instability without laser irradiation, as is apparent by the areas to the left of the dashed-dotted lines in Fig. 3.7. Similar to the cases without CO_2 laser light, two distinct types of behavior are identified. First, the regime of acoustic instability in which the flames finally result in turbulent motions via ice-cream structures with vibrating motions in Mix. 1 and 4; the typical flame behavior of transition processes in this regime will be discussed later. Second, the regime of nonacoustic instability in which flames have large curved cells and propagate without fluctuation, even under continuous irradiation by CO_2 laser light, as shown in Mix. 2 and 3. Control of initial flame curvature by CO_2 laser irradiation greatly facilitates qualitative evaluation on the effects of variation in the flame surface area, as shown in the inserted pictures (Mix. 2 and 3) in Fig. 3.7. It also makes it possible to implement nonlinear growth of flame surface area, which may be given by hydrodynamic instability [16, 44, 45], as shown in Mix. 2 and 3.

Pelcé & Rochwerger [30] gave the criterion for cellular thermoacoustic instability: the

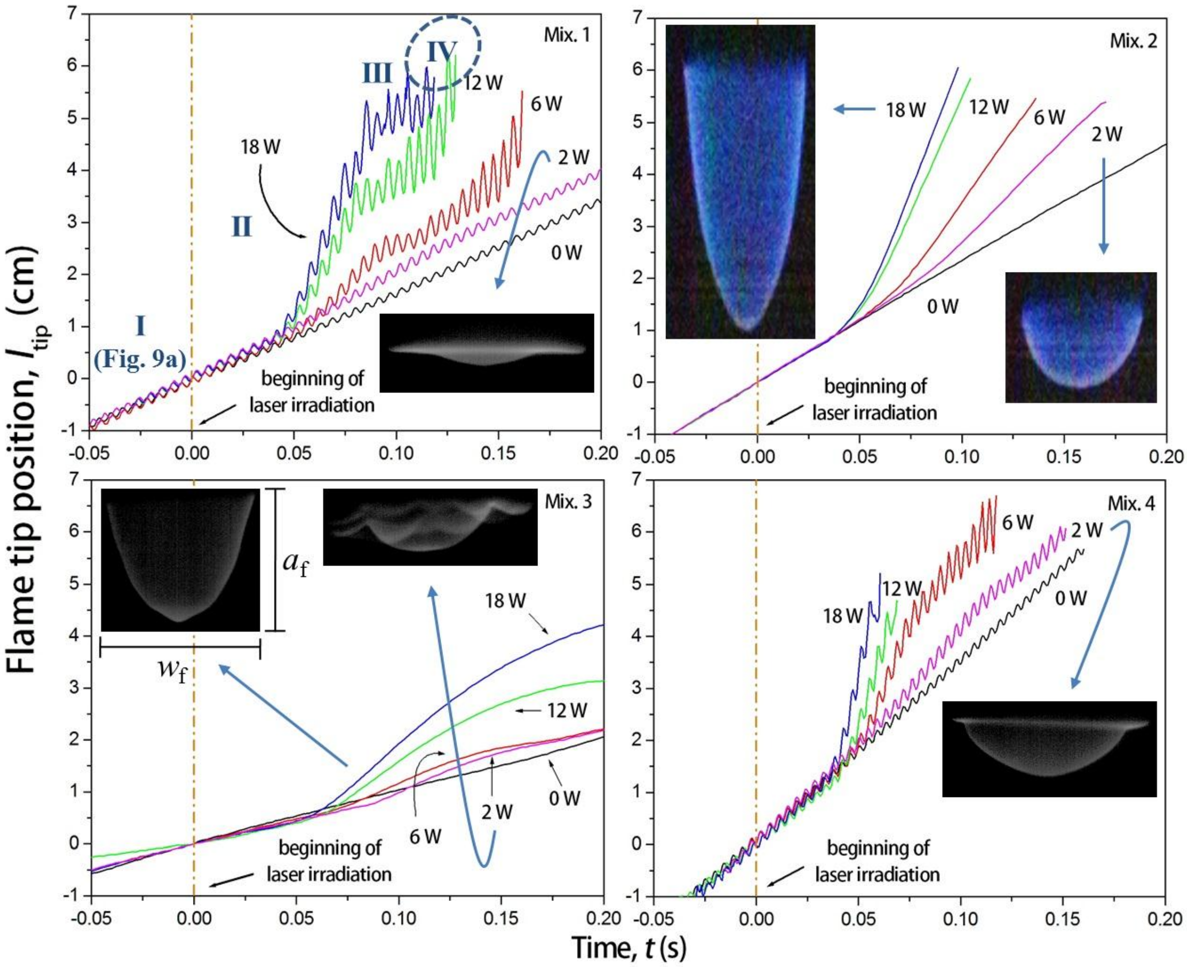

Fig. 3.7 Temporal flame tip position with various laser power inputs with flame propagating downward in Mix. 1, 2, 3, and 4; Individual regions of I, II, III, and IV in Mix. 1 correspond to flame behaviors in Fig. 3.8a, respectively.

flame surface area should be sufficiently larger than the radius-to-length ratio of the combustion tube related to acoustic radiative losses:

$$ak \geq r/L. \tag{3-1}$$

However, the experimental results show that a sufficiently increased flame surface area due to laser irradiation does not support the generation of acoustic sound, as shown in Mix. 2 and 3 in Fig. 3.7. The maximum values of ak are 7.51 and 2.70 ($r/L \approx 0.05$), and the maximum displacement flame velocities, S_d, are 101.7 and 184.1 cm/s in Mix. 2 and 3 with laser powers of 18 W, respectively. Here, a and k are calculated by $a = a_f$ and $k = \pi/w_f$, where a_f and w_f are the maximum amplitude and maximum width of curved flame, respectively, as shown in the inserted pictures in Fig. 3.7.

In fact, these values are too large compared to Pelcé and Rochwerger's analysis [30] which is limited to small amplitude. Therefore, to consider effects of small amplitude on the generation of acoustic sound is also needed. As shown in Mix. 2 and 3 with laser powers of 2 W in Fig. 3.7, the small flame amplitudes also do not cause the generation of acoustic vibration and, here, the maximum values of ak are 1.95 and 1.45, respectively.

As shown in Fig. 3.7, Mix. 1 and 4 are regimes of the primary acoustic instability even without laser irradiation. In these cases, the initial conditions are vibrating flat flames prior to the appearance of laser irradiation in the areas to the left of the dashed-dotted lines in Fig. 3.7. Now Mixture 1 is considered. Figure 3.8a shows flame behaviors of transition from an initially flat flame to turbulent motion induced by a laser power of 18 W in Mix. 1. The numerical values at the bottom of each picture are the passage of time after laser irradiation. One can divide the results into four individual types of flame behavior in order to describe the transition process in detail. First, the flat flame appears corresponding to the primary acoustic instability, as shown in Fig. 3.8a (I). The ice-cream flame is observed after exposure to CO_2 laser light in Fig. 3.8a (II). In this region, the sudden acceleration of the flame tip position with increasing oscillation amplitude during 50-80 ms can be observed as shown in Fig. 3.7. Also, the flame tip maintains convex shape during propagation with ice-cream structure as shown in Fig. 3.8b (II). After this, the flame exhibits a corrugated structure corresponding to the secondary acoustic instability in Fig. 3.8a (III). Once a concave structure appears at the flame tip, as shown in Fig. 3.8c (II-III), the corrugated wave propagates from the center to the outer edge of the flame as time goes by, as reported in the previous work [38, 39]. Moreover,

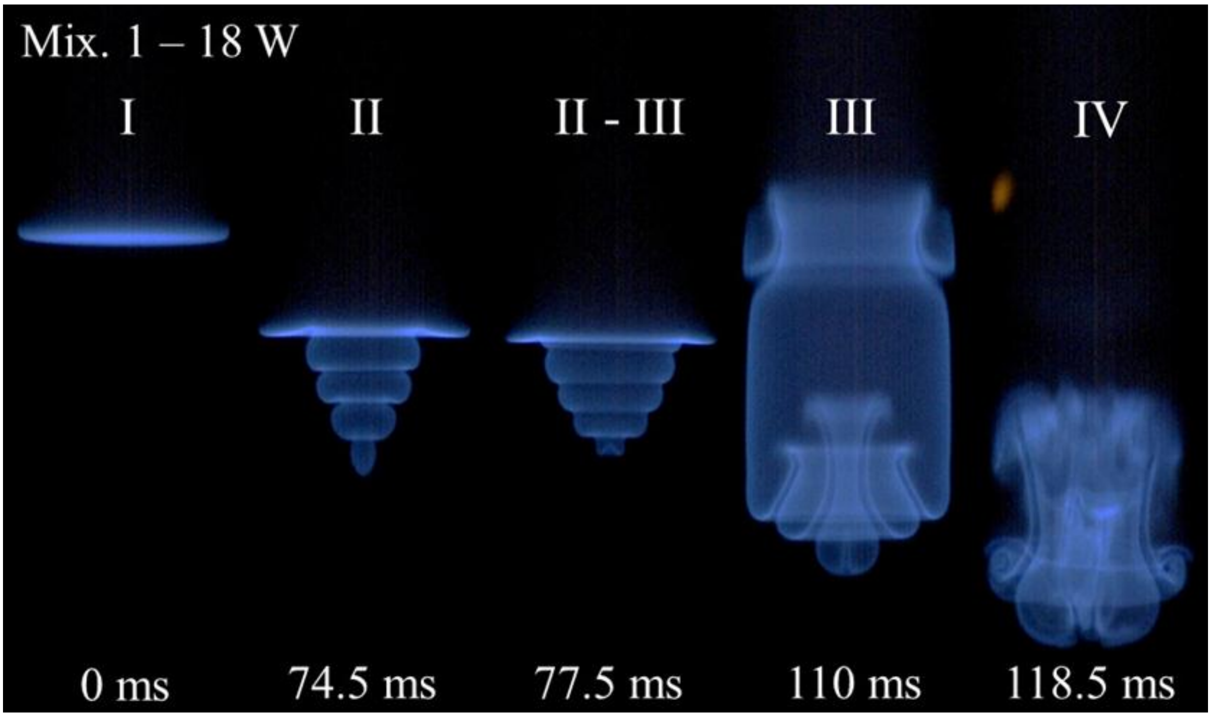

(a)

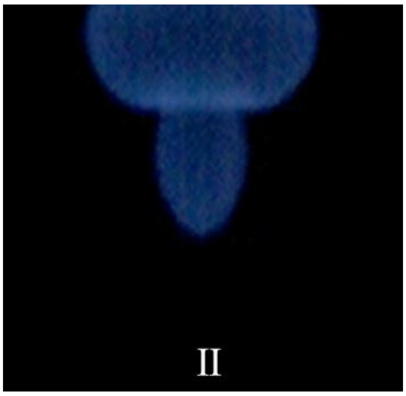

(b)

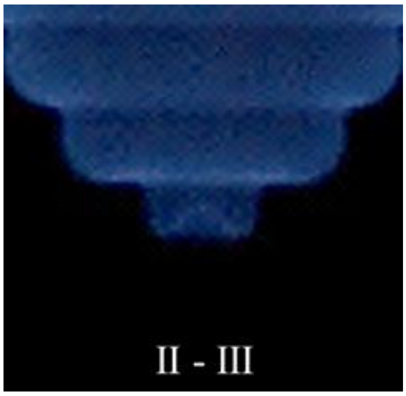

(c)

Fig. 3.8 (a) Distinctive flame behaviors of transition with laser power of 18 W in Mix. 1, (b) enlarged image at flame tip in II, and (c) enlarged image at flame tip in II III; (I) flat flame, (II) ice-cream flame, (III) corrugated structure, and (IV) turbulent motion connecting with Mix. 1 in Fig. 3.7.

the slope of flame tip position suddenly decreases, as shown in Fig. 3.7. Finally, explosive turbulent motion appears with a breakdown of the curved structures in Fig. 3.8a (IV). In Mix. 1 with laser irradiation, the flames undergo the whole transition process as described above except for a laser power of 2 W. This case will be discussed later in this Section.

To assess the effects of variations of flame areas on the growth rate of the acoustic instability, the estimation of pressure variation has been conducted. Figure 3.9 shows the measured acoustic pressure fluctuation at the bottom of the tube as a function of time with a laser power of 18 W in Mix. 1. Vertical dotted lines denote the boundaries of individual regions of transition processes from flat flames to turbulent motion. The start of laser

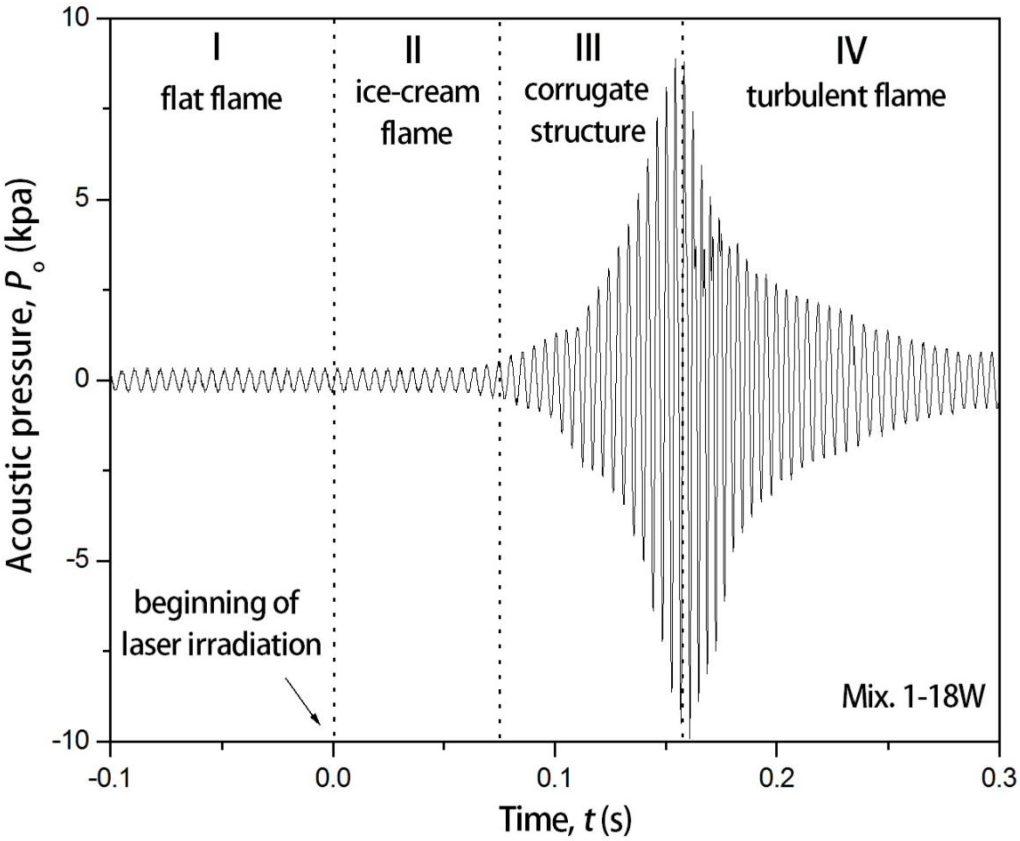

Fig. 3.9 Acoustic pressure at the bottom of the tube as a function of time with a laser power of 18 W in Mix. 1.

irradiation is defined as t = 0.0 s. No growth of pressure amplitude is observed until the corrugated structure appears, as shown in Fig. 3.9. Once the corrugated structure via ice-cream flame appears as shown in Fig. 3.8a (III), the acoustic pressure exponentially increases. This is a typical feature of the secondary acoustic instability [25, 33]; as more laser irradiation time elapses, turbulent motion appears with a breakdown of the coherent corrugated structures, and the acoustic pressure simultaneously decreases. An unexpected characteristic is the limited change in the pressure amplitude in the region of the ice-cream flame (II), even with a sudden change in the flame surface area. This phenomenon gives important information that the variation in the flame surface area is not always associated with pressure amplification. For further understanding, qualitative comparisons are given in Fig. 3.10. Figure 3.10a and b shows acoustic pressure in front of the flames and flame surface areas as a function of time (a) without laser irradiation and (b) with continuous laser irradiation at 18 W before the corrugated structure appears in Mix. 1. The solid and dotted lines denote pressure change, P_u, and flame surface area change, A_f, respectively. Fluctuations of pressure and flame surface area are in phase at frequencies of 183 and 182 Hz in (a) and (b), respectively. The most important observation is that the acoustic pressure amplitudes are virtually the same, even though the flame surface area changes as compared with (a) and (b). Here, the maximum flame surface areas are 21.8 and 42.7 cm^2 without and with laser irradiation in Mix. 1, respectively. In particular, for the case of laser irradiation, the maximum value of $(ak)^2$ is 12.3.

To discuss the effects of flame surface area on pressure amplification more clearly, an additional experiment on short-term laser irradiation is also conducted. According to previous research [39], the threshold of the secondary acoustic instability is given in terms of laser irradiation time and power. A case, in which there is no transition to turbulent flame namely

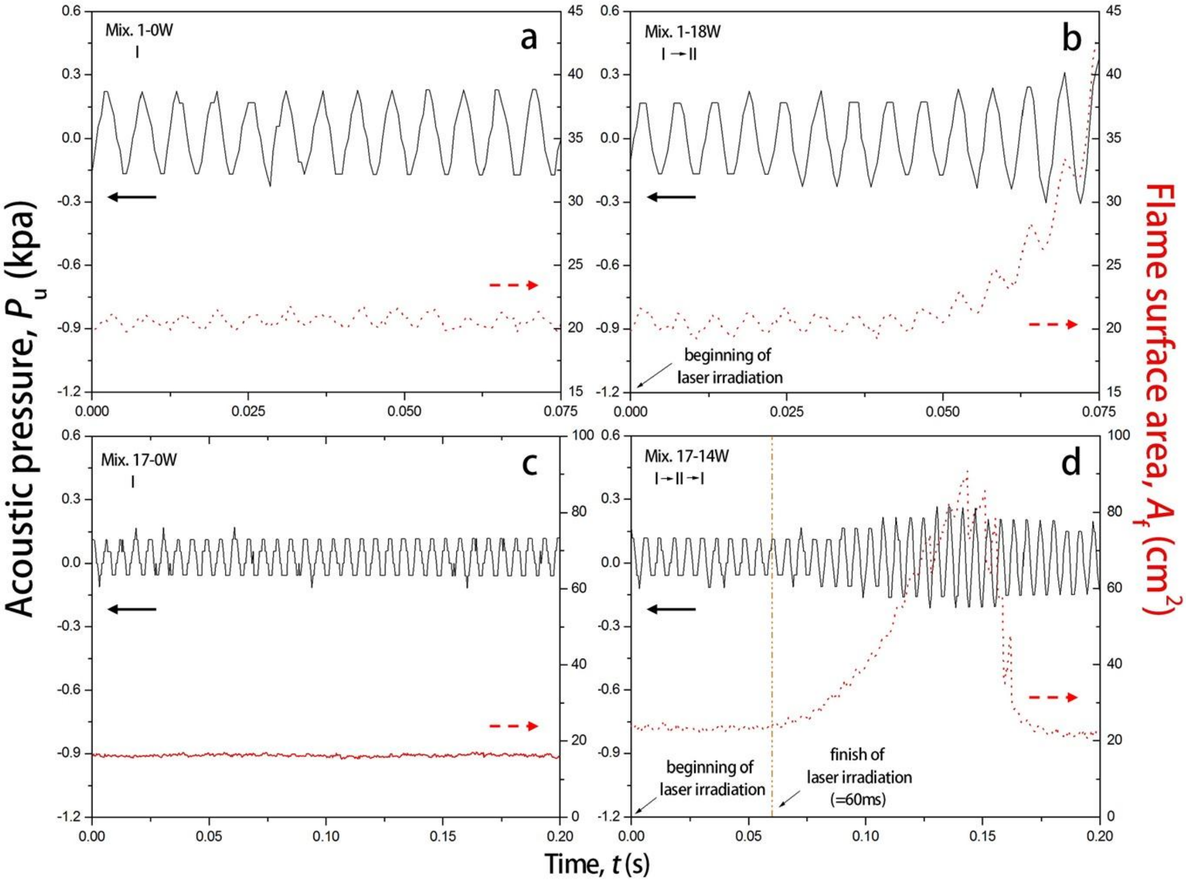

Fig. 3.10 Acoustic pressure in front of the flames and flame surface area as functions of time (a) without laser irradiation and (b) with continuous laser irradiation at 18 W in Mix. 1; and (c) without laser irradiation and (d) with a short-term laser irradiation over 60 ms at 14 W in Mix. 17.

the laser condition of 60 ms, is selected at 14 W for rich ethylene flame diluted with CO_2 gas [39]. Figure 3.10c and d show acoustic pressures in front of the flames and flame surface areas as functions of time (c) without laser irradiation and (d) with short-term laser irradiation in Mix. 17. In Fig. 3.10d, the start time of laser irradiation is defined as t = 0.0 ms, and the vertical dashed-dotted line denotes the end of laser irradiation (t = 60 ms). The deformation of the flame front starts at around 50 ms corresponding to an ice-cream flame. The peak flame area appears at around 140 ms. In the images captured by a high-speed camera, the flame tip curvature starts to decrease at around 100 ms, and finally, the flat flame is formed again. Fluctuations of pressures and flame surface areas are also in phase, and their frequencies are 168 Hz in (c) and (d). In the case of short-term laser irradiation, the acoustic pressure amplitude slightly changes with extreme variation in the flame surface area. Nevertheless, it can be ignored considering the order of magnitude of pressure amplification in the secondary acoustic instability, as shown in Fig. 3.9. Here, the maximum flame surface areas are 17.0 and 90.8 cm^2 without and with a short-term laser irradiation in Mix. 17, respectively. In particular, for the case of a short-term laser irradiation, the maximum value of $(ak)^2$ is 9.9. Here, the same results as the cases of continuous laser irradiation are obtained, that is, the acoustic frequency and the growth rate of acoustic instability are not always associated with the increase or decrease in the flame surface area.

As mentioned above, it is necessary to consider the effects of small amplitude as shown in Mix. 1 with laser power of 2 W in Fig. 3.7. The initial vibrating flat flame still maintains acoustic sound even for laser irradiation with weak laser power. Figure 3.11 show the measured acoustic pressure fluctuation at the bottom of the tube as a function of time in this case. The flame shape changes to weakly curved flame not ice-cream flame after exposure to CO_2 laser light as the inserted pictures. Then, the weakly curved flame again becomes the flat shape at around 0.2 s even under continuously irradiating CO_2 laser light. Because the flame propagation enhancement by the laser irradiation is too weak and the acoustic wave suppress the weakly convex structure. Thereby, the concave structure which indicates initiator of the secondary acoustic instability cannot be observed. Here, the pressure amplitude is the limited change despite the change of flame shape. Therefore, the variation in the flame surface area even with small amplitude does not always support the growth of acoustic pressure. In this case, the maximum value of $(ak)^2$ is 0.29.

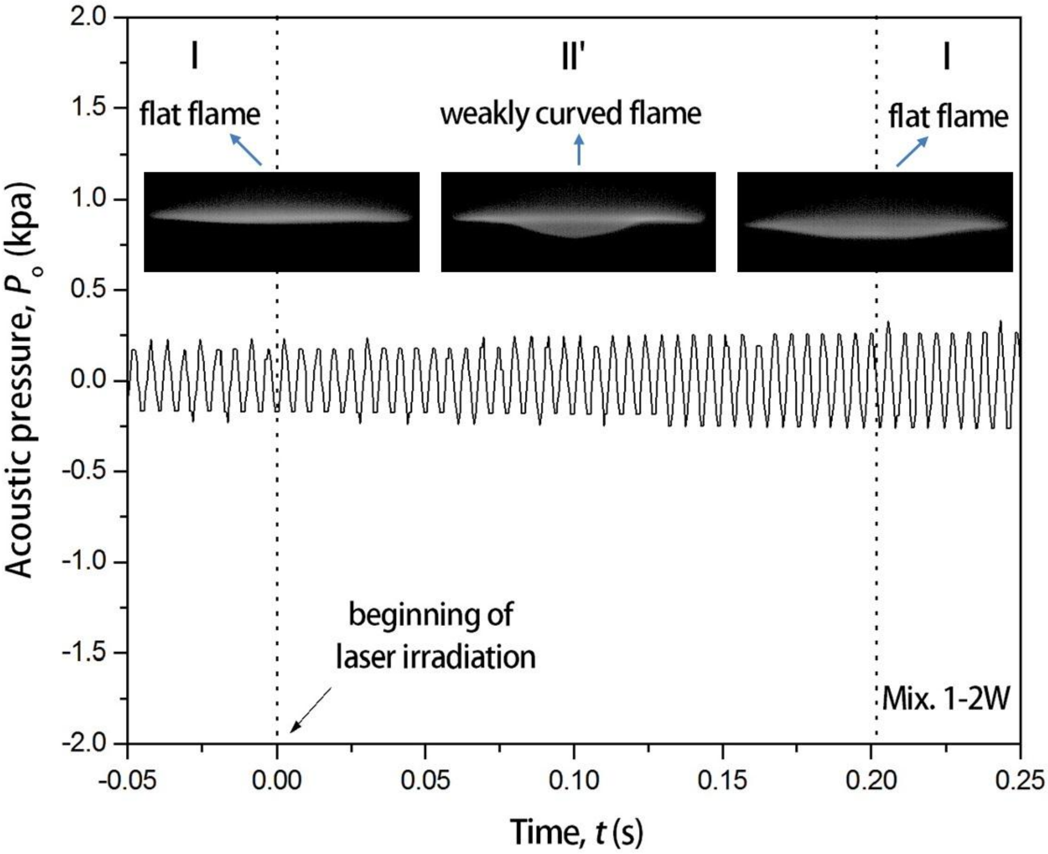

Fig. 3.11 Acoustic pressure at the bottom of the tube as a function of time with a laser power of 2 W in Mix. 1; (I) flat flame and (II') weakly curved flame.

Meanwhile, Figure 3.11 is in the region of saturated acoustic pressure after the vibrating flat flame takes place. On the other hand, the calculation range of Pelcé and Rochwerger's analysis [30] is the region of developing acoustic pressure before the flame has achieved transition to the flat front. Therefore, the data in Fig. 3.11 and ref [30] could not be compared each other. However, the experimental cases of Mix. 2 and 3 (relatively slow flames) with and without laser irradiation are in the region of developing acoustic pressure comparable with Pelcé and Rochwerger's calculation range [30]. In the cases, the variations of flame surface area did not induce primary acoustic instability within the tested laser power condition as seen in Fig. 3.7 (no fluctuation of flame tip position is observed in Fig. 3.7 in

Mix. 2 and 3).

In this section, to confirm the mechanism of acceleration coupling, various experiments with different flame surface areas induced by laser irradiation are conducted. The change in the flame area does not cause the spontaneous generation of the primary acoustic instability in initially nonvibrating flames. Furthermore, the variations of flame surface areas (growth or decline) do not support change in the acoustic frequency and growth rate of the acoustic pressure, even for initially vibrating flat flames.

3.3 Concluding remarks

This Chapter 3 provides experimental evidence on the onset of the primary acoustic instability of downward-propagating flames in a tube. The main focus was to establish the dominant onset mechanism of primary acoustic instability between pressure coupling and acceleration coupling. The adiabatic flame temperature and the laminar burning velocity correlated well with the average acoustic intensity. Based on these results, linear relationships between the coupling constant and the average acoustic intensity were obtained, and the critical values of the coupling constants (βM_{CO2} = 0.0082, βM_{N2} = 0.0099) were acquired through linear approximation of the onset of the primary acoustic instability for lean ethylene flames. Thus, the average acoustic intensity is proportional to the coupling constant, βM, on the primary acoustic instability in present experimental observations.

To ensure the relevance of the mechanism of acceleration coupling in the primary acoustic instability, additional experiments with CO_2 laser irradiation are conducted. Contrary to the expectations based on previous research, the experimental results showed that growth of the flame area did not cause the spontaneous generation of the primary acoustic instability in initially nonvibrating flames. Even with initially vibrating flat flames, the growth of acoustic pressure could not be observed, even with a dramatic increase or decrease of the flame surface area by CO_2 laser light irradiation. Therefore, it is concluded that variation in the flame surface area does not always function as the coupling mechanism of the primary acoustic instability.

Finally, the effects of acoustic losses on acoustic instability are also estimated. Larger total acoustic losses as functions of speed of sound, kinematic viscosity, and thermal diffusivity tended to suppress the acoustic vibration even at the same coupling constant.

Chapter 4: Estimation of effects of Lewis number on primary acoustic instability

To estimate effects of Lewis number on the primary acoustic instability in Chapter 4, the premix gas composed of ethylene, oxygen, carbon dioxide, and nitrogen is placed under atmospheric pressure in the tube. Various gas compositions are tested in association with different laminar burning velocities (S_L), adiabatic flame temperatures (T_b), acoustic losses ($1/\tau_{loss}$), coupling constant values (βM), and *Le* (Table 4.1). The mixtures provide information for *Le* below unity from Mix. 1–4, very close to unity from Mix. 5–10, and above unity from Mix. 11–14.

Table. 4.1 Summary of results for the tested gas in Chapter 4.

Mix.	C_2H_4	O_2	CO_2	N_2	S_L (cm/s)	T_b (K)	$1/\tau_{loss}$ (s^{-1})	βM	*Le*	vibration or not
1	0.09	0.19	0.73		6	1670	8.4	0.0035	0.79	X
2	0.09	0.20	0.71		12	1817	8.3	0.0040		O
3	0.09	0.21	0.70		16	1917	8.4	0.0066		O
4	0.086	0.213	0.701		18	1982	8.5	0.0074		O
5	0.06	0.20	0.74		11	1814	8.4	0.0049	1.05	X
6	0.07	0.22	0.71		16	1951	8.4	0.0078		O
7	0.07	0.23	0.70		19	2000	8.5	0.0093		O
8	0.07	0.24	0.69		22	2049	8.5	0.0110		O
9	0.07	0.26	0.67		25	2049	8.6	0.0116		O
10	0.07	0.29	0.64		29	2049	8.7	0.0126		O
11	0.04	0.14		0.82	22	1832	12.7	0.0070	1.34	X
12	0.05	0.16		0.79	32	2000	12.6	0.0103		O
13	0.05	0.18		0.77	40	2092	12.6	0.0131		O
14	0.05	0.19		0.76	43	2103	12.6	0.0138		O

4.1 Equidiffusive flame

First, the combustion behavior in the acoustic field is observed for equidiffusive flames (*Le* = 1). Dynamic flame behavior for freely propagating flames is considered. Figure 4.1 depicts the temporal variability in the flame tip’s position l_{tip} and the flame behavior (inserted pictures) for *Le* ≈ 1 at the view area. When the flames reach the view area, *t* = 0.0 s. Three distinct types of behavior are identified: 1) a regime of non-acoustic instability, where the cellular flame propagates without fluctuation (Mix. 5); 2) a regime of acoustic instability, where the flame fronts are still cellular but vibrating (Mix. 6 and 7); and 3) a regime of acoustic instability, where the vibrating flat flames propagate (Mix. 8, 9, and 10). Here, the vibrating flame is defined as the flame with a peak-to-peak amplitude periodic oscillation over 0.03 cm. Comparing Mix. 5 and 6, the flame of Mix. 6, with larger βM than that of the flame of Mix. 5, displays vibration even with the same acoustic losses. In both cases, the cellular structure can be observed even at *Le* ≈ 1, which may result from the presence of heat losses to the wall. According to Jackson and Kapila's study [46], the critical *Le* causing the cellular instability increases with excessive heat losses near the flammability limit. When βM increases, the flame assumes a flat shape and vibrates periodically, as shown in Mix 8. The amplitude of the flame vibration and the acoustic pressure fluctuation increase with βM.

Figure 4.2 shows typical transition behavior from an initial cellular front to a flat flame after ignition in primary acoustic instability (Mix. 8). The numerical values at the bottom of each picture indicate time. The transition proceeds as follows. After ignition, the cellular flame front propagates downward, because of diffusive thermal instability. Then, the flame becomes flat under the presence of acoustic sound resonating at a quarter of the wavelength and remains flat through the close end of the tube. Figure 4.3 shows the measured acoustic pressure fluctuation at the bottom of the tube as a function of time in Mix. 8. Two different

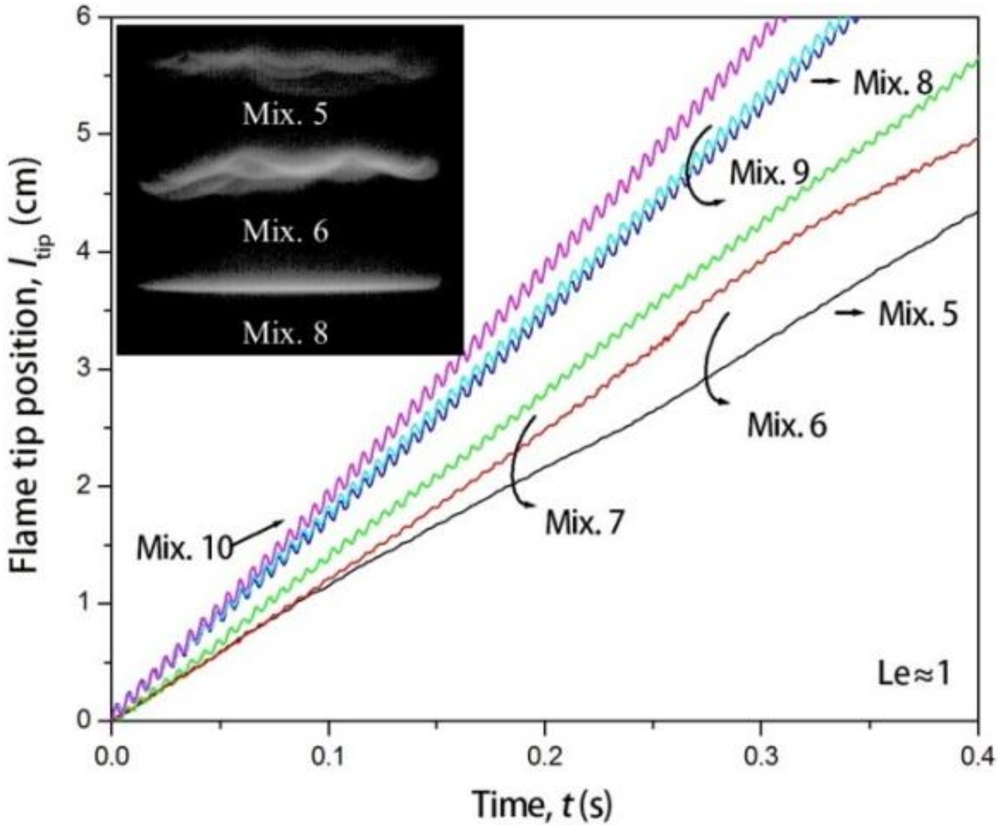

Fig. 4.1 The flame tip's position at $Le \approx 1$ over time.

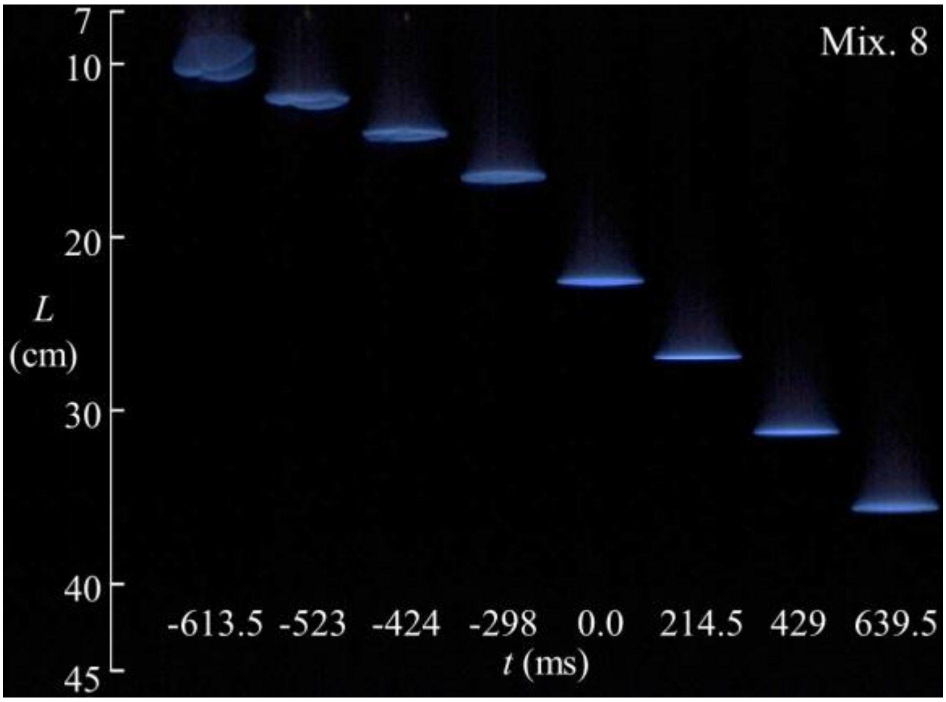

Fig. 4.2 Sequential images of a propagating flame in Mix. 8.

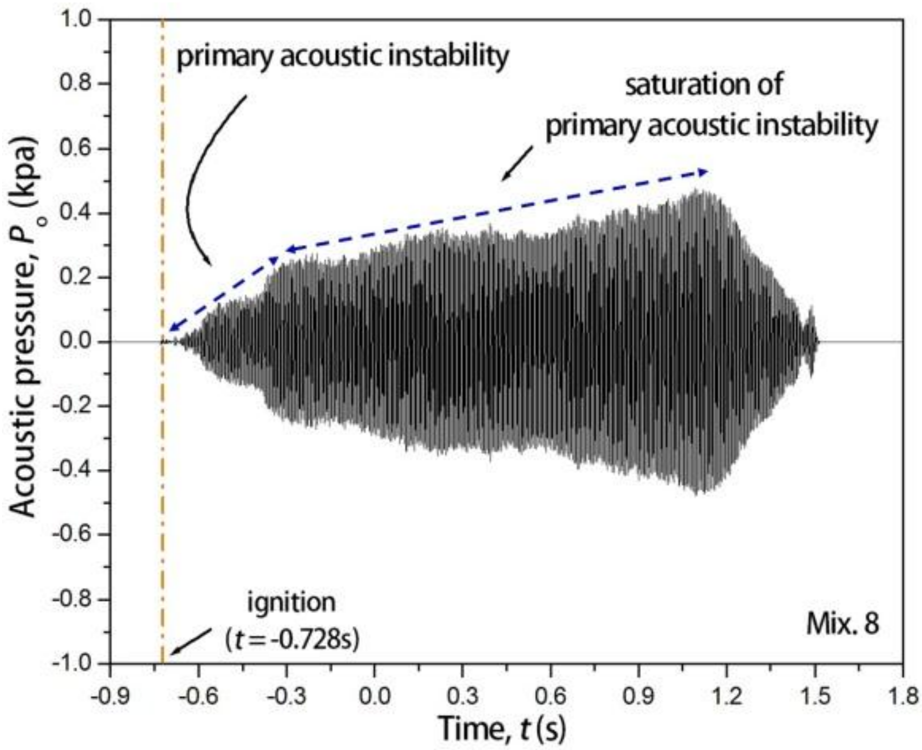

Fig. 4.3 Acoustic pressure at the bottom of the tube as a function of time in Mix. 8.

stages are observed. The first stage (indicated as primary acoustic instability in Fig. 4.3) corresponds to the region of developing acoustic pressure, which occurs when the vibrating flat flame via the cellular structure appears as shown in Fig. 4.2. The linear growth rate is approximately 2.4 s^{-1}. The next stage corresponds to the region of saturated acoustic pressure, which occurs after the flame has achieved transition to the flat front. The growth rate of acoustic pressure (≈ 0.7 s^{-1}) in the saturation region becomes much smaller than that in the primary developing region, as shown in Fig. 4.3.

Summarizing the above experimental observations, three facts can be pointed out: (1) a larger coupling constant tends to generate a larger amplitude of flame vibration and acoustic pressure under the same acoustic losses, (2) the strong primary acoustic sound suppresses the initial cellular structure, and (3) in the time-dependent acoustic pressure, the growth rate of saturated acoustic pressure becomes much smaller than that in the primary developing region.

4.2 Nonequidiffusive flame

4.2.1 Low Lewis number

For non-equidiffusive flames, theoretical results showed that the chemical reaction rate becomes more sensitive to variations in gas temperature with decreasing *Le* [40, 41]. This is because the reaction zone δ_f, which is given by $\delta_f \approx \sqrt{\alpha\tau_t}$, where α is thermal diffusivity and τ_t is transit time, becomes thinner with decreasing *Le*. Therefore, for diffusive thermal effects in the acoustic field, significant acoustic sound amplification is anticipated.

Figure 4.4 shows temporal variations in the flame tip's position for $Le < 1$. Three distinct types of behavior are identified, as observed for $Le \approx 1$. Mixture 1 corresponds to the regime of non-acoustic instability with cellular structure, Mix. 2 corresponds to the regime of acoustic instability with vibrating cellular flame, and Mixt. 3 and 4 to the regime of acoustic instability with vibrating flat flames. Particularly, for Mix. 1, the short wavelength

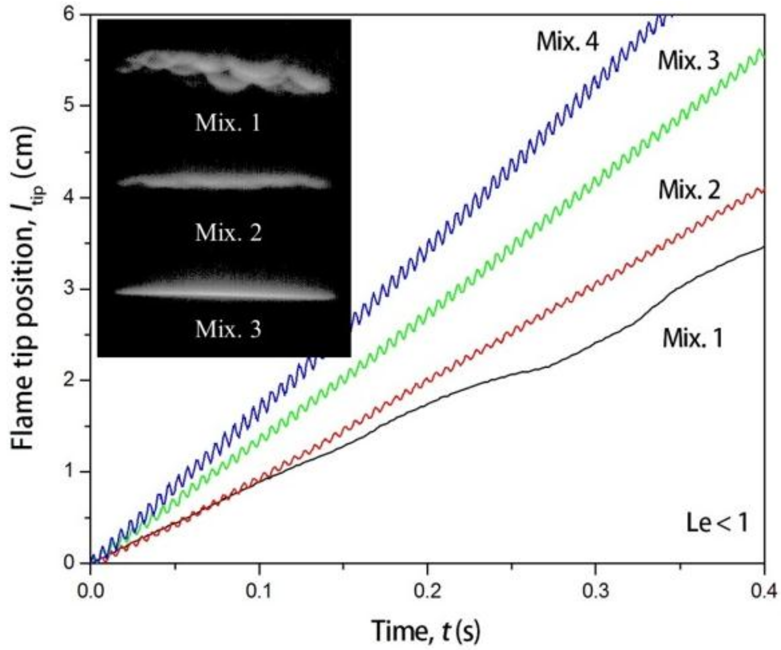

Fig. 4.4. Temporal flame tip's position at $Le < 1$.

disturbance (cellular structure) is observed more clearly than that in Mix. 5 (see, Fig. 4.1), probably due to the low *Le* value, since the growth rate of the short wavelength disturbance is a function of $\frac{1}{2}\beta(1-Le)$ [16]. Considering the effect of the coupling constant, a larger βM tends to generate larger acoustic vibration amplitude, as was also the case for $Le \approx 1$. One of the most noticeable differences with $Le \approx 1$ is that the vibrating flames, when $Le < 1$, appear at lower βM values under the same acoustic losses. Here, the acoustic sound generated in Mix. 2 with $\beta M = 0.0040$, however, is not observed in Mix. 5, even with the similar $\beta M = 0.0049$. This may be attributed to the higher sensitivity of the reaction zone to variations in gas temperature when $Le < 1$. In general, the reaction zone is expressed as $\delta_f = (RT_b/E)\delta_{th}$ and depends on temperature [16]. Here, R is the gas constant, E is the activation energy, and δ_{th} is the thermal thickness. The bracket is inversely related to the Zel'dovich number, which is $\beta = E(T_b - T_u)/(RT_b^2)$. Therfore, a larger β results in a thinner reaction zone; thus, β is an important parameter in changing primary acoustic instability. Similar to β, a decreased *Le* results in a thinner reaction zone; thus, a low *Le* tends to enhance primary acoustic instability.

To estimate the effects of flame shape variations on primary acoustic instability, experiments induced by CO_2 laser irradiation are conducted. Figure 4.5 shows the temporal change of the flame tip's position for 6 and 3 W laser power, in Mixt. 1 and 2, respectively. Figure 4.6 shows the measured acoustic pressure fluctuation at the bottom of the tube as a function of time with laser irradiation in Mix. 2. In Figs. 4.5 and 4.6, the vertical dashed-dotted lines indicate the beginning of laser irradiation. As discussed above, Mix. 1 and 2 correspond to regimes of non-acoustic and acoustic instabilities without laser irradiation, respectively. In Mix. 1, a sudden increase in the propagation speed starts around 0.1 s after the beginning of laser irradiation in Fig. 4.5. However, the flame exhibits no vibration and propagates with a smoothly curved front (bottom of the inserted images in Fig. 4.5) even under continuously

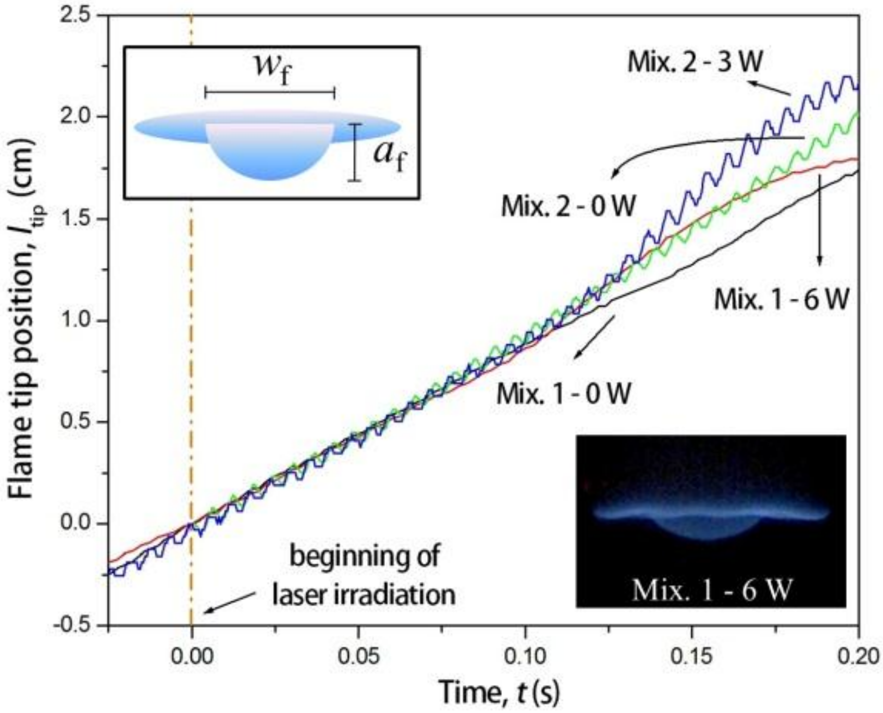

Fig. 4.5 Temporal flame tip's position with laser powers in Mix. 1 and 2 (*Le* = 0.79).

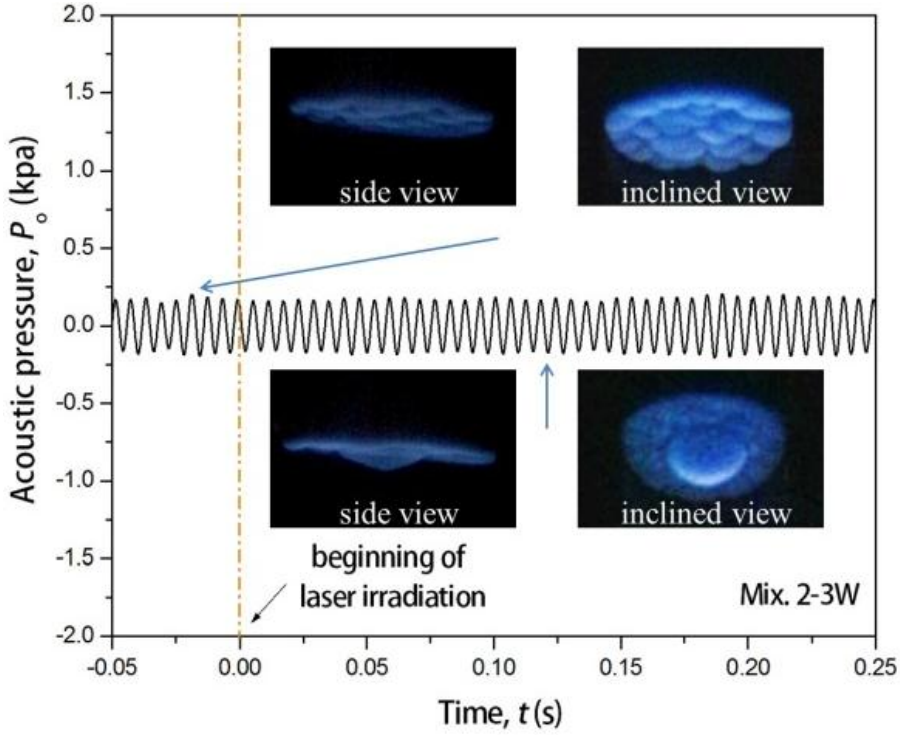

Fig. 4.6. Acoustic pressure at the bottom of the tube as a function of time for 3 W laser power in Mix. 2 (*Le* = 0.79).

irradiating CO_2 laser light.

Pelcé and Rochwerger [30] introduced a criterion for thermoacoustic instability, according to which the flame surface area should be sufficiently larger than the radius-to-length ratio of the combustion tube related to the acoustic losses: $ak \geq r/L$, where r is the tube radius and L is the length of the tube. However, the experimental results show that the weakly increased flame surface area, due to laser irradiation, does not support the generation of acoustic vibration (Fig. 4.5). The maximum value of ak is 1.09 ($r/L \approx 0.05$). Here, a and k are calculated by $a = a_f$ and $k = \pi/w_f$, where a_f and w_f are the maximum amplitude and width of the curved flame, respectively (upper inserted images in Fig. 4.5).

Mixture 2 corresponds to a regime of primary acoustic instability even without laser irradiation (Fig. 4.5). Around 0.1 s after the beginning of laser irradiation, the sudden acceleration of the flame tip's position with increasing flame displacement-oscillation amplitude is observed. The inserted images in Fig. 4.6 show flame behaviors before (upper) and after (bottom) laser irradiation. The initial cellular structure (short wavelength disturbance) changes to the smoothly curved front related with long wavelength disturbance by laser irradiation (inclined views in Fig. 4.6). However, an unexpected characteristic is the limited change in the pressure amplitude, even with variation in the wavelength and amplitude of the disturbance. This phenomenon indicates that the wavelength of the flame front's shape does not affect the primary acoustic sound in the present experiments. Here, the maximum value of $(ak)^2$ is 1.25.

4.2.2 Large Lewis number

For $Le > 1$, three distinct types of behavior can be observed similar to $Le \approx 1$ (Fig. 4.7). Mixture 11 corresponds to the regime of non-acoustic instability with a smoothly curved front,

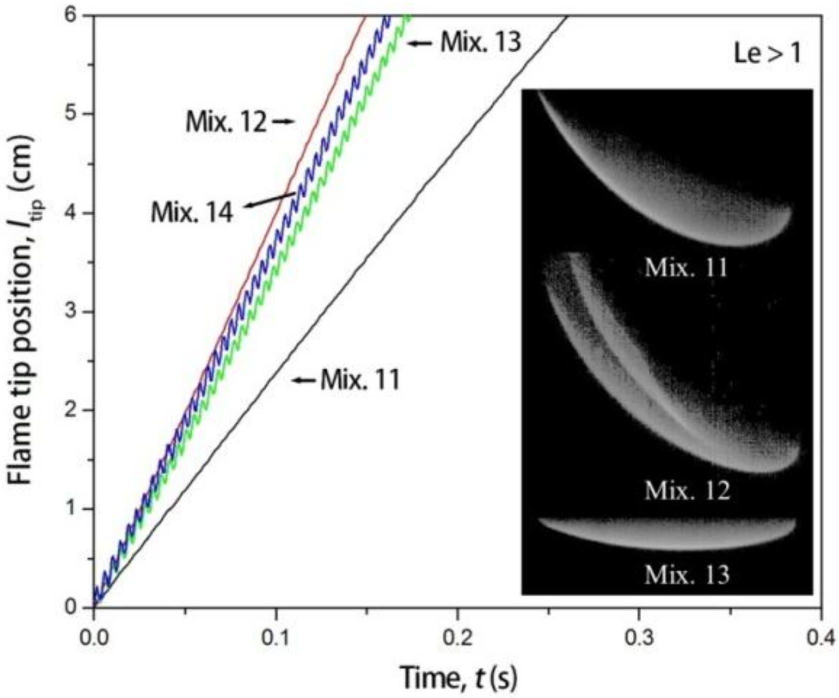

Fig. 4.7. Temporal flame tip's position at Le > 1.

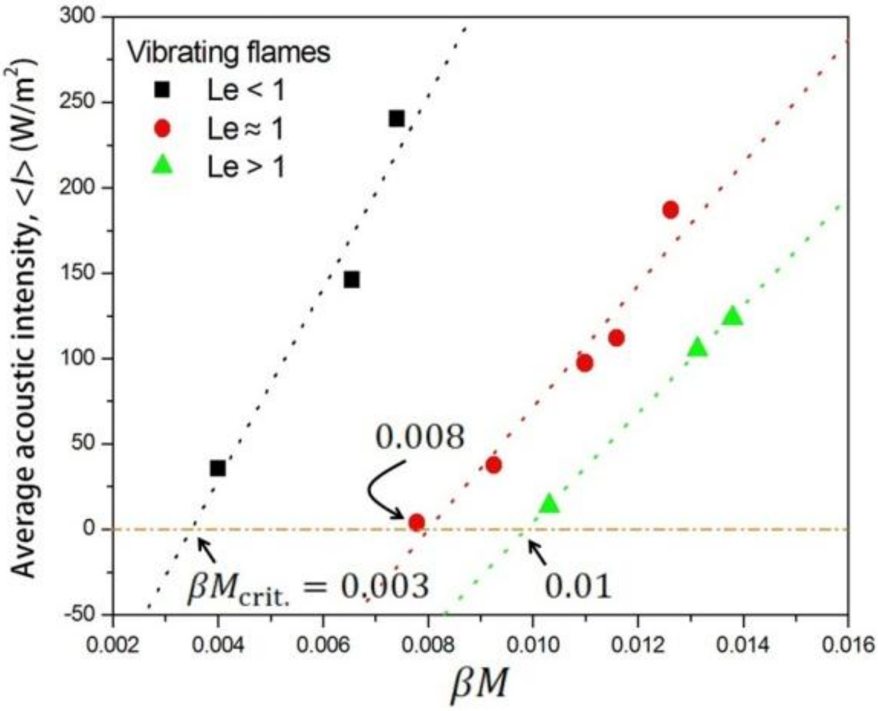

Fig. 4.8. Dependence of the average acoustic intensity for primary acoustic instability on the coupling constant at different Lewis numbers.

Mix. 12 to the regime of acoustic instability with a vibrating smoothly curved flame, and Mix. 13 and 14 to the regime of acoustic instability with vibrating flat flames. Comparing Mix. 11 with Mix. 5 (Fig. 4.1) at $Le \approx 1$, both are non-vibrating flames without any acoustic sound; however, a relatively longer wavelength disturbance occurs in Mix. 11, which may result from D–L instability. The vibrating flames appear, when $Le > 1$, at relatively larger βM than $Le \approx 1$. Here, the acoustic sound is not observed in Mix. 11 with $\beta M = 0.007$, although it is generated in Mix. 6 even with the similar $\beta M = 0.0078$. This may result from the larger acoustic losses and which the reaction zone is relatively insensitive to variations in gas temperature due to the greater flame thickness. When the coupling constant further increases, the transition from the smoothly curved front to the flat flame occurs with strong acoustic sound even in $Le > 1$. The restabilization of D–L caused by primary acoustic instability was discussed by Searby [25]; the qualitative results therein agree with the present experimental observations. Unfortunately, the pulsating instability cannot be observed in here, as the theoretical prediction of Clavin et al. [28] suggested.

Overall, three facts can be pointed out regarding non-equidiffusive flames: (1) for $Le < 1$, acoustic sound is generated at relatively low βM, because the reaction rate is more sensitive to variations in gas temperature, (2) the wavelength of the flame's shape exhibits a limited effect on the amplification of the primary acoustic sound, and (3) for $Le > 1$, a relatively larger βM is required to observe the primary acoustic instability, because the reaction rate is more insensitive to gas temperature variations, and the strong primary acoustic sound suppresses D–L instability.

Based on the presented experimental evidence, the average acoustic intensity is assigned as the coupling constant for different values of Le in Fig. 4.8. The calculation of the average acoustic intensity $\langle I \rangle$ is described in Appendix B. The average acoustic intensity correlates well with βM. Considering a constant Le, a larger βM tends to generate strong acoustic sound. To determine the critical βM for the generation of primary acoustic instability, a linear approximation is established, and the values 0.003, 0.008, and 0.01 are obtained depending on Le. These differences may be caused by diffusive thermal effects and acoustic losses. Therefore, a relatively high βM is required to generate primary acoustic instability as Le increases.

4.3 Concluding remarks

This Chapter 4 deals with the effects of the Lewis number on primary acoustic instability of downward-propagating flames in a combustion tube. The different coupling mechanisms are investigated, including the direct sensitivity of the reaction rate to acoustic pressure and variation in the flame surface area induced by acoustic acceleration. A larger coupling constant βM tends to generate larger amplitude of flame vibration under the same acoustic losses and the strong primary acoustic sound stabilizes intrinsic flame instability regardless of the disturbance wavelength.

Considering non-equidiffusive flames, the acoustic sound is generated at relatively low βM when Le decreases, because the reaction rate is more sensitive to the variations in gas temperature with decreasing Le. For $Le > 1$, relatively larger βM is required to observe primary acoustic instability because the reaction rate is relatively more insensitive. Based on these results, a linear relationship between βM and the average acoustic intensity was obtained under a constant Le, and the critical values of the coupling constants ($\beta M_{Le\approx0.79}$ = 0.003, $\beta M_{Le\approx1.05}$ = 0.008, $\beta M_{Le\approx1.34}$ = 0.01) were acquired through linear approximation depending on different values of Le. These differences may be attributed to diffusive thermal effects and acoustic losses. However, the change in the flame front's shape by laser irradiation has limited effect on the generation of primary acoustic instability under any tested Le conditions.

Chapter 5: Estimation of effects of various fuels on acoustic instability

To estimate effects of various fuels on the primary acoustic instability in Chapter 5, different types of gas compositions for CH_4, C_2H_4 and C_3H_8 diluted with N_2 or CO_2 are used. For acoustic instability, a coupling constant, βM, plays a central role in the initiation mechanism. It is responsible for variation of local heat release rate due to an incoming acoustic wave according to the results from Chapter 3. Effects of Lewis number on acoustic instability in nonequidiffusive flames, in which diffusive-thermal effects are dominant in internal flame structure, were described. For Lewis number below (above) unity, the initiation of acoustic instability occurs at relatively small (large) coupling constant because the chemical reaction rate becomes sensitive (insensitive) to gas temperature fluctuation in acoustic field according to the results from Chapter 4. Therefore, in this Chapter, the experimental study of downward-propagating flames is performed with different fuels for CH_4, C_2H_4 and C_3H_8 diluted with N_2 or CO_2 in a tube regarding the dependence of effects of fuel on generation mechanisms of primary as well as secondary acoustic instabilities followed by previous Chapter 3 and 4.

The propagation tube is 50-mm inner diameter and 711-mm length which is longer tube with previous one in Chapter 3 and 4 (511-mm length). the premix gas composed of methane, ethylene, propane, oxygen, carbon dioxide, and nitrogen are set at atmospheric pressure in the tube. Equivalence ratios as 0.8 and 1.2 were selected to change Le. To estimate different laminar burning velocities with the fixed equivalence ratio, dilution ratio, $D = \frac{O_2}{O_2+N_2\ or\ CO_2}$, is changed. The flame properties (e.g., laminar burning velocities (S_L), speed of sound (c), and adiabatic flame temperatures (T_b)) are calculated using CHEMKIN (Premix code/ USC II)

[43].

5.1 Flame stability

The experiments with downward-propagating flames were performed by varying laminar burning velocity, S_L, and two different equivalence ratios as 0.8 and 1.2. Figure 5.1 shows flame stability maps as functions of S_L and Φ with (a) CH_4, (b) C_2H_4 and (c) C_3H_8 diluted with N_2 or CO_2. Six distinct types of flame behavior are identified.

I : Curved flame without acoustic sound

II: Curved flame with acoustic sound

III: Curved → Flat flame

IV: Curved → Flat → Corrugated → Turbulent

V : Curved → Corrugated → Turbulent

VI: Curved → Corrugated → Turbulent → Curved → Corrugated → Turbulent

Now, the flame behaviors at $Le < 1$, which are lean CH_4-N_2, lean and rich CH_4-CO_2, rich C_2H_4-CO_2, rich C_3H_8-N_2 and rich C_3H_8-CO_2, are considered. Here, the reason of which rich C_3H_8-N_2 flames are included in case of low *Le* despite $Le = 1.03$, will be discussed later. Figure 5.2 shows typical transition behaviors in respective Regimes after ignition at rich C_3H_8 diluted with N_2. The numerical values at the left hand side of the picture indicate the distance of the tube from upper side. When S_L is low, a regime of nonacoustic instability (Regime I) in which the curved flame propagates without fluctuation is identified as shown in Fig. 5.1. However, this regime is only observed in lean CH_4-N_2, because other fuels are relatively

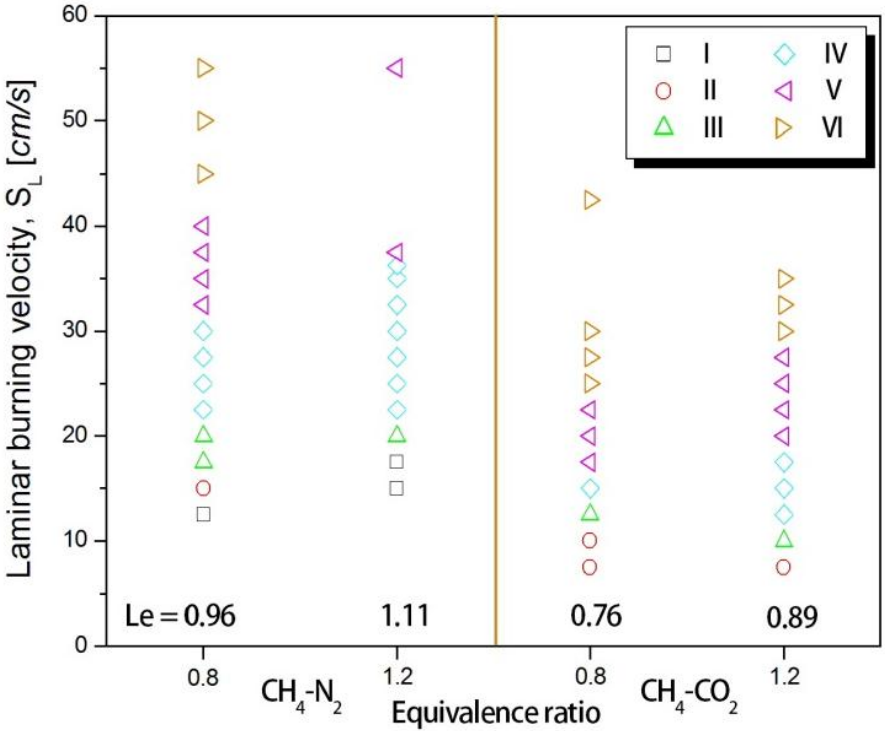
Laminar burning velocity, S_L [cm/s]
Le = 0.96
1.11
0.76
0.89
0.8
1.2
CH_4-N_2
Equivalence ratio
CH_4-CO_2
I
II
III
IV
V
VI

(a)

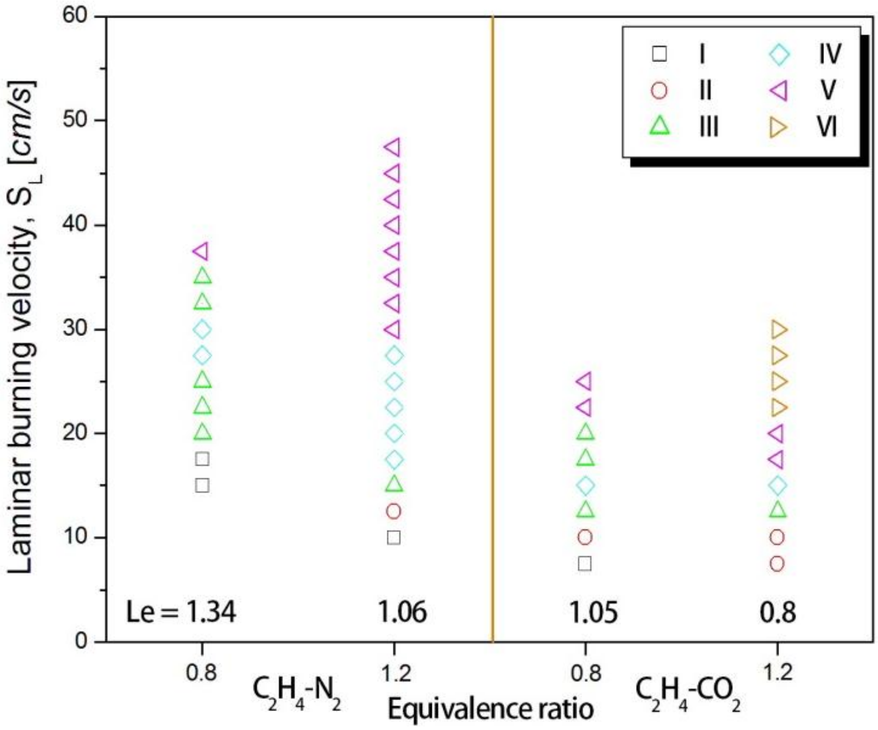
Laminar burning velocity, S_L [cm/s]
Le = 1.34
1.06
1.05
0.8
0.8
1.2
C_2H_4-N_2
Equivalence ratio
C_2H_4-CO_2
I
II
III
IV
V
VI

(b)

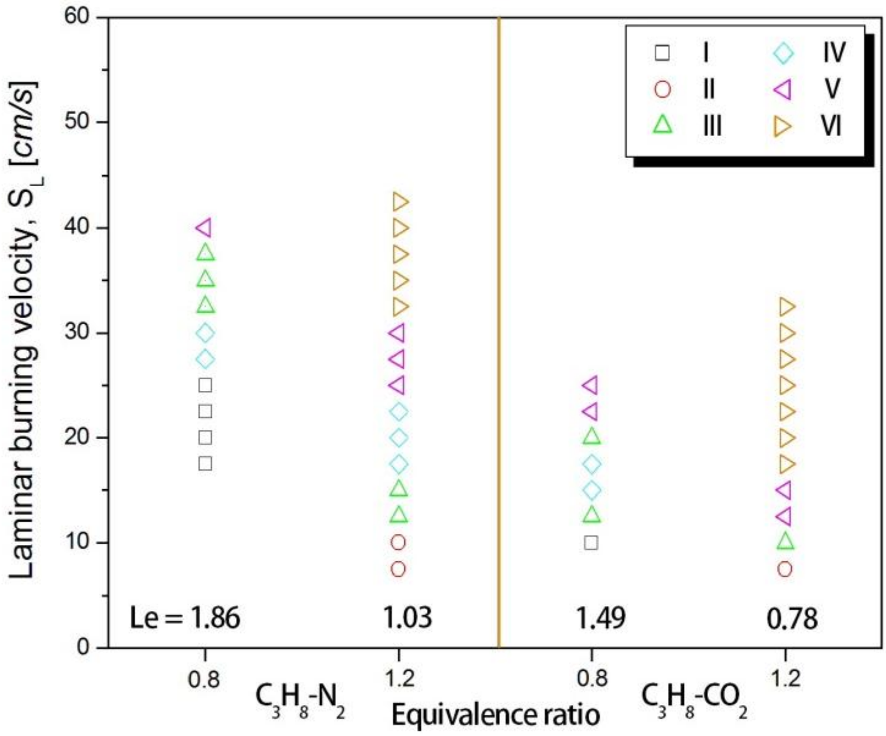

(c)

Fig. 5.1. Stability map of acoustic instability (a) CH_4 (b) C_2H_4 and (c) C_3H_8 diluted with N_2 or CO_2 at Φ = 0.8 and 1.2.

lower Le and the variations of flame temperatures are very sensitive to fluctuation of incoming unburned gas temperature by acoustic wave. In general, the growth rate of the short wavelength disturbance (e.g., cellular instability) is a function of $\frac{1}{2}\beta(1 - Le)$ studied by Sivashinsky [16, 17]. Thus, large growth rate represents unstable flame and inner flame structure is significantly affected by external disturbance such as gas temperature and pressure. When S_L increases in Fig. 5.1, a regime of acoustic instability (Regime II) is identified in which the flame fronts are still curved but vibrating with small acoustic sound as shown in Fig. 5.2. Here, when the flame reaches half of the tube, quasi-flat flame with the short wavelength disturbance appears, however, the flame has arbitrary propagating motion

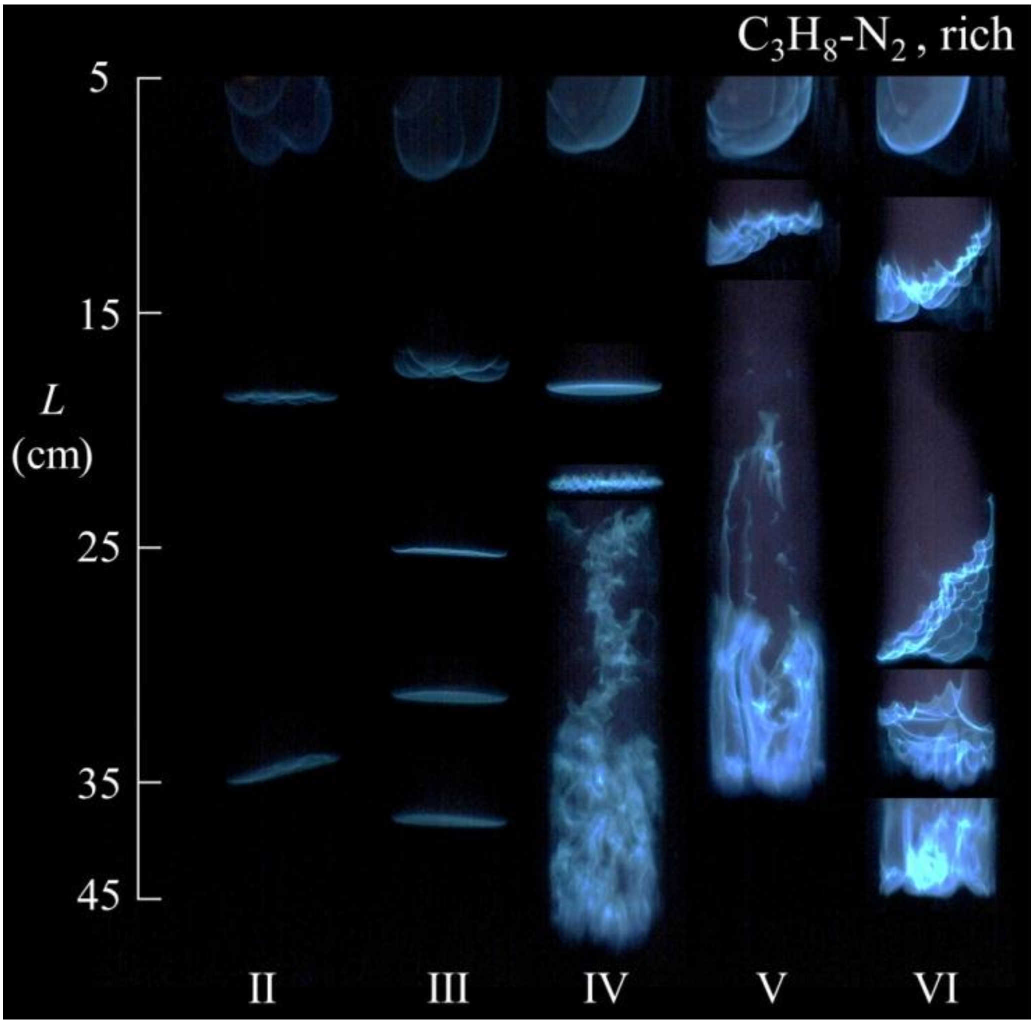

Fig. 5.2. The feature of flame behavior in acoustic field at rich C_3H_8 diluted with N_2.

without steady propagation as shown in Fig. 5.2. It can be understood that the primary acoustic saturation is not accompanied and still developing based on the pressure measurement. When S_L further increases in Fig. 5.1, the vibrating flat flames occur with relatively amplified acoustic sound (Regime III) as shown in Fig. 5.2. This is typical process of primary acoustic instability and the acoustic pressure is also saturated. After then, the vibrating flames finally result in turbulent motions via corrugated structure with violent acoustic sound by pre-existing finite-amplitude primary acoustic vibrations (Regime IV) as shown in Fig. 5.2. This is typical process of secondary acoustic instability. When S_L further increases in Fig. 5.1, explosive turbulent motion appears without the transition of the flat flames (Regime V) as shown in Fig. 5.2. Particularly, for *Le* < 1, Regime VI can be observed in which the explosive turbulent motion returns to the curved flame with decreasing acoustic sound in short period of flame propagation, then, turbulent motion reappears at large S_L as shown in Fig. 5.2. This may result from increasing order of magnitude difference between acoustic and chemical reaction time. Generally, a strong acoustic instability can appear when the chemical reaction time is close to the acoustic time, $\tau_c \approx \tau_a$. However, the shortened chemical reaction time by diffusive-thermal effect in *Le* < 1 may cause acoustic damping and restabilization of turbulization. Furthermore, the diffusive-thermal effect operates significantly in the corrugated structure because of increasing gradients of species concentration and heat.

Meanwhile, rich C_3H_8-N_2 flames follow the tendency of low *Le* despite *Le* = 1.03. This phenomenon may result from presence of heat losses to the wall. According to Jackson and Kapila's study [46], the critical *Le* causing the diffusive-thermal effects increases with excessive heat losses.

For *Le* > 1, the previous study [15] showed that the effect of thermal diffusion is dominant and the flame is diffusive-thermally stable. Also, the reaction zone is relatively insensitive to variation of gas temperature due to decreasing reaction rate [40, 41]. Therefore, it can be expected that the coupling between acoustic pressure and heat release fluctuations is relatively weaker than *Le* < 1.

In Fig. 5.1, five distinct types of behavior can be observed similar to low *Le* at *Le* > 1 which are rich CH_4-N_2, lean and rich C_2H_4-N_2, lean C_2H_4-CO_2, lean C_3H_8-N_2 and lean C_3H_8-CO_2. The tendency from Regime I to V is the same with low *Le* and, particularly, Regime VI does not appear because of decreasing reaction rate by the stabilizing contribution. However,

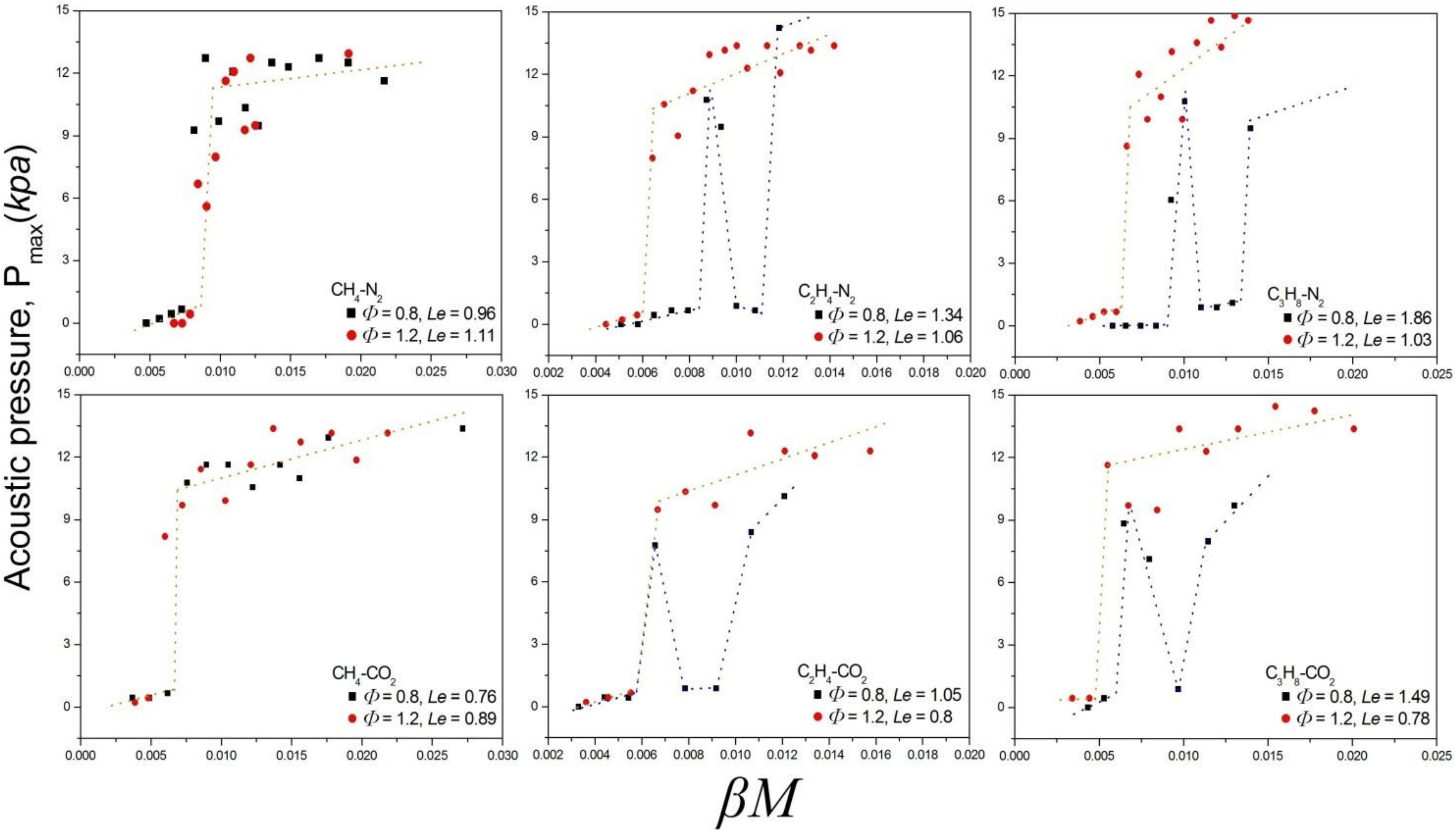

Fig. 5.3 Dependence of the coupling constant on maximum acoustic pressure in acoustic field at various gas compositions.

Regime III reappears after Regime IV at relatively large *Le* cases except of rich CH_4-N_2 and rich C_2H_4-N_2. Generally, vibrating flames in acoustic field tend to transit to secondary acoustic instability with increasing S_L by sufficiently high acoustic amplitude [25]. Therefore, a possible explanation for the restabilization of secondary acoustic instability is that the corrugated structure can be stable by the stabilizing contribution in large *Le*. Also, the stable flame would occur for $\beta(Le\text{-}1) < 11$ as determined by Sivashinsky [16, 17]. The Zel'dovich number can be calculated [5] as $\beta = E(T_b - T_u)/(RT_b^2)$. Here E is the activation energy, T is temperature, and R is the gas constant. In general, the Zel'dovich number increases with S_L because the thermal thickness is inverse proportion to β. Thus, adequately large S_L is required to observe the stabilizing contribution at the corrugated structure with highly strained flow field by accelerated acoustic field. This phenomenon is firstly introduced in the present study.

On comparing low and large *Le* in Fig. 5.1, the acoustic sound generates at relatively low S_L at $Le < 1$. This may be caused by more sensitive reaction rate from variation of gas temperature.

On the basis of the experimental evidence as listed above, maximum acoustic pressure as the coupling constant is characterized with different *Le* at various gas compositions in Fig. 5.3. The lower points represent primary acoustic instability and upper points are subjected to the secondary acoustic instability or turbulent flames. The major trend is that the maximum acoustic pressure increases with βM, and suddenly amplifies when secondary acoustic instability occurs. For CH_4 flames, effects of *Le* cannot be observed because differences of *Le* with varying equivalence ratios are not relatively significant than other fuels. For C_2H_4 and C_3H_8 flames, the stabilizing contribution tends to extend the region of primary acoustic instability at large *Le*, and secondary acoustic instability generates at large coupling constant. Finally, in adequately large βM, the restabilization of secondary acoustic instability takes place in very narrow region for large *Le*. Thus, it may be understood that the coupling constant, βM, is a key parameter in whole process of acoustic instability and effects of *Le* plays secondary role.

5.3 Concluding remarks

This Chapter 5 provides experimental evidence of effects of various fuels with different Lewis number on acoustic instability of freely downward-propagating flames for CH_4, C_2H_4 and C_3H_8 diluted with N_2 or CO_2 in a combustion tube. Flame stability maps were obtained and analyzed based on the observed flame behaviors in acoustic field.

The vibrating flame characteristics in downward-propagating flames were classified into six distinct regimes for $Le < 1$ on the flame stability maps: nonacoustic instability (Regime I), developing primary acoustic instability (Regime II), saturated primary acoustic instability (Regime III), secondary acoustic instability (Regime IV), turbulent flame (Regime V) and restabilization of turbulization (Regime VI).

The restabilization of turbulization may be caused by increasing order of magnitude difference between acoustic and chemical reaction time due to the diffusive-thermal effect, and is only observed in $Le < 1$.

For large *Le*, the restabilization of secondary acoustic instability appears by the stabilizing contribution at adequately large S_L. Also, the stabilizing effect causes to extend the region of primary acoustic instability as well as to delay initiation of secondary acoustic instability.

Chapter 6: Summary

The acoustic instability of downward-propagating flames in a combustion tube is investigated. The main focus was to establish the dominant onset mechanism of primary acoustic instability between pressure coupling and acceleration coupling. The flammable gas mixture was ignited at the top, open end of the tube, and a flame front propagated toward the closed end of tube. The flame behavior and acoustic pressure are measured.

In Chapter 3, the onset mechanism of primary acoustic instability of downward-propagating flames in a combustion tube is studied. The effects of a coupling constant, βM, and the variation in the flame surface area were considered. To change the coupling constant, various gas compositions for lean ethylene flames diluted with carbon dioxide or nitrogen were used. A linear relationship between the coupling constant and the average acoustic intensity was obtained, and the critical values of the coupling constants are acquired through linear approximation regarding the onset of the primary acoustic instability. Furthermore, the CO_2 laser irradiation method was adopted to alter the shape of the flame front, and experimental results showed that the variation in the flame surface area does not always cause spontaneous generation of the primary acoustic instability in initially nonvibrating flames. Furthermore, even in initially vibrating flat flames, the growth rate of the primary acoustic instability was not associated with the growth or decline in the flame surface area in the present experiments. Finally, the effects of acoustic losses on acoustic instability were also estimated, and experimental results showed that larger total acoustic losses tend to suppress acoustic vibration even at the same coupling constant.

In Chapter 4, the effects of the Lewis number on primary acoustic instability in non-equidiffusive flames were described, where the diffusive thermal effects largely determine the internal flame structure based on pressure coupling which is more dominant mechanism confirmed in Chapter 3. For a Lewis number below (above) unity, where the reaction rate increases (decreases) with reducing (increasing) reaction zone thickness, relatively strong (weak) acoustic sound was produced under the same coupling constant, because the chemical reaction rate becomes very sensitive (insensitive) to gas temperature fluctuations in the acoustic field. Finally, a linear relationship between the coupling constant and the average acoustic intensity was obtained, and results showed that relatively large coupling constant is required to generate primary acoustic instability as the Lewis number increases.

In Chapter 5, the effect of the various fuels for CH_4, C_2H_4 and C_3H_8 diluted with N_2 or CO_2 on acoustic instability was described. For Lewis number below (above) unity, the initiation of acoustic instability occurs at relatively small (large) coupling constant because the chemical reaction rate becomes sensitive (insensitive) to gas temperature fluctuation in acoustic field in connection with the results in Chapter 4. Also, when βM further increases, the restabilization of secondary acoustic instability takes place in very narrow region for large *Le* because of thermo-diffusively stable flames. In contrast, for small *Le*, the restabilization of turbulization occurs in short period of flame propagation by increasing order of magnitude difference between acoustic and chemical reaction time. It is shown that diffusive-thermal effect is a secondary role by comparison with βM in generation of acoustic instability.

References

[1] X. J. Gu, M. Z. Haq, M. Lawes, R. Woolley, Combust. Flame 121 (2000) 41-58.

[2] S. H. Chung, C. K. Law, Combust. Flame 55 (1984) 123-125.

[3] Y. S. Ko, S. H. Chung, Combust. Flame 118 (1999) 151-163.

[4] P. Pelcé, P. Clavin, J. Fluid Mech. 124 (1982) 219-237.

[5] P. Clavin, Prog. Energy Combust. Sci. 11 (1985) 1-59.

[6] A. Levy, Proc. Roy. Soc. A283 (1965) 134.

[7] J. Jarosinsky, R. A. Strehlow, A. Azarbarzin, Proc. Combust. Inst. 19 (1982)1549-1557.

[8] G. Darrieus, Unpublished work presented at La Technique Moderne, and at Le Congrés de Mécanique Appliqueée (1945).

[9] L. Landau, Acta Phys.-Chim. URSS 19 (1944) 77-85.

[10]G. Searby, Proc. Int. Conf. Combust. Detonation, Zel'dovich Memorial II (2004)

[11]F. A. Williams, Combustion Theory, 2nd ed., Benjamin-Cummins, Menlo Park (1985)

[12]G. H. Markstein, J. Aero. Sci. 18 (1951) 199-209.

[13]G. Joulin, P. Clavin, Combust. Flame 35 (1979) 139-153.

[14]G. I. Barenblatt, Y. B. Zeldovich, A. G. Istratov, Zh. Prikl. Mekh. Tekh. Fiz. 4 (1962) 21-26

[15]G. H. Markstein, Proc. Combust. Inst. 4 (1952) 44-59.

[16]G. I. Sivashinsky, Rev. Fluid. Mech. 15 (1983) 179-199.

[17]G. I. Sivashinsky, Combust. Sci. and Tech. 15 (1977) 137-145.

[18]H. Pearlman, P. Ronney, Physics of Fluids 6 (12) 4009-4018.

[19]H. Pearlman, P. Ronney, J. Chem. Phys. 101 (3) 2632-2633.

[20]A. G. Class, B. J. Matkowsky, A. Y. Klimenko, J. Fluid Mech. 491 (2003) 51-63.

[21]C. K. Law, Combustion Physics, Cambridge University Press (2006).

[22]Y. Ma, PhD Thesis, Drexel University (2009).

[23]D.T. Harrje, F.H. Reardon, Liquid propellant rocket combustion instability, Report No. NASA-SP-194, NASA, 1972.

[24]J. Rayleigh, Nature. 18 (1878) 319.

[25]G. Searby, Combust. Sci. and Tech. 81 (1992) 221-231.

[26]W. E. Kaskan, Proc. Combust. Inst. 4 (1953) 575-591.

[27]R. A. Dunlap, Aeronautical Research Center, University of Michigan. Project MX833. Rep. UMM-43(1950).

[28]P. Clavin, P. Pelcé, L. He, J. Fluid Mech. 216 (1990) 299-322.

[29]G. H. Markstein, Proc. Sixth Natl Congr. Appl. Mech., Cambridge, Mass. 11 (1970) 11-33.

[30]P. Pelcé, D. Rochwerger, J. Fluid Mech. 239 (1992) 293-307.

[31]M. Faraday, Phil. Trans. R. Soc. Lond. 121 (1831) 319-340

[32]G. H. Markstein, Proc. Sixth Natl Congr. Appl. Mech., Cambridge, Mass. 11 (1970) 11-33.

[33]G. Searby, D. Rochwerger, J. Fluid Mech. 231 (1991) 529-543.

[34]C. Clanet, G. Searby, P. Clavin, Fluid Mech. 385 (1999) 157-197.

[35]D. Bradley, Internal Combustion Engineering: Science and Technology (J Wearing, Ed.), Elsevier Applied Science, London (1990) 287-331.

[36]N. Peters, F. A. Williams, Combust. Flame 68 (1987) 185-207.

[37]M. Tsuchimoto, O. Fujita, T. Honko, Y. Nakamura, H. Ito, Proc. Combust. Inst. 32 (2009) 1003-1009.

[38]J. S. Park, O. Fujita, Y. Nakamura, H. Ito, Proc. Combust. Inst. 33 (2011) 1105-1112.

[39]Y. Taniyama, O. Fujita, Combust. Flame 161 (2014) 1558-1565.

[40]G.J. Sharpe, Combust. Theory Model 7 (1) (2003) 45-65.

[41]S. Kadowaki, M. Yahata, H. Kobayashi, J. Thermal Sci. Technol. 6 (3) (2011) 376-390.

[42]The national institute of standards and technology (NIST), available at <hittp://webbook.nist.gov/chemistry/>.

[43]R. J. Kee, R. M. Rupley, et al., CHEMKIN PRO, Reaction Design, Inc., San Diego, CA, 2009.

[44]S. H. Kang, S. W. Baek, H. G. Im, Combust. Theor. Model. 10 (2006) 659-681.

[45]J. Yuan, Y. Ju, C. K. Law, Combust. Flame 144 (2006) 386-397.

[46]T.L. Jackson, A.K. Kapila, Combust. Sci. Technol. 49 (5-6) (1986) 305-317.

[47]L. Landau, E. Lifshitz, Fluid Mechanics, 1st edn. Pergamon (1986).

[48]S. Gade, M. Sc, Sound intensity, Technical review 3 (1982) 3-39.

Appendix A: Acoustic losses

In general, the acoustic energy is dissipated at the open end of the tube through radiative losses and at the wall through diffusive losses, and the acoustic instability generates when the gain produced by the flame overcomes the acoustic losses. The characteristic times of acoustic losses can be expressed as follows [34, 47].

Radiative losses: $1/\tau_{\mathrm{rad}} = (\omega r)^2/(8cL)$, where r is the tube radius and L is the length of the tube. The radiative losses are proportional to ω^2. In this study, the speed of sound, c, is calculated using CHEMKIN (Premix code/USC II) [43]. The radiative losses are only affected by the speed of sound when a single combustion tube is used. Therefore, it is expected that the flames diluted with nitrogen have higher $1/\tau_{\mathrm{rad}}$ than those diluted with carbon dioxide.

Wall losses: $1/\tau_{\mathrm{wall}} = \sqrt{8}(\omega\alpha)^{0.5}[(\gamma - 1) + Pr^{0.5}]/r$, where α is the thermal diffusivity, γ is the specific heat ratio, Pr is the Prandtl number (= ν/α), and ν is the kinematic viscosity. The first term in the brackets is related to the thermal boundary layer and the second term is related to the viscous layer. The wall losses are proportional to $(\omega\alpha + \omega\nu)^{0.5}$. Finally, the total acoustic loss, $1/\tau_{\mathrm{loss}}$, is given by $1/\tau_{\mathrm{loss}} = 1/\tau_{\mathrm{rad}} + 1/\tau_{\mathrm{wall}}$.

Appendix B: Calculation of acoustic intensity

The sound intensity (or the acoustic intensity) is defined as the acoustic power per unit area, $I = P_u u_u$. The average sound intensity, $\langle I \rangle$, during time is given by [48]

$$\langle I \rangle = \frac{1}{t}\int_0^t P_u(t) u_u(t) \mathrm{d}t. \tag{B1}$$

Here, the acoustic pressure of the unburned mixture in front of the flame is obtained by the pressure measured at the bottom of tube, P_o. Pressures elsewhere in the tube at any time are given by [26]

$$P_u(x) = P_o \cos\frac{2\pi x}{\lambda}, \tag{B2}$$

where x is the distance along the tube measured from the bottom as depicted Fig. 1b and λ is the wavelength of sound associated with the angular frequency ω. The displacement of the unburned mixture, ξ_u, is given as follows [26]:

$$\xi_u(x) = \frac{P_o \sin\frac{2\pi x}{\lambda}}{\rho c \omega}. \tag{B3}$$

Thus, the acoustic velocity of the unburned mixture can be obtained by $u_u = \mathrm{d}\xi_u/\mathrm{d}t$.

Appendix C: 2014 Photo Contest – Beautiful Flames, Combustion Society of Japan

“The Highest Award”

Title: Flame cake of the first birthday

Explanation of photo

Title: Flame cake of the first birthday

SungHwan YOON, TaeJoon NOH, Osamu FUJITA

Hokkaido University, Kita13 Nishi 8, Kita-ku, Sapporo, Hokkaido, Japan

This flame was formed from interaction between acoustic vibration and downward propagating flame in combustion tube of 5 cm diameter and 51.1 cm long. A desired curvature is initially given to the propagating flame by CO_2 laser absorption. The combustion tube is half-open at the top end, ignition side. C_2H_4/O2/CO_2 mixture of Le = 1.05 and $\Phi = 0.9$ is used as the tested gas. When curved flame is exposed to the acoustic vibration field in the combustion tube, coherent corrugated structure is formed and then it turns to complicated turbulent motion. The picture is one moment of corrugated structure before transition to turbulent motion. This picture seems birthday cake. The lower flame in the picture looks like a cake and the separated flame above the main flame, which is caused by auto ignition, seems a candle flame. Therefore, the flame is named as "Flame cake of the first birthday".

Camera & Lens: FASTCAM Mini UX100 & NOKTON 25mm F0.95

F-number: F0.95, Frame Rate: 2000 fps at 768 x 512 pixel resolution, ISO: 5000

Appendix D: 2015 Contest of Visualization of Combustion, Korea Society of Combustion

“The Best Visualization Award”

Title: Visualization of Transient Flame Motion in a Combustion Tube Induced by External CO_2 Laser Irradiation

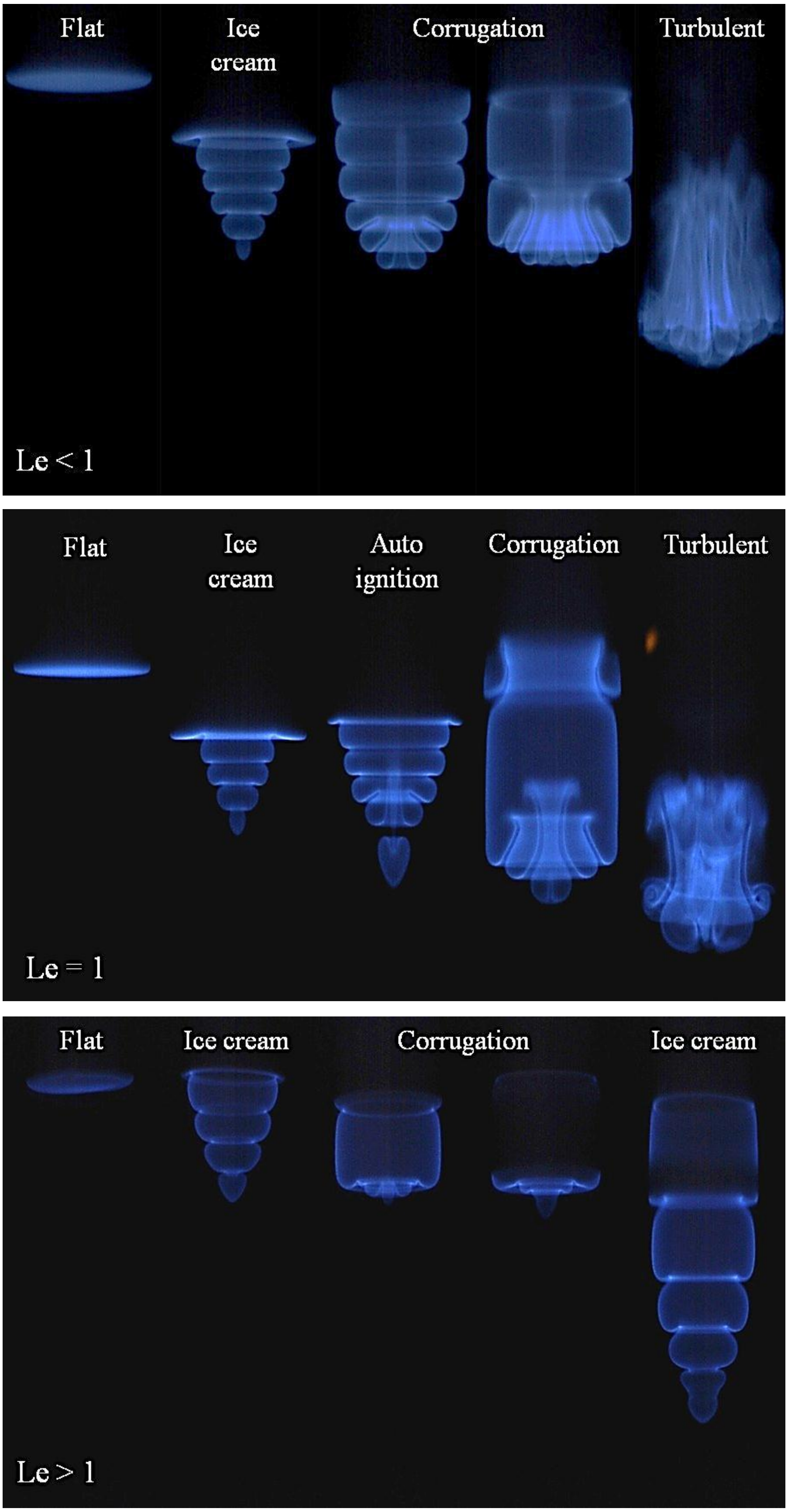
Flat
Ice cream
Corrugation
Turbulent
Le < 1
Flat
Ice cream
Auto ignition
Corrugation
Turbulent
Le = 1
Flat
Ice cream
Corrugation
Ice cream
Le > 1

Explanation of visualization

Title: Visualization of Transient Flame Motion in a Combustion Tube Induced by External CO_2 Laser Irradiation

SungHwan YOON, TaeJoon NOH, Osamu FUJITA

Hokkaido University, Kita13 Nishi 8, Kita-ku, Sapporo, Hokkaido, Japan

The visible imageries present an experimental description of dynamic behaviors of flame fronts in downward propagating flames for different Lewis number. A novel method is utilized, the CO_2 laser irradiation method, to control the shape of freely propagating flames, because the ethylene gas used is the main absorption medium of CO_2 laser light. To create identically initial flame at the initial moment of irradiating CO_2 laser, the completely flat flame front is selected as a default flame, which is corresponding to the primary acoustic instability as reported by Searby. Carbon dioxide and nitrogen were selected as diluents to control Lewis number. The time-dependent behaviors of the downward propagating flame are captured by high speed cameras. The visualization shows characteristic flame behaviors in different Lewis number. Once the corrugated structure is established the flame accelerates for $Le < 1$ because of relatively strong mass diffusion effect and the corrugated structure leads to the turbulent motion. For *Le* > 1, the flame cannot be transition to the turbulent mode because stabilization of the corrugated structure appears due to the conductive heat loss to the unburned side by thermal diffusion effect. Interestingly, the auto-ignited flame during transition to the turbulent motion for *Le* = 1 could be observed.

Camera & Lens: FASTCAM Mini UX100 & NOKTON 25 mm F0.95

F-number: F0.95, Frame Rate: 2000 fps, ISO: 5000

Achievements

Journal publications:

1. **<u>S. H. Yoon</u>**, T. J. Noh, O. Fujita, “Effects of Lewis number on generation of primary acoustic instability in downward-propagating flames”, ***Proceedings of the Combustion Institute***, (under revision).
2. **<u>S. H. Yoon</u>**, T. J. Noh, O. Fujita, “Onset mechanism of primary acoustic instability in downward-propagating flames”, ***Combustion and Flame*** 170 (2016) 1-11.
3. O. Fujita, **<u>S. H. Yoon</u>**, Y. Taniyama, “Research on instability of propagating flames in a combustion tube by using laser irradiation method”, ***Journal of the Combustion Society of Japan*** 181 (2015) 174-182.
4. Q. Wang, L. Hu, **<u>S. H. Yoon</u>**, S. Lu, M. Delichatsios, S. H. Chung, “Blow-out limits of nonpremixed turbulent jet flames in a cross flow at atmospheric and sub-atmospheric pressures”, ***Combustion and Flame*** 162 (2015) 3562-3568.
5. W. J. Lee, **<u>S. H. Yoon</u>**, J. Park, O. B. Kwon, Y. J. Kim, T. H. Kim, J. H. Yun, S. I. Keel, “Lewis-number-induced and buoyancy-driven self-excitations in nitrogen-diluted laminar free-jet flames”, ***Fuel*** 112 (2013) 366-374.
6. S. I. Keel, H. Y. Park, Y. J. Kim, **<u>S. H. Yoon</u>**, “Engineering control of mill fire for high volatile sub-bituminous coal”, ***Korea Society of Combustion*** 18 (2013) 53-58.

Conference publications:

1. T. J. Noh, **<u>S. H. Yoon</u>**, O. Fujita, “A study on the effect of propagation direction on onset of primary acoustic instability by comparing downward and upward propagating flames in a tube”, ***54th Symposium (Japanese) on Combustion***, Sendai, Japan, (2016. 11, Oral presentation, To be presented).

2. **<u>S. H. Yoon</u>**, O. Fujita, "Experimental observation of pulsating instability under acoustic field at large Lewis number", ***9th National Congress on Fluids Engineering***, Daegu, Korea, (2016. 8, Oral presentation).

3. **<u>S. H. Yoon</u>**, T. J. Noh, O. Fujita, "Effects of Lewis number on generation of primary acoustic instability in downward-propagating flames", ***36th International Symposium on Combustion***, Seoul, Korea, (2016. 8, Oral presentation).

4. T. J. Noh, **<u>S. H. Yoon</u>**, O. Fujita, "The comparative study of acoustic instabiilty of downward and upward propagating flames in a tube", ***36th International Symposium on Combustion***, Seoul, Korea, (2016. 8, Poster presentation).

5. **<u>S. H. Yoon</u>**, T. J. Noh, O. Fujita, "Effect of Lewis number on acoustic instability of freely propagating flames in a tube", ***International Symposium: Thermoacoustic Instabilities in Gas Turbines and Rocket Engines: Industry meets Academia***, Munich, Germany, (2016. 6, Oral presentation).

6. **<u>S. H. Yoon</u>**, T. J. Noh, O. Fujita, "Effect of Lewis number on the initiation of primary acoustic instability in a combustion tube", ***1st Pacific Rim Thermal Engineering Conference***, Hawaii, USA, (2016. 3, Oral presentation).

7. T. J. Noh, **<u>S. H. Yoon</u>**, O. Fujita, "Effects of Lewis number on acoustic instability of upward propagating premixed flames in a combustion tube", ***53rd Symposium (Japanese) on Combustion***, Tsukuba, Japan, (2015. 11, Oral presentation).

8. **<u>S. H. Yoon</u>**, O. Fujita, "Effects of variation of the flame area and natural damping on primary acoustic instability of downward propagating flames in a tube", ***25th International Colloquium in the Dynamics of Explosions and Reactive Systems***, Leeds, England, (2015. 8, Oral presentation).

9. T. J. Noh, **<u>S. H. Yoon</u>**, O. Fujita, "Effect of Lewis number on acoustic instability of

upward propagating ethylene flames", ***50th Korea Society of Combustion Symposium***, Suncheon, Korea, (2015. 5, Oral presentation).

10. **S. H. Yoon**, O. Fujita, "A study on effects of thermal diffusion and burning velocity in acoustic instability", ***52nd Symposium (Japanese) on Combustion***, Okayama, Japan, (2014. 12, Oral presentation).
11. **S. H. Yoon**, T. J. Noh, O. Fujita, "Effect of Lewis number on acoustic instability of downward propagating flames", ***47th Korea Society of Combustion Symposium***, Busan, Korea, (2013. 12, Oral presentation).
12. **S. H. Yoon**, O. Fujita, "Effect of Lewis number on acoustic instability of downward propagating flames", ***Seoul National University - Hokkaido University Joint Symposium***, Seoul, Korea, (2013. 12, Poster presentation).
13. J. Park, **S. H. Yoon**, Y. H. Chung, W. J. Lee, "Self-excitation of edge flame in laminar lifted jet and non-premixed counterflow flames" (Topical review), ***9th Asia Pacific Conference on Combustion***, Gyeongju, Korea (2013. 5, Oral presentation).
14. J. Park, **S. H. Yoon**, Y. H. Chung, W. J. Lee, O. B. Kwon, "Self-excitation of edge flame", ***45th Korea Society of Combustion Symposium***, Pohang, Korea (2012. 11, Oral presentation).
15. J. K. Han, **S. H. Yoon**, J. Park, J. H. Yun, S. I. Keel, "Comparison between diffusive-thermal and buoyancy-driven self-excitations in laminar lifted free-jet flames", ***9th China-Japan-Korea Workshop on Microgravity Sciences***, China (2012. 10, Oral presentation).
16. W. J. Lee, **S. H. Yoon**, J. Park, J. H. Yun, S. I. Keel, "Heat-loss-induced self-excitation in laminar lifted coflow-jet flames", ***9th China-Japan-Korea Workshop on Microgravity Sciences***, China (2012. 10, Oral presentation).

Awards:

1. "**The Best Visualization Award**", 2015 Contest of Visualization of Combustion, Korea Society of Combustion, Korea (2015. 12).
2. "**The Highest Award**", 2014 Photo Contest – Beautiful Flames, Combustion Society of Japan, Japan (2014. 12).
3. Selected as a scholarship student from Ministry of Education of Japanese Government (MEXT), Japan (2012. 10).